UNIVERSITY OF CALIFORNIA, SAN DIEGO

CMB Polarization Measurements with the POLARBEAR Experiment

A dissertation submitted in partial satisfaction of the
requirements for the degree
Doctor of Philosophy

in

Physics

by

David Boettger

Committee in charge:

Professor Hans Paar, Chair
Professor Brian Keating, Co-Chair
Professor Kim Griest
Professor William Hodgkiss
Professor Gabriel Rebeiz

2014

The dissertation of David Boettger is approved, and it is acceptable in quality and form for publication on microfilm and electronically:

_____

_____

_____

_____
Co-Chair

_____
Chair

University of California, San Diego

2014

EPIGRAPH

¿Quién escribe tu nombre con letras de humo entre las estrellas del sur?
Ah déjame recordarte cómo eras entonces, cuando aún no existías.
—Pablo Neruda

TABLE OF CONTENTS

LIST OF FIGURES

LIST OF TABLES

ACKNOWLEDGEMENTS

I have had a wonderful experience working on this project over the past seven years. I am indebted to many people without whose friendship, expert guidance, and encouragement I could not have made it this far.

I would first like to thank my advisor Hans Paar for providing me with the opportunity to work on the project, for many intellectually stimulating and encouraging conversations over the years, and for being so tolerant of the long periods of time I have spent away from San Diego. I would also like to thank Brian Keating for all of his support and advice during my time in this group.

I spent several long stretches of time in Berkeley working on this project, and I thank Adrian Lee for that opportunity and the guidance he provided. The patience and thoughtful explanations of Mike Myers also helped to ensure that this time I spent in Berkeley was productive, educational, and enjoyable. It was a pleasure to work closely with Zigmund Kermish in Berkeley and the field as well. I thank Bryan Steinbach for many challenging and enlightening discussions. My time in Berkeley was also greatly improved by the presence of many others, among them Daniel Flanigan, Chase Shimmin, Marius Lungu, Erin Quealy, Haruki Nishino, Toki Suzuki, Liz George, Nick Harrington, Christian Reichardt, Yuji Chinone, and Joseph Martino.

I also feel extremely fortunate to have worked with a fantastic group of people in San Diego. Nate Stebor, Brandon Wilson, and Stephanie Moyerman all made my time both in and out of lab far more enjoyable than it would have been otherwise. The same is true of Darcy Barron, with whom I also enjoyed several international adventures related to POLARBEAR travel. I have enjoyed the presence of many other co-workers in and out of the lab including Lisa Krayer, Fred Matsuda, Praween Siritanasak, Matt Atlas, Chris Aleman, James Feng, Amit Yadav, Jon Kaufman, Chang Feng, Ian Schanning, Tucker Elleflot, Marty Navaroli, Priscilla Kelly, and Nathan Miller.

It is also my pleasure to thank Kam Arnold, with whom I have spent time in Berkeley, Cedar Flat for the initial engineering deployment, Chile for the science deployment, and San Diego. I have received a tremendous amount of technical and

life advice from him, and his energy and enthusiasm never cease to amaze me.

Apart from co-workers, I would also like to thank my family and other friends not connected with POLARBEAR, to whom I am very grateful for their support and encouragement over my time in graduate school.

I have enjoyed the time I have been able to spend in Chile. I thank all of the wonderful people I have met there for being so welcoming and friendly, and I greatly look forward to the years I will spend in Chile to continue working on this project.

Finally, I would like to acknowledge the tremendous contributions of Huan Tran, which were crucial to the successes this project has achieved thus far and will hopefully continue to achieve in the future. He has and will continue to be dearly missed as a friend and colleague.

Figures 2.1 and 2.4 are reprints of material as it appears in The POLARBEAR experiment. Z. D. Kermish, P. Ade, A. Anthony, K. Arnold, D. Barron, D. Boettger, J. Borrill, S. Chapman, Y. Chinone, M. A. Dobbs, J. Errard, G. Fabbian, D. Flanigan, G. Fuller, A. Ghribi, W. Grainger, N. Halverson, M. Hasegawa, K. Hattori, M. Hazumi, W. L. Holzapfel, J. Howard, P. Hyland, A. Jaffe, B. Keating, T. Kisner, A. T. Lee, M. Le Jeune, E. Linder, M. Lungu, F. Matsuda, T. Matsumura, X. Meng, N. J. Miller, H. Morii, S. Moyerman, M. J. Myers, H. Nishino, H. Paar, E. Quealy, C. L. Reichardt, P. L. Richards, C. Ross, A. Shimizu, M. Shimon, C. Shimmin, M. Sholl, P. Siritanasak, H. Spieler, N. Stebor, B. Steinbach, R. Stompor, A. Suzuki, T. Tomaru, C. Tucker, and O. Zahn, Society of Photo-Optical Instrumentation Engineers (SPIE) Conference Series, vol. 8452 of Society of Photo-Optical Instrumentation Engineers (SPIE) Conference Series, Sept. 2012. The dissertation author made essential contributions to many aspects of this work.

Figure 2.5 and figure 2.7 are reprints of material as it appears in The bolometric focal plane array of the POLARBEAR CMB experiment. K. Arnold, P. A. R. Ade, A. E. Anthony, D. Barron, D. Boettger, J. Borrill, S. Chapman, Y. Chinone, M. A. Dobbs, J. Errard, G. Fabbian, D. Flanigan, G. Fuller, A. Ghribi, W. Grainger, N. Halverson, M. Hasegawa, K. Hattori, M. Hazumi, W. L. Holzapfel, J. Howard, P. Hyland, A. Jaffe, B. Keating, Z. Kermish, T. Kisner, M. Le Je-

une, A. T. Lee, E. Linder, M. Lungu, F. Matsuda, T. Matsumura, N. J. Miller, X. Meng, H. Morii, S. Moyerman, M. J. Myers, H. Nishino, H. Paar, E. Quealy, C. Reichardt, P. L. Richards, C. Ross, A. Shimizu, C. Shimmin, M. Shimon, M. Sholl, P. Siritanasak, H. Spieler, N. Stebor, B. Steinbach, R. Stompor, A. Suzuki, T. Tomaru, C. Tucker, and O. Zahn, Society of Photo-Optical Instrumentation Engineers (SPIE) Conference Series, vol. 8452 of Society of Photo-Optical Instrumentation Engineers (SPIE) Conference Series, Sept. 2012. The dissertation author made essential contributions to many aspects of this work.

Figures 2.2, 3.11, 3.20, 4.8, 4.11, 4.12, 5.4, and table 5.1 are reprints of material as it appears in A Measurement of the Cosmic Microwave Background B-Mode Polarization Power Spectrum at Sub-Degree Scales with POLARBEAR. The POLARBEAR Collaboration: P. A. R. Ade, Y. Akiba, A. E. Anthony, K. Arnold, M. Atlas, D. Barron, D. Boettger, J. Borrill, S. Chapman, Y. Chinone, M. Dobbs, T. Elleflot, J. Errard, G. Fabbian, C. Feng, D. Flanigan, A. Gilbert, W. Grainger, N. W. Halverson, M. Hasegawa, K. Hattori, M. Hazumi, W. L. Holzapfel, Y. Hori, J. Howard, P. Hyland, Y. Inoue, G. C. Jaehnig, A. H. Jaffe, B. Keating, Z. Kermish, R. Keskitalo, T. Kisner, M. Le Jeune, A. T. Lee, E. M. Leitch, E. Linder, M. Lungu, F. Matsuda, T. Matsumura, X. Meng, N. J. Miller, H. Morii, S. Moyerman, M. J. Myers, M. Navaroli, H. Nishino, H. Paar, J. Peloton, D. Poletti, E. Quealy, G. Rebeiz, C. L. Reichardt, P. L. Richards, C. Ross, I. Schanning, D. E. Schenck, B. D. Sherwin, A. Shimizu, C. Shimmin, M. Shimon, P. Siritanasak, G. Smecher, H. Spieler, N. Stebor, B. Steinbach, R. Stompor, A. Suzuki, S. Takakura, T. Tomaru, B. Wilson, A. Yadav, and O. Zahn, ArXiv e-prints, Mar. 2014. The dissertation author made essential contributions to many aspects of this work.

Figure 6.1 was provided by Chang Feng. Figure 6.3 was provided by Yuji Chinone. The dissertation author made essential contributions to many aspects of both works.

VITA

2005	B. S. in Physics *summa cum laude*, University of Southern California
2005-2007	Teaching Assistant, University of California, San Diego
2008-2014	Graduate Student Researcher, University of California, San Diego
2014	Ph. D. in Physics, University of California, San Diego

PUBLICATIONS

The POLARBEAR Collaboration: P.A.R. Ade, Y. Akiba, A.E. Anthony, K. Arnold, M. Atlas, D. Barron, D. Boettger, et al.,A Measurement of the Cosmic Microwave Background B-Mode Polarization Power Spectrum at Sub-Degree Scales with POLARBEAR. http://arxiv.org/abs/1403.2369

The POLARBEAR Collaboration: P.A.R. Ade, Y. Akiba, A.E. Anthony, K. Arnold, D. Barron, D. Boettger, et al., Gravitational Lensing of Cosmic Microwave Background Polarization. http://arxiv.org/abs/1312.6646

The POLARBEAR Collaboration: P.A.R. Ade, Y. Akiba, A.E. Anthony, K. Arnold, D. Barron, D. Boettger, et al., Evidence for Gravitational Lensing of the Cosmic Microwave Background Polarization from Cross-correlation with the Cosmic Infrared Background. Physical Review Letters, Volume 112, Issue 13

K. Arnold, P.A.R. Ade, A.E. Anthony, D. Barron, D. Boettger, et al., The bolometric focal plane array of the POLARBEAR CMB experiment. http://arxiv.org/abs/1210.7877

Z. Kermish, P. Ade, A. Anthony, K. Arnold, K. Arnold, D. Barron, D. Boettger, et al., The POLARBEAR Experiment. http://arxiv.org/abs/1210.7768

B. Keating, S. Moyerman, D. Boettger, J. Edwards, G. Fuller, et al., Ultra High Energy Cosmology with POLARBEAR. http://arxiv.org/abs/1110.2101

The POLARBEAR Collaboration: J. Errard, P.A.R. Ade, A. Anthony, K. Arnold, F. Aubin, D. Boettger, et al., The new generation CMB B-mode polarization experiment: POLARBEAR. http://arxiv.org/abs/1011.0763

ABSTRACT OF THE DISSERTATION

CMB Polarization Measurements with the POLARBEAR Experiment

by

David Boettger

Doctor of Philosophy in Physics

University of California, San Diego, 2014

Professor Hans Paar, Chair
Professor Brian Keating, Co-Chair

POLARBEAR is an experiment designed to measure the polarization of the cosmic microwave background (CMB). These measurements have scientific objectives spanning particle physics, cosmology, and astrophysics. The field of CMB polarization is rapidly evolving, with extraordinary progress being made on several fronts including the recently claimed detection of gravitational waves generated during cosmic inflation.

This dissertation describes the POLARBEAR instrument and the measurements taken during its first season of observations. The results include the first evidence for a non-zero C_ℓ^{BB} power spectrum at sub-degree angular scales, consistent with theoretical expectations.

Chapter 1

Introduction

Less than a century has elapsed since the publication of the general theory of relativity [1], and efforts in that time have yielded profound changes to our understanding of cosmology. Theoretical and observational progress has allowed us to develop and test precise physical theories about the history, shape and composition of the universe. Near the end of the twentieth century, observational evidence began to converge on the Lambda-Cold Dark Matter (ΛCDM) model, which has now become the "standard model" of cosmology. In many respects this model is surprisingly simple, and has now survived more than a decade of increasingly strenuous observational tests. These tests have come from a diverse range of observations spanning many different measurement techniques and cosmic distance scales. Measurements of the cosmic microwave background (CMB) have played a particularly important role in formulating and testing ΛCDM.

This dissertation describes experimental efforts to measure polarization of the CMB with the POLARBEAR experiment. CMB polarization is a field which allows even stricter tests of the ΛCDM model as well as enables probes of new and otherwise untestable physics. Using CMB polarization measurements, the BICEP2 experiment has recently reported the detection of gravitational waves generated during inflation [2]. If confirmed, this implies that CMB polarization measurements can probe physics at the grand unification energy scale, which is completely inaccessible to any other current experimental technique.

We begin with a brief overview of cosmology and the CMB, including a

discussion of its polarization and the goals behind measuring it. It is not our aim to re-derive well known results available in the literature, but instead to provide a broad overview of the context in which the questions this dissertation addresses are being asked.

1.1 General Relativity and the Expansion of the Universe

General relativity is the conceptual framework that underpins our theoretical understanding of the expanding universe. The idea that the universe we see today emerged from a hotter, denser primordial universe via the expansion of space is a general expression of the Big Bang theory, and forms the basis of modern cosmology. We will briefly discuss general relativity and how it motivates such an idea.

1.1.1 The Metric in General Relativity

Distances and time intervals can be described for a coordinate system by using the 4×4 metric tensor $g_{\mu\nu}$, with a line element ds written as $ds^2 = g_{\mu\nu}dx^\mu dx^\nu$ [1]. For a given coordinate system, the associated metric tensor tells us how to determine physical distances and time intervals via an integral over line elements along some path of interest. This is a mathematical construction which general relativity uses to describe the nature of space.

In general relativity, the Einstein field equations determine the form of the metric $g_{\mu\nu}$ given a distribution of energy (in all its forms, including matter), and energy moves along geodesic curves determined by the metric. Effectively, matter and energy tell space how to bend, and the bending of space tells matter and energy how to move [3]. In this way, general relativity describes space as a dynamical object that changes in response to the energy it contains.

[1] There is an implied sum on μ and ν over the three spatial and one temporal dimensions by the standard Einstein summation convention.

The Einstein field equations are ten coupled, non-linear differential equations, which in practice admit few exact analytic solutions. This is equivalent to saying that for most arbitrary distributions of matter and energy, the metric $g_{\mu\nu}$ cannot be determined exactly. However, exact solutions are possible under assumptions of symmetries that simplify the problem.

1.1.2 The Cosmological Principle

An example of such a symmetry, known as the *Cosmological Principle*, requires that the distribution of energy (and thus space) be the same everywhere (homogeneous) and further contain no preferred direction (isotropic)[2]. This assumption is manifestly violated in the modern universe, yet it is believed to be close to correct in the early universe and even to hold today when considered only at sufficiently large distance scales. The metric that follows under these assumptions is known as the Friedmann-Lemaître-Robertson-Walker (FLRW) metric, and yields a line element in co-moving coordinates of[3] [4]:

$$ds^2 = -dt^2 + a^2(t)\frac{(dx^2 + dy^2 + dz^2)}{[1 + \frac{\kappa}{4a^2(t)}(x^2 + y^2 + z^2)]^2}, \quad \kappa = 0, \pm 1. \tag{1.1}$$

The value of κ determines the type of spatial curvature, with $\kappa = 0$ implying that space is flat. For flat space, this metric behaves like the normal Minkowski-space metric of special relativity, except for the scaling of spatial distances by the scale factor $a(t)$ which up to this point has been an arbitrary function of the time coordinate t. Thus we see that the physical distances between two spatial coordinate points can grow or shrink as a function of time, corresponding to an expansion or contraction of space.

1.1.3 The Friedmann Equation

Deriving the FLRW metric above relies only upon symmetery arguments and not general relativity. It falls to general relativity to determine the scale factor

[2]While these conditions are typically stated separately, isotropy at all points in space implies homogeneity [4], though isotropy at one particular point does not.

[3]We have chosen to work in natural units where $c = \hbar = k_B = 1$ and thus c is omitted here.

$a(t)$ as a function of time given a physical distribution of matter and energy obeying the *Cosmological Principle*. If we define the Hubble rate and critical densities as:

$$H(t) \equiv \frac{\dot{a}(t)}{a(t)}, \quad \rho_{crit}(t) \equiv \frac{3H^2(t)}{8\pi G}, \tag{1.2}$$

we can write the Friedmann equation, which governs the evolution of the scale factor, as[4] [5]:

$$H^2(t) = \frac{8\pi G}{3}\left(\rho(t) + \frac{\rho_{crit}(t) - \rho(t)}{a^2(t)}\right) = \frac{8\pi G}{3}\rho(t) - \frac{\kappa}{a^2(t)}, \tag{1.3}$$

and the Friedmann acceleration equation as:

$$\frac{\ddot{a}(t)}{a(t)} = \dot{H}(t) + H^2(t) = \frac{4\pi G}{3}(\rho + 3\mathcal{P}). \tag{1.4}$$

Here κ is defined as before, ρ is equal to the summed density of all the constituents of the universe[5], $\mathcal{P}$ is equal to the pressure, and over-dot notation is used to indicate derivatives with respect to t. We see from equation 1.3 that $\rho > \rho_{crit}$ implies that $\kappa = 1$ and space is positively curved, $\rho < \rho_{crit}$ implies that $\kappa = -1$ and space is negatively curved, and $\rho = \rho_{crit}$ implies that $\kappa = 0$ and space is flat.

A tremendous amount of detail and intellectual effort is hidden by this summary, but it describes the theoretical picture of the expanding universe in its simpliest form. We are left with differential equations that determine $a(t)$ in terms of the density ρ and pressure $\mathcal{P}$ which homogeneously and isotropically fill space. In fact, we see that a flat universe will continue to expand as long as it maintains some energy density.

In 1927, Edwin Hubble published his studies of Cepheid variables indicating that galaxies were receding away from us at a rate ($\vec{v}$) proportional to their distance ($\vec{r}$) [6], at which time the framework outlined above was already understood [7]. Hubble's law $\vec{v} = H\vec{r}$ is exactly what would be expected in a homogeneous and isotropic universe with $\dot{a}(t) = a(t)H$, with H constant[6]. It was thus possible to

[4]The second equality generally holds only for a specific choice of normalization for $a(t)$. For $\kappa = \pm 1$, $a(t)$ must take on values that reflect the curvature of the universe. For $\kappa = 0$, $a(t)$ may be fixed to an arbitrary value at a given time [4]. Typically this is chosen so that $a(\text{now}) = 1$.

[5]For ΛCDM this means matter (both dark and normal), radiation, and dark energy.

[6]This is of course where H gets its name, although it is now known to not be constant.

attribute the observed recession to a global expansion of the universe of the sort described by $a(t)$ instead of to some special location of the Earth or the Milky Way.

The implications of this interpretation are striking. Both the history and fate of the universe are determined by the equations for $a(t)$ and how the elements composing ρ and $\mathcal{P}$ respond to changing physical distances of the space they inhabit. Reversing the picture, it is possible to envision the universe as it must have existed in a much smaller, hotter, and denser form.

1.2 The CMB

With the experimental detection of and theoretical explanation for the expanding universe, it became possible to theorize about observable consequences of the universe beginning in a much more compact form. While we will focus here on the CMB, there have been other significant areas of investigation, not the least of which is Big Bang nucleosynthesis (BBN). The correct prediction of elemental abundances that were created in the early universe is a great triumph[7] of the Big Bang theory. In fact, it was in the context of early investigations into BBN that Gamow, Alpher, and Herman initially predicted the existence of the CMB [9, 10], though they only predicted an energy density for the radiation and seem not to have appreciated its spectral characteristics, nor that it would be observable [11]. Russian physicists Doroshkevich and Novikov predicted early in 1964 [12] that the CMB would have a black body spectrum, that it should be detectable, and in fact suggested that a particular Bell Laboratories antenna located at Crawford Hill, New Jersey would be a suitable instrument for detecting it.

Later that same year, Penzias and Wilson made their now famous serendipitous discovery of this radiation [13] using the very antenna identified by Doroshkevich and Novikov[8].

This radiation was understood [14] to have been produced in the early hot

[7]Except for lithium; see i.e. [8].

[8]Though an English translation of the work was published, it was not noticed in the West until later and Penzias and Wilson were unaware of it at the time of their discovery.

and dense universe: photon energies and number densities were high enough to maintain the matter in the universe in an ionized state. As the universe expanded and cooled, the radiation could no longer maintain the ionization, electrons "recombined[9]" with protons, and the photons began to free-stream through the universe as their mean free paths grew to be larger than the causal horizon of the universe. We will return to this picture below.

In their paper, Penzias and Wilson describe the radiation as 3.5K $\pm$ 1K and isotropic. The isotropy of the radiation is a key feature: the radiation must be nearly isotropic in order for the FLRW metric to be a reasonable description of the universe. However, in order for gravitational instability to have led to the structures we observe in the modern universe there must have been some variations in density, which can be shown to lead to variations in the observed temperature [16]. The detection of the CMB thus began a nearly thirty year quest to find this anisotropy.

In 1992, the Cosmic Background Explorer (COBE) satellite experiment succeeded in detecting these spatial anisotropies with its Differential Microwave Radiometer (DMR) instrument [17]. The Far Infared Absolute Spectrometer (FIRAS) instrument on the same satellite measured the spectrum of the CMB to be a nearly perfect blackbody at 2.725K $\pm$ 0.002K [18, 19]. The Nobel committee, in awarding the Nobel Prize for the work done with FIRAS and DMR, proclaimed that these measurements "marked the inception of cosmology as a precise science."

The anisotropies that COBE DMR detected in the CMB are on the order of 10^{-5}. The incredible uniformity of the early universe is a crucial feature, allowing the coupled nonlinear Einstein and Boltzmann equations needed to describe the evolution of the early universe to be handled within the framework of linear perturbation theory. That is, because the universe used to be so close to homogeneous and isotropic, we can use those assumptions as a starting point to understand more complicated behavior. While the most striking feature of the CMB is its incredible uniformity, an understanding of how anisotropies in the CMB today originate from

[9]This odd choice of terminology (electrons and ions are stably combining for the first time!) originates from the study of HII regions where electrons and ions are continuously "recombining" [15].

inhomogeneities in the early universe is what has made the CMB such a powerful tool.

1.2.1 Deviations from the Cosmological Principle

In order to account for the subtle anisotropies and inhomogeneities that must have been present in the early universe, it is necessary to introduce the perturbations $\Psi(\vec{r},t)$ and $\Phi(\vec{r},t)$ into the metric [5] (*cf.* equation 1.1):

$$ds^2(t,\vec{r}) = -(1+2\Psi(t,\vec{r}))dt^2 + a^2(t)(1+2\Phi(t,\vec{r}))(dx^2+dy^2+dz^2) \tag{1.5}$$

where we have now chosen to describe only flat space[10] ($\kappa = 0$), a choice which is justified observationally. Here Ψ corresponds to perturbations to the Newtonian potential, and Φ corresponds to perturbations to the spatial curvature.

Because we know that these time and space dependent deviations from isotropy are small, the approach that is taken to understand the evolution of the early universe is to solve for the dynamics keeping terms to linear order in Φ and Ψ.

This linearity allows solutions to the time-evolution of the perturbation fields to be simplified even further. The initial conditions $\Phi(t_0,\vec{r})$ and $\Psi(t_0,\vec{r})$ can be expanded into a set of complete basis functions whose time-evolution is simpler to calculate, and then the results can be understood as the sum of the time-evolved basis functions [20], e.g. for the spatial curvature we can write:

$$\begin{aligned} \Phi(t_0,\vec{r}) &= \sum_k \phi_k f_k(\vec{r}) \\ \Phi(t,\vec{r}) &= \sum_k \phi_k F_k(t,\vec{r}) \end{aligned} \tag{1.6}$$

with F_k a solution to the linearized governing equations and with $F_k(t_0,\vec{r}) = f_k(\vec{r})$.

There are many possible choices for f_k. In the CMB community it is most common to choose harmonic plane waves as a basis so that $f_{\vec{k}} \propto e^{i\vec{k}\cdot\vec{r}}$, making the ϕ_k Fourier coefficients. The dynamics of each Fourier mode can then be tracked

[10] This expression also ignores vector and tensor modes for simplicity.

independently. This choice of basis is particularly convenient because the time dependence factors out as:

$$F_{\vec{k}}(t,\vec{r}) = T_k(t) f_{\vec{k}}(\vec{r}) \tag{1.7}$$

where T_k is known as the transfer function. A fair amount of physical intuition can also be gained from looking at the solutions in this form. Another choice of basis function is:

$$f_k(\vec{r}) = \delta_D^{(3)}(\vec{r} - \vec{r}_k) \tag{1.8}$$

where $\delta_D^{(3)}$ is the three dimensional Dirac delta function corresponding to a point-like perturbation in real space. Results from this basis are useful for generating a somewhat different intuitive picture [20,21]. What must be done with any choice of basis is to determine how initial perturbations evolve with time - that is, determine $F_k(t,\vec{r})$.

1.2.2 Time Evolution of Perturbations

For a given k-mode in the Fourier basis, the Einstein equations can be used to determine how the metric perturbations Φ and Ψ evolve with time. This can be shown to be [22, 23]:

$$k^2\Phi + 3\frac{\dot{a}}{a}\left(\dot{\Phi} - \frac{\dot{a}}{a}\Psi\right) = -4\pi G a^2 \delta\rho k^2 \left(\dot{\Phi} - \frac{\dot{a}}{a}\Psi\right) = 4\pi G a^2 \delta p \tag{1.9}$$

where $\delta\rho$ and δp are the perturbations to the total density and momentum fields, with contributions from each individual species indexed by j: $\delta\rho = \sum_j \delta\rho_j$ and $\delta p = \sum_j \delta p_j$ where $\delta\rho_j$ and δp_j are perturbations to all the different species that contribute to energy and momentum densities in the unvierse. In the above equations the dot notation has now been used to denote derivatives with respect to conformal time $\eta(t) \equiv \int_0^t \frac{dt'}{a(t')}$ for convenience, and we will now make the switch to using η as our time coordinate. We then need to establish what components of the universe contribute to the density and momentum perturbations and account for how these perturbations interact with each other and with the metric.

For ΛCDM the different species that contribute[11] to $\delta\rho$ and δp are: photons, normal matter (ions and electrons), cold dark matter, and neutrinos[12] [23]. The interactions of these species with each other and with the metric is handled via the Boltzmann equation. The Boltzmann equation deals with phase-space distribution functions $f(\eta, \vec{r}, \vec{p})$, where f is a product of probabilities for a particle to exist at a particular point in space ($\vec{r}$) and to have a particular momentum ($\vec{p}$) at that point at a given time η.

For instance, if we parameterize the photon distribution by its temperature T we can define the photon perturbation field $\Theta(\eta, \vec{x}, \vec{n}) \equiv \frac{\delta T}{T}(\eta, \vec{x}, \vec{n})$ where the direction $\vec{n}$ now plays the role of momentum. Letting:

$$\Theta(\eta, \vec{x}, \vec{n}) = \int \frac{d^3k}{(2\pi)^3} e^{i\vec{k}\cdot\vec{x}} \Theta(\eta, \vec{k}, \vec{n}) \tag{1.10}$$

we can construct a differential equation for $\Theta(\eta, \vec{k}, \vec{n})$ that describes the interactions between photons and electrons via Thomson scattering as well as interactions with the metric perturbations which affect photon energies via the expansion of space or gravitational redshifting.

Exact Results

We are interested in comparing to measurements of the CMB, and so calculating Θ today is our primary aim. However, the photon field couples to electrons and the metric and because these are coupled in different ways to all the other perturbations, systems of differential equations describing the time evolution of the distribution functions for all the perturbations must be solved simultaneously. To achieve the accuracy required to compare to actual measurements these equations must be solved numerically. The required equations and techniques for achieving rapid and accurate numerical solutions are described in [22–25]. Software packages are used to compute observable quantities today given the spectrum of initial

[11] Note that while dark energy (Λ) is currently the dominant energy component in the universe, it is not perturbed in the ΛCDM model and is only part of the homogeneous background evolution.

[12] Models that include massive neutrinos effectively treat them as a warm dark matter contribution [24].

perturbations. While numerical calculations are required for comparison to experiment, a qualitative picture can also provide some insight.

Interpretation

When the temperature T of the photon field is sufficiently high, enough photons have energies above the $\chi = 13.6$ eV ionization energy of hydrogen to maintain the baryons in a completely ionized state. As the universe expands, T drops ($T \propto \frac{1}{a}$) because photon energies are redshifted due to expansion. When $T \ll \chi$ the universe ceases to be ionized and the photons "free-stream" through the universe. With some important exceptions to be discussed later, the features we observe in the CMB today were formed before this process of "recombination" as the universe became neutral for the first time. The point at which recombination occurs is largely a function of temperature.

The largest scale k-modes that affect the Θ which we observe today had a wavelength longer than the causal horizon of the universe at recombinaiton. These long wavelengths were thus not subject to causal evolution before recombination and so reflect the initial[13] perturbations. An initial perturbation that increases the density[14] ρ will increase the gravitational potential perturbation Ψ. This leads to two effects: 1) there is a gravitational redshift effect due to photons leaving the potential well of the perturbation with $\frac{\delta T}{T} = \Theta = \Psi$ and 2) there is a time dilation effect caused by the potential well that delays the time at which the plasma recombines and leads to an offset term of $\Theta = -\frac{2}{3}\Psi$ [15]. The result is:

$$\frac{\delta T}{T} = \Theta = \frac{\Psi}{3} \tag{1.11}$$

as a perturbation in the temperature field that we observe today. This is known as the *Sachs-Wolfe* effect [16].

At k-scales where the wavelengths of modes are smaller than the causal

[13]Post-inflation, if inflation is the correct theory of the early universe.

[14]A perturbation to the density that does not affect the relative number densities of species being considered is called *adiabatic*, whereas *isocurvature* perturbations affect relative number densities without affecting overall density. Current observations are consistent with only adiabatic perturbations being present [26].

horizon at recombination, the picture is more complicated. These modes are affected by causal physics and altered from their initial state prior to recombination. Well before recombination, the scattering rate of photons off electrons is high, and the result is that the photons and baryons are "tightly coupled". The competing influences of gravity and photon pressure lead to acoustic effects in the photons and baryons, which in the tightly coupled limit can be treated as a single fluid [5].

In the Fourier-mode decomposition, the result is oscillating acoustic waves whose crests are hot, over-dense regions and whose troughs are cold, under-dense regions. In the simplest approximation the amplitude of these perturbations oscillate in time like $\cos[kr_s(\eta)]$ or $\sin[kr_s(\eta)]$ depending on initial conditions. Here r_s is the sound horizon:

$$r_s(\eta) \equiv \int_0^\eta d\eta' c_s(\eta'), \tag{1.12}$$

with c_s the speed of sound, which is also a function of time because it depends on the ratio of photon and baryon densities. These waves oscillate in time until recombination, when the photons no longer provide pressure to drive the oscillations and the acoustic behavior ceases [5].

The picture in the position-space basis with a point like perturbation is even simpler: a spherical shell of photon and baryon over-density expands outward at the sound speed c_s from the initial point until recombination. More precise calculations show dispersion in the expanding shell, but lead to a similar qualitative picture [20, 27]. The physics in this picture is identical to the oscillating plane waves, merely expressed in a different basis. In both cases, the sound horizon r_s at recombination plays a crucial role in determining the anisotropies that are encoded in the photons as they free-stream away after recombination.

We expect anisotropy to be enhanced at k-scales where the oscillating plane waves have reached a maximum or a minimum at recombination ($k = n\pi/r_s$, $n = 1, 2, ...$)[15], or equivalently at the scale of the sound-horizon in real space. We are able to measure these effects today because they are imprinted on the photon

[15]Here we have assumed only the cosine mode is present, which, as predicted by inflation, is consistent with observations.

field at last scattering, generating the anisotropies in the CMB we measure today.

In most literature, the temperature anisotropies we observe today are described as a result of the photon-baryon fluid being either hotter or colder than the unperturbed background at the time of recombination. This is a paradox: the timing of recombination in a given region of space is a function of the temperature there, and thus cold regions recombine earlier and hot regions recombine later. All recombination happens at the same photon temperature[16], and thus hot and cold regions emit photons of the same temperature as they recombine. The reason that information about the inhomogeneities is preserved is because the universe is expanding: regions that are colder recombine first and are thus more redshifted and correctly appear colder; regions that are hotter recombine later and are thus less redshifted and appear hotter [15].

Given an exact distribution of initial inhomogeneities, we could predict the map of the full CMB sky as we observe it today. However, because we have no knowledge of the precise initial conditions, the meeting point between theory and experiment must be chosen elsewhere.

The initial inhomogeneities (perturbations) are predicted to be Gaussian random fluctuations that are nearly independent of the spatial scale k, and this prediction is in good agreement with current observational evidence. These inhomogeneities are processed until last scattering as described above, leaving some spatial scales with enhanced inhomogeneities relative to others. With the assumption of initial Gaussian fluctuations and an understanding of how physics affects the growth or suppression of those inhomogeneities before last scattering, it is possible to predict statistical properties of the observed anisotropies today, serving as a point for comparison between theory and experiment. In the CMB community, the meeting point is chosen to be the power spectrum of the anisotropies, which is the spherical harmonic transform of the two-point angular correlation function on the sky.

[16]The conditions for recombination are also weakly dependent on density, but higher density serves to delay recombination and lower density to advance it, which does not solve the paradox.

1.2.3 CMB Power Spectra

The power spectrum of the full sky is based on the spherical harmonic transform. We begin by transforming a single field as measured on the sky. For instance, in the case of the temperature anisotropies, the full sky anisotropies $\Theta(\theta, \phi)$ are represented as:

$$\Theta(\theta, \phi) = \sum_{\ell=1}^{\infty} \sum_{m=-\ell}^{\ell} a_{\ell m}^{T} Y_{\ell m}(\theta, \phi), \tag{1.13}$$

where the T in $a_{\ell m}^{T}$ represents temperature, and $Y_{\ell m}(\theta, \phi)$ are the standard spherical harmonics functions which are normalized as:

$$\int d\Omega Y_{\ell m}(\theta, \phi) Y_{\ell m}^{*}(\theta, \phi) = \delta_{\ell \ell'} \delta_{m m'}. \tag{1.14}$$

$a_{\ell m}^{T}$ represents the strength of the temperature anisotropy in a particular spherical harmonic $Y_{\ell m}$. The angular period of a single harmonic mode is given by ℓ, with the approximate relationship that the number of periods over the full sphere is given by $\frac{360^{\circ}}{\ell}$. The parameter m relates to the orientation and phase of the modes with respect to the sphere.

For our theoretical sky, each coefficient $a_{\ell m}$ is drawn from a Gaussian distribution of mean zero and a variance related to the expected level of anisotropy at the given angular scale ℓ. All values of $a_{\ell m}$ at a given ℓ are drawn from the same distribution [5]. Of course, an important task of experiments is to confirm this assumption of Gaussianity; thus far no evidence of non-Gaussianity originating from last scattering has been found [28]. For a truly Gaussian field, the only quantity left to characterize is then the variance of the modes at a particular angular scale ℓ. The power spectrum is an estimate of that variance. We define the power spectrum C_{ℓ} as:

$$C_{\ell} = \frac{1}{2\ell + 1} \sum_{m=-\ell}^{\ell} a_{\ell m} a_{\ell m}^{*} = \langle a_{\ell m} a_{\ell m}^{*} \rangle, \tag{1.15}$$

and in particular for the temperature power spectrum:

$$C_\ell^{TT} = \frac{1}{2\ell+1}\sum_{m=-\ell}^{\ell} a_{\ell m}^T a_{\ell m}^{T*} = \langle a_{\ell m}^T a_{\ell m}^{T*} \rangle. \tag{1.16}$$

An example measurement of the C_ℓ^{TT} power spectrum along with the best fit ΛCDM theory curve are shown in figure 1.1. It is typical to plot the power spectra normalized by the factor $\ell(\ell+1)/2\pi$, as is done in figure 1.1. This "flattens" the spectra, making it decay more slowly as a function of ℓ, and makes the acoustic features more visible.

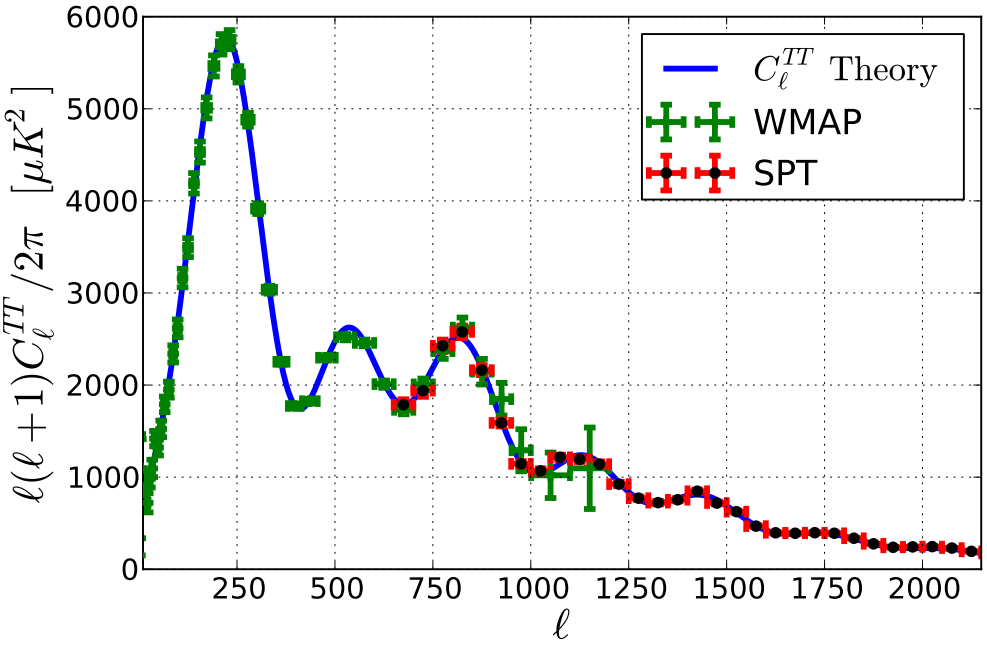

Figure 1.1: The CMB C_ℓ^{TT} power spectrum as measured by the WMAP [29] and SPT [30] experiments. The WMAP measurements are shown in green and the SPT measurements in red. A fit to the ΛCDM model is shown with a blue solid line.

The clearly visible peak structure in figure 1.1 corresponds to the enhanced inhomogeneity at different k scales where the Fourier modes have reached maxima or minima at the surface of last scattering, as described above. It is interesting to note that when viewed as an angular correlation function, the multiple peaks seen in the power spectrum correspond to a single peak at the scale of the acoustic horizon at last scattering. The shape of the single correlation function peak con-

tains the same information that is extracted from the multiple harmonics seen in the power spectrum [31].

When measuring small portions of the sky, as an experiment such as POLARBEAR does, the spherical harmonic transform can be approximated as a Fourier transform. This both simplifies the calculations and provides a more intuitive picture of what each mode represents. The use of Fourier space also greatly simplifies the representation of CMB polarization, as we will see later. 2D Fourier space can be conveniently represented on a plane in polar coordinates. Each point on the 2D Fourier plane represents a mode in the power spectrum, equivalent to a value of $a_{\ell m}a^*_{\ell m}$, with the radial coordinate $\ell = 2\pi|\vec{k}|$ and azimuthal coordinate $\varphi_{\vec{\ell}}$. ℓ specifies the period of each mode and $\varphi_{\vec{\ell}}$ specifies the orientation angle of the wave vector for the mode. An example of this representation, generated via simulation, is shown in figure 1.2 for the TT power spectrum. In this case the value of C_ℓ^{TT} can be formed as an azimuthal average over rings at radius ℓ. We will use notation like:

$$C_\ell^{TT} = \langle TT^* \rangle_{\varphi_{\vec{\ell}}} \tag{1.17}$$

to indicate this azimuthal averaging process. Equation 1.17 serves as the equivalent of equation 1.16 in flat space.

The C_ℓ^{TT} power spectrum has been well characterized, and fitting model parameters to the peak structure has lead to the firm establishment of ΛCDM as the leading theory of cosmology. We now turn our focus to the polarization of the CMB.

1.3 Polarization of the CMB

Similar to the temperature anisotropies, any polarization generated at last scattering will be preserved in the radiation field reaching us today. Measuring polarization anisotropies can provide a powerful additional window into the physics of the early universe. We first introduce terminology required to characterize polarization in the context of CMB measurements, and then discuss mechanisms

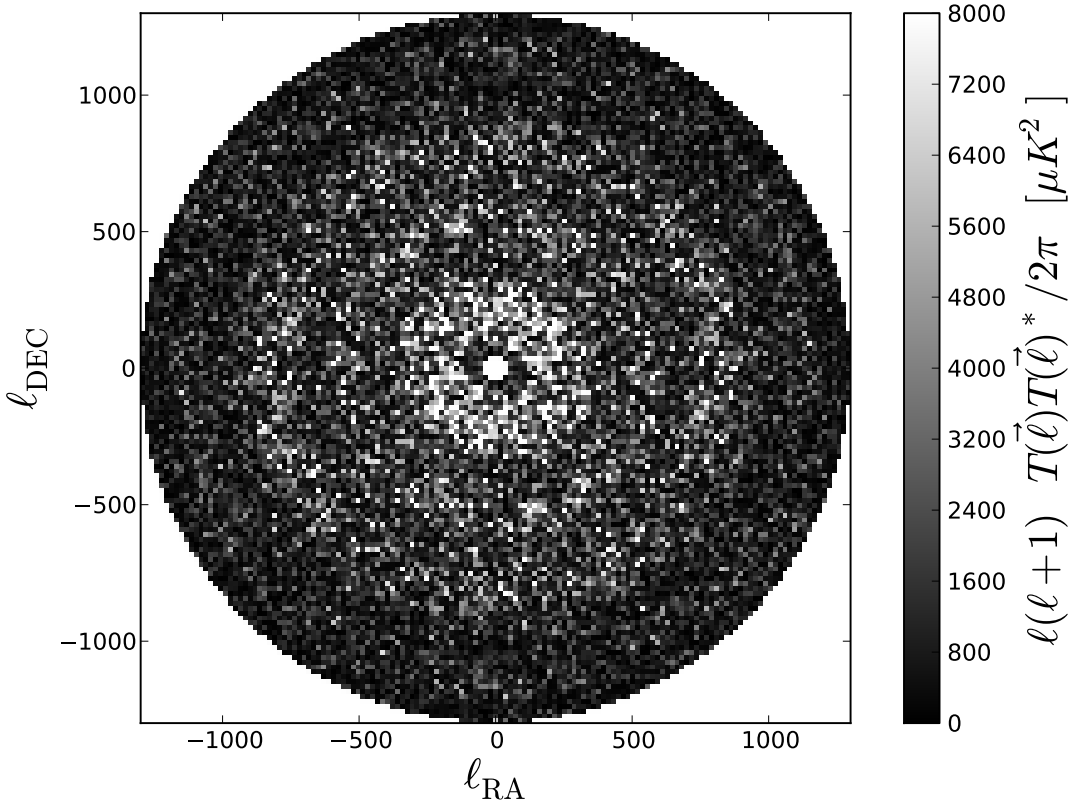

Figure 1.2: A simulated TT power spectrum in 2D Fourier space. The first four acoustic peaks are visible as azimuthally symmetric areas with higher values. The region outside of $50 < \ell < 1700$ is masked out. The resolution shown represents the actual number of Fourier modes that would be sampled on a $20^\circ \times 20^\circ$ region of the sky.

for generating polarization in the CMB.

1.3.1 Polarization Representation

Polarization can be characterized at each point on the sky by both a magnitude and an angle describing the direction of polarization. In the CMB field, the Stokes parameters are typically used to represent polarization. In terms of the electric field strength along two axes x and y, the four Stokes parameters are [32]:

$$
\begin{aligned}
I &= |E_x|^2 + |E_y|^2, \\
Q &= |E_x|^2 - |E_y|^2, \\
U &= 2\mathrm{Re}(E_x E_y^*), \\
V &= -2\mathrm{Im}(E_x E_y^*).
\end{aligned}
\tag{1.18}
$$

The Stokes parameter I represents the total power in the radiation field, and Q and U represent the linear polarization. V represents circular polarization which is not expected in the CMB and most CMB polarization experiments, including POLARBEAR, do not measure it. The simple geometric interpretation of Q and U, that each can be treated as the difference in polarized power oriented along orthogonal sets of axes, is shown in figure 1.3.

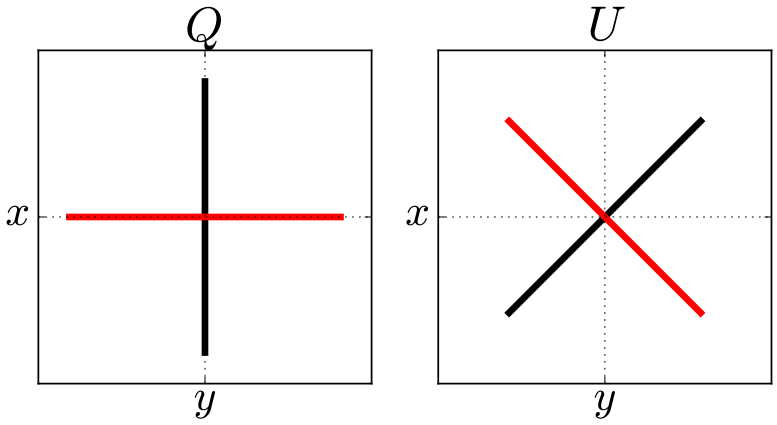

Figure 1.3: A visualization of the Q and U Stokes parameters. Q is shown on the left: positive Q (red) is proportional to polarized power along the x-axis and negative Q (black) is proportional to polarized power along the y-axis. U is shown on the right: it is defined identically to Q on a set of axes rotated by 45° with respect to the x- and y-axes.

The linear polarization at any point can be represented as a linear combination of Q and U, so that measuring Q and U at each point corresponds to a full measurement of the linear polarization. Because sky maps are typically shown in terms of right ascension (RA) and declination (DEC), we align the definition of Q and U to these coordinates, choosing positive Q to run along RA and negative Q to run along DEC.

We now seek a way to construct power spectra of CMB polarization using equation 1.15, analogous to what was done in equation 1.16 for temperature. We thus need to form Fourier transforms of polarization quantities. Directly transforming Q and U results in quantities representing polarization angles in a basis fixed to the coordinates because the definition of Q and U is coordinate system dependent. For comparison between theory and experiment, it is necessary to define quantities which characterize polarization in a way that is not coordinate system dependent. This transformation to coordinate independent quantities can also be done in a way that nicely separates physical mechanisms for generating the polarization.

1.3.2 E and B Decomposition

We begin by forming the 2D Fourier transforms of $Q(\vec{x})$ and $U(\vec{x})$, which we will call $Q(\vec{\ell})$ and $U(\vec{\ell})$. These quantities represent Fourier transforms of the polarization with the orientation of the polarization of a particular Fourier mode fixed to the coordinates in which the transform is done. As an alternative, we may choose to fix the polarization orientation of a particular Fourier mode relative to the orientation of its wave vector. With this choice, the amplitude of the Fourier mode is fixed with respect to the coordinate system in which polarization angles are measured.

As a particular choice of such a system, we can define E-modes to be those with polarization orientations fixed to be parallel or perpendicular to their wave vectors, and the complimentary B-modes to be those with polarization orientations fixed at $\pm 45^\circ$ relative to the wave vector. This choice of basis completely represents linear polarization, just as Q and U do, but does so in a coordinate independent way.

With these definitions, $E(\vec{\ell})$ and $B(\vec{\ell})$ may be found from $Q(\vec{\ell})$ and $U(\vec{\ell})$ via:

$$\begin{aligned} E(\vec{\ell}) &= Q(\vec{\ell})\cos(2\varphi_{\vec{\ell}}) + U(\vec{\ell})\sin(2\varphi_{\vec{\ell}}) \\ B(\vec{\ell}) &= -Q(\vec{\ell})\sin(2\varphi_{\vec{\ell}}) + U(\vec{\ell})\cos(2\varphi_{\vec{\ell}}), \end{aligned} \tag{1.19}$$

and the inverse operation of transforming from $E(\vec{\ell})$ and $B(\vec{\ell})$ to $Q(\vec{\ell})$ and $U(\vec{\ell})$ is performed as [33]:

$$\begin{aligned} Q(\vec{\ell}) &= E(\vec{\ell})\cos(2\varphi_{\vec{\ell}}) - B(\vec{\ell})\sin(2\varphi_{\vec{\ell}}) \\ U(\vec{\ell}) &= E(\vec{\ell})\sin(2\varphi_{\vec{\ell}}) + B(\vec{\ell})\cos(2\varphi_{\vec{\ell}}). \end{aligned} \tag{1.20}$$

An example of single E- and B-modes represented in real space, along with their accompanying polarization orientations, is shown in figure 1.4.

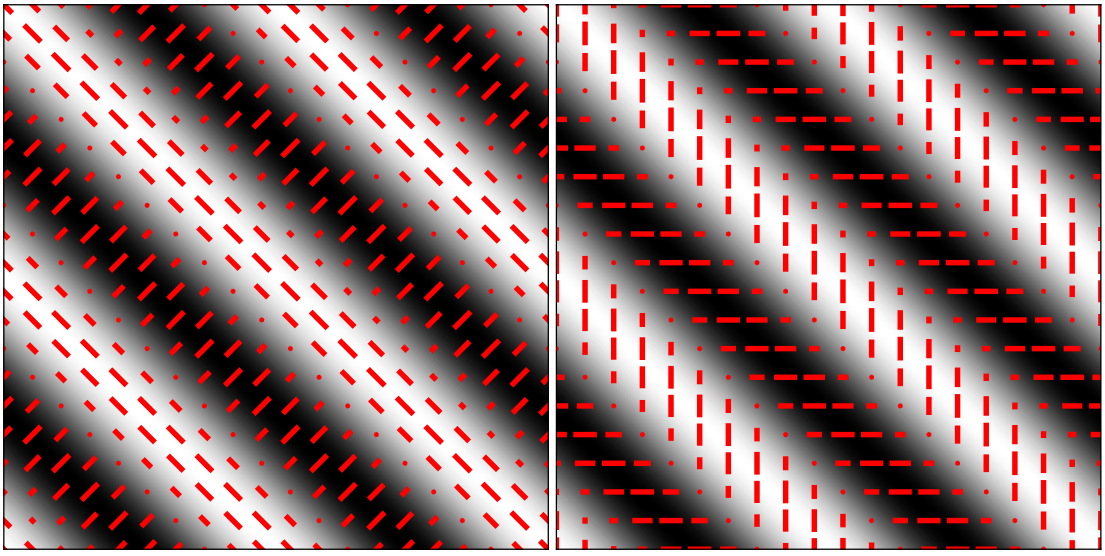

Figure 1.4: Example E- and B-modes. The amplitude of either E or B at each point is shown with a black (negative) and white (positive) color scale. The direction of polarization associated with each point is shown in red. The left panel shows an example of an E-mode, characterized by polarization directions oriented parallel or perpendicular to the wave vector of the mode. The right panel shows an example of a B-mode, characterized by polarization directions oriented at $\pm 45°$ relative to the wave vector of the mode.

The nature of E and B polarization is non-local: it is not possible to make a measurement of polarization at a single point in space and characterize it as either E or B. Therefore measurements of polarization are performed as measurements of Q and U, but these are converted to E and B over the part of sky under consideration before comparison with theoretical expectations. Measurements of $E(\vec{\ell})$ and $B(\vec{\ell})$ can be azimuthally averaged to produce C_ℓ^{EE} and C_ℓ^{BB}, as was done for $T(\vec{\ell})$ in equation 1.17, which again is the meeting point for theory and

experiment. More generally, we may also investigate cross-power spectra between the different fields as:

$$C_\ell^{XY} = \langle XY^* \rangle_{\varphi_{\vec{\ell}}} \tag{1.21}$$

with $X, Y \in [T, E, B]$.

1.3.3 Generation of Polarization in the Primordial CMB

Shortly before last-scattering, electrons and photons are interacting via Thomson scattering. For certain patterns of unpolarized but anisotropic incoming radiation, Thomson scattering can induce a net polarization in the scattered radiation.

Defining the outgoing radiation we receive today to be directed along $\hat{n}$ with polarization $\hat{\epsilon}_i$ and incoming radiation from direction $\hat{n}'$ with polarization direction $\hat{\epsilon}'_j$, the differential cross section for Thomson scattering is [32]:

$$\frac{d\sigma}{d\Omega} = \left(\frac{e^2}{mc^2}\right)^2 |\hat{\epsilon}_i(\hat{n}) \cdot \hat{\epsilon}'_j(\hat{n}')|^2. \tag{1.22}$$

By summing over the two incoming polarization directions at each direction $\hat{n}'$ and integrating over all directions of incident radiation with an intensity $f(\hat{n}')$ dependent on the incoming direction, it can be shown [5] that the net polarization of the outgoing radiation is proportional to the spherical harmonic quadrupole of f. Thus Thomson scattering will produce net linear polarization if and only if the scattering electron is surrounded by a radiation field with a quadrupole intensity pattern.

The oscillating acoustic waves generated by the perturbations discussed above produce such quadrupole patterns, and this is the dominant mechanism for generating CMB polarization. It can be shown [5] that an individual 3D Fourier mode of a density perturbation will generate a quadrupole pattern with maxima and minima out of phase with the density maxima and minima. These quadrupole moments are always oriented such that the polarization scattered toward an observer is parallel or perpendicular to the Fourier mode wave vector. This is because

the scalar density perturbations have no property that breaks the symmetry around the axis perpendicular to the wave vector. The same will hold true in projection on the sky: the polarization orientation will remain parallel or perpendicular to the orientation of the 2D wave vector. Thus the polarization generated by density perturbations can only be E-mode polarization, and any observed B-mode polarization must be generated by a different physical effect.

The temperature fluctuations and E-mode polarization are produced by the same physical mechanisms, though they are out of phase. We therefore expect to see acoustic peak structure in C_ℓ^{EE}, and for the T and E fields to be correlated. C_ℓ^{EE} and C_ℓ^{TE} were first measured in 2002 [34] and have been well-characterized by many experiments.

Generation of B-mode Polarization

There are two frequently considered mechanisms for generating B-mode polarization: the presence of gravitational waves at the surface of last scattering [35, 36], and the influence of gravitational lensing of CMB photons between last scattering and our observations today [37,38]. These two mechanisms have distinct signatures which peak at different angular scales.

Gravitational waves at the surface of last scattering lead to quadrupole temperature anisotropies for local electrons, leading to polarization of the scattered light. Unlike the quadrupoles associated with density fluctuations, these quadrupoles produce both E- and B-mode polarization because the helicity states of gravitational radiation break the symmetry around the wave vector axis. The BICEP2 collaboration recently announced a detection of B-modes consistent with expectations for polarization created by gravitational waves generated by inflation [2]. If confirmed, this would be the most direct evidence of the theory of inflation, which posits an exponential expansion of the universe that creates perturbations of the kind described above as well as gravitational waves from quantum vacuum fluctuations. The energy scale of inflation, as implied by the BICEP2 result, would be 2×10^{16} GeV, thirteen orders of magnitude higher than the physics accessible to current particle accelerators [39].

B-modes generated by gravitational lensing are created after last scattering. Lensing-generated polarization was detected shortly before the gravitational wave B-modes [40–43], and are the primary target of measurements described in this dissertation.

1.3.4 Gravitational Lensing of the CMB

Massive large-scale structures between the last-scattering surface and our galaxy deflect the trajectory of CMB photons. This leads to distortions of both the temperature and polarization anisotropies; here we consider the effects on polarization.

In the weak lensing limit, polarization represented on the sky by $Q(\hat{n})$ and $U(\hat{n})$ from a particular direction $\hat{n}$ may be written in terms of the polarized emission at last scattering ($\tilde{Q}$ and $\tilde{U}$) as [38]:

$$[Q \pm iU](\hat{n}) = [\tilde{Q} \pm i\tilde{U}](\hat{n} + \vec{d}(\hat{n})), \tag{1.23}$$

where $\vec{d}(\hat{n})$ represents the angular deflection of photons arriving from direction $\hat{n}$, known as the lensing deflection field. The deflection field represents the integrated history of deflections for each point on the sky. It is related to the line-of-sight integral over the gravitational potential $\Psi(D\hat{n})$ via $\vec{d}(\hat{n}) = \nabla\phi(\hat{n})$:

$$\phi(\hat{n}) = -2\int dD \frac{D_s - D}{DD_s}\Psi(D\hat{n}), \tag{1.24}$$

where D is the comoving distance along the line of sight and D_s is the distance to the last-scattering surface [38]. As can be seen from 1.23, these subtle deflections remap polarization on the sky without rotating it. Qualitatively, we may interpret this effect as redirecting the wave-vector of a mode without re-orienting its polarization, which intuitively explains why gravitational lensing can generate B-mode polarization from primordial E-mode polarization.

More quantitatively, given a single primordial E-mode $E(\vec{\ell}) = \delta(\vec{\ell} - \vec{\ell}')$ we will generate observed E- and B- modes as:

$$\Delta E(\vec{\ell}) = \frac{\cos(2\varphi_{\vec{\ell}\vec{\ell}'})}{(2\pi)^2} W(\vec{\ell}, \vec{\ell} - \vec{\ell}')$$
$$\Delta B(\vec{\ell}) = \frac{\sin(2\varphi_{\vec{\ell}\vec{\ell}'})}{(2\pi)^2} W(\vec{\ell}, \vec{\ell} - \vec{\ell}'), \tag{1.25}$$

with $\varphi_{\vec{\ell}\vec{\ell}'} \equiv \varphi_{\vec{\ell}'} - \varphi_{\vec{\ell}}$ and:

$$W(\vec{\ell}, \vec{\ell} - \vec{\ell}') = -[\vec{\ell} \cdot (\vec{\ell} - \vec{\ell}')]\phi(\vec{\ell} - \vec{\ell}'). \tag{1.26}$$

Thus in general, lensing will create both B-modes and new E-modes from a single primordial E-mode, but with different characteristic patterns in Fourier space. We may integrate over many primordial E-modes using equation 1.25 to create the final ΔE and ΔB we measure. These changes to E and B generated by gravitational lensing correlate E and B across different parts of Fourier space, creating non-Gaussianity. This non-Gaussianity is a key distinction between the B-modes generated by gravitational lensing and the B-modes generated by gravitational waves, which should be Gaussian.

The value of $\langle \phi(\vec{\ell})\phi(\vec{\ell}) \rangle_{\varphi_{\vec{\ell}}} = C_\ell^{\phi\phi}$ may be calculated theoretically using numerical techniques very similar to those used to calculate theoretical CMB power spectra, though also including non-linear corrections for later-time effects [44]. $\phi(\vec{\ell})$ is expected to be Gaussian distributed in the same way the other CMB fields are. At the percent level, the sum of neutrino masses affects $C_\ell^{\phi\phi}$, which will ultimately allow precise measurements of $C_\ell^{\phi\phi}$ to constrain or measure neutrino masses [45].

The theoretical lensing potential predicts the angular deflections $\vec{d}(\hat{n})$ to be on the scale of a few arcminutes, but with correlations of the deflection field on the scale of several degrees. A theoretical value for the correlations between the magnitude of the deflections $C_L^{dd} = [L(L+1)]^2 C_\ell^{\phi\phi}/2\pi$ across different angular scales $|\vec{L}|$ is shown in figure 1.5.

Given knowledge of $C_\ell^{\phi\phi}$ and C_ℓ^{EE}, the induced C_ℓ^{BB} spectrum can be calculated. The ΛCDM prediction for the C_ℓ^{BB} spectrum generated from the gravitational lensing of E-modes is shown in figure 1.6. Measuring this spectrum was a primary target of the first season of POLARBEAR observations.

As can be seen in figure 1.6, the signals POLARBEAR is interested in mea-

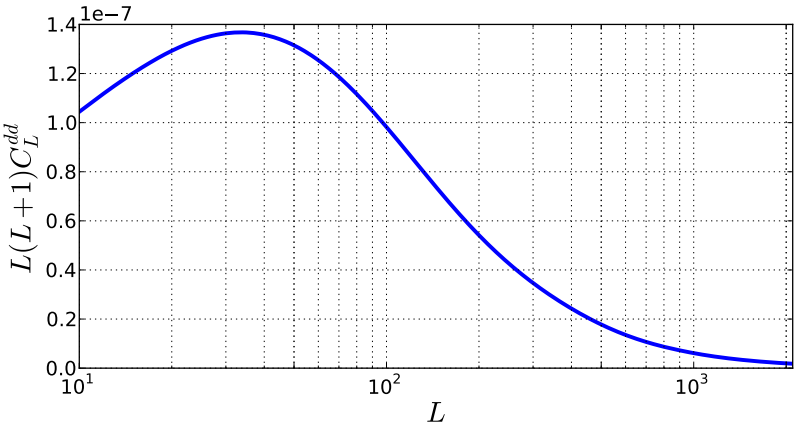

Figure 1.5: The ΛCDM theoretical C_L^{dd} power spectrum, with d in units of radians, created by the distribution of large scale structure in the universe.

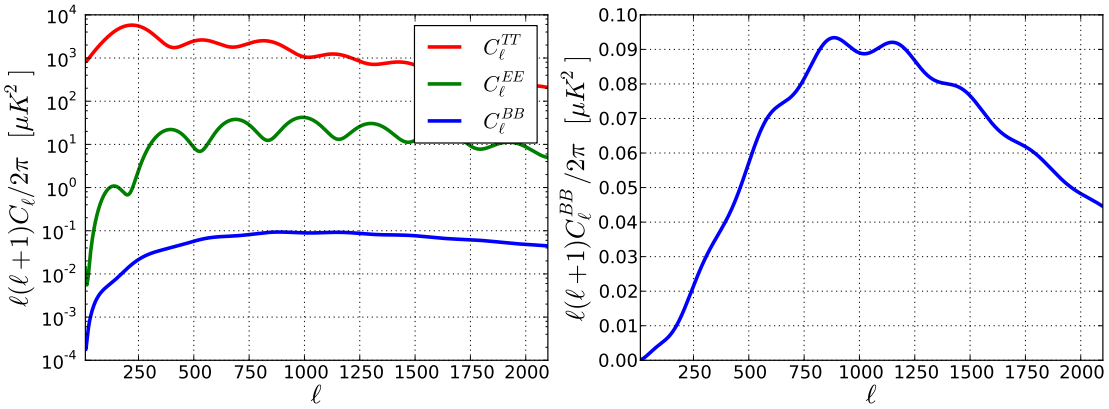

Figure 1.6: The theoretical C_ℓ^{BB}power spectrum induced by gravitational lensing of E-mode polarization. C_ℓ^{BB} is shown on the left with a log scale for comparison to C_ℓ^{TT} and C_ℓ^{EE}. C_ℓ^{BB} is shown alone on the right on a linear scale.

suring (C_ℓ^{BB}) are orders of magnitude lower than those that had been measured when the experiment began (C_ℓ^{TT} and C_ℓ^{EE}). This requires an instrument that is both very sensitive and that has excellent control over systematic errors.

Chapter 2

The POLARBEAR Instrument

POLARBEAR is an experiment designed to measure the CMB B-mode polarization generated by primordial gravitational waves as well as the B-mode polarization generated by gravitational lensing. The first season of POLARBEAR observations has focused on measuring the lensing B-mode signal. The experiment is comprised of a cryogenic receiver (POLARBEAR-1) containing a bolometric focal plane mounted on the Huan Tran Telescope and operates from the James Ax Observatory site in Chile.

2.1 Chilean Observation Site

The Chilean observatory site, known as the James Ax Observatory, is located at latitude -22.958°, longitude 292.214°, and an elevation of over 5,200 meters. Observing from this location in the Atacama desert in northern Chile provides a number of advantages to POLARBEAR. As a ground-based experiment, the most important fundamental noise source that POLARBEAR must contend with is the atmosphere. In the frequency range of interest to POLARBEAR, molecular oxygen and water dominate the atmospheric absorption and emission that the instrument is subjected to. The high altitude, dry site in the Atacama Desert, with precipitable water vapor frequently under 1 mm, is thus one of the best in the world for mm-wave observations. The location in the Southern Hemisphere provides access to the southern sky which has a greater area with low galactic foreground con-

tamination as compared to the northern sky. The latitude of the site means that sky patches of interest rotate in orientation relative to the telescope as they rise and set, allowing the telescope to acquire data from scanning across patches at different angles over the course of an observation. This is in contrast to the South Pole, another prime observation site with arguably better atmospheric conditions, where sky patches do not change orientation as the Earth turns. This variation in scan angle helps to average over systematic effects that would otherwise be a greater source of contamination in the data [46].

2.2 The Huan Tran Telescope

2.2.1 Optical and Mechanical Design

The Huan Tran Telescope (HTT) has an off-axis Gregorian[1] design that satisfies the Mizuguchi-Dragone condition. The Mizuguchi-Dragone condition sets the tilt between the symmetry axes of the conics for the primary and secondary reflectors, and is chosen to minimize cross-polarization and astigmatism over a large diffraction-limited field of view [47, 48]. Off-axis telescopes provide the advantage of unobstructed apertures because they do not need secondary support structures which obstruct the beam, scattering or diffracting light in ways that create potentially polarized sidelobes. The Gregorian-Dragone design is one of the two offset dual-reflector designs that has become common for CMB experiments, the other being the crossed-Dragone. The Gregorian design has the advantage of a smaller secondary as compared to the alternative crossed design. This smaller sub-reflector allows for easier baffling to prevent far sidelobes due to scattering at the receiver window. The smaller secondary also allows for greater mechanical simplicity of the telescope structure. One disadvantage that the Gregorian design suffers from is a smaller diffraction-limited field of view as compared to the equivalent crossed-Dragone design [49].

A ray-traced optical diagram of HTT is shown in Figure 2.1. The primary

[1]The term Gregorian indicates the use of a parabolic primary reflector and elliptic secondary reflector.

and secondary reflectors are visible along with the re-imaging optics and focal plane that are located inside of the cryostat. HTT has a 2.5 meter precision primary reflector that was machined from a single cast piece of aluminum to have a 53μm RMS surface accuracy. A lower precision guard ring, fabricated separately from eight individual panels, extends the surface to 3.5 meters in diameter. Only the precision primary reflector surface is used in the main beam of the instrument, with the guard ring designed to deflect any spillover to the sky. The high surface accuracy and monolithic design of the primary and secondary mirrors limit loss due to both diffuse scattering and polarized scattering that occurs at mirror panel interfaces. The 2.5 meter primary aperture gives a ~ 3.5 arcminute beam at 150 GHz, the central operating frequency of POLARBEAR-1, allowing the experiment to probe up to $\ell \sim 2500$, sufficient for characterizing the peak of the lensing B-mode spectrum at $\ell \sim 1000$.

Also pictured in figure 2.1 are the co-moving ground shield, prime focus baffle, and secondary reflector enclosure. These baffles are designed to prevent stray light from entering the main optical path of the telescope and contaminating the data with signals from the ground. The co-moving ground shield is reflective, while the secondary and prime focus baffles are absorptive. Baffling of the absorptive type fills stray light paths with an absorbing material which contributes optical loading to the detectors but does not introduce time-dependent signals as the telescope scans.

The HTT was constructed by VertexRSI[2]. The mechanical specifications and achieved performance are summarized in Table 2.1.

The only aspect in which performance of the telescope has failed to meet expectations is in pointing reconstruction. We believe that this is at least partly due to a lack of sufficient coverage in pointing measurements to create a better pointing reconstruction model over the azimuth and elevation ranges of POLARBEAR science observations. The true mechanical repeatability limits of the telescope will not be known until more detailed measurements are made. However, on the basis of simulations and potential impact on C_ℓ^{BB} it was decided that the achieved

[2]Now a part of General Dynamics SATCOM Technologies.

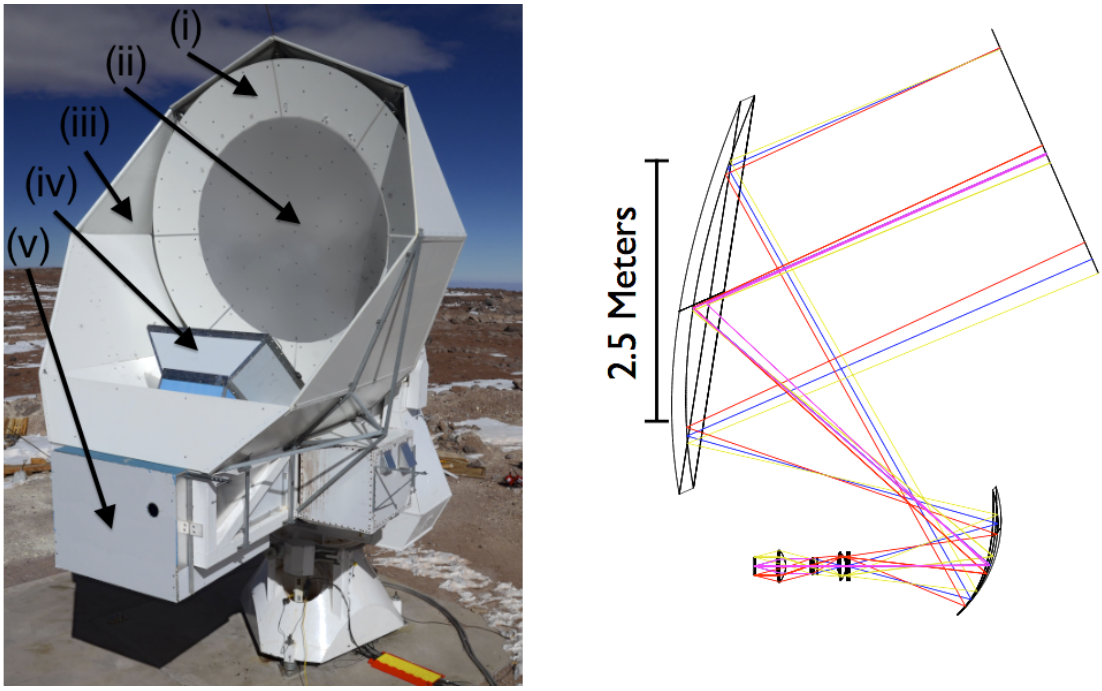

Figure 2.1: **Left:** The Huan Tran Telescope at the James Ax Observatory in northern Chile. Called out in the image are (i) the primary guard ring, (ii) the precision primary mirror, (iii) the co-moving ground shield, (iv) the prime focus baffle, and (v) the secondary reflector enclosure. The secondary reflector and cryostat are not visible because they are surrounded by their respective enclosures. **Right:** A ray-trace schematic of the telescope optics. The focus created by the dual-reflector design is re-imaged by cold optics to the flat focal plane. Figure from [50].

pointing error and associated loss of resolution was acceptable for the first science publications [41–43] and this dissertation.

2.2.2 Thermal Calibration Source

A thermal calibration source is located behind HTT's secondary mirror. A light pipe runs from this source through a small hole in the secondary mirror, allowing the detectors in the cryostat to see the calibration source. The light pipe has a diameter of 0.125 inches and the thermal source is regulated to a temperature of 700° C. The effective intensity of the source varies across the focal plane from about 35-85 mK. A chopper is located between the heat source and the light pipe, allowing the source to be chopped over a range of different frequencies. A polarizer

Table 2.1: HTT mechanical specifications and achieved performance.

Description	Specified	Achieved
Azimuth Travel	$\pm 200^\circ$	$\pm 200^\circ$
Elevation Travel	-1° to $+122.5^\circ$	$+3^\circ$ to $+120^\circ$
Azimuth/Elevation Velocity	$4\ ^\circ/\mathrm{s}$	$4\ ^\circ/\mathrm{s}$
Azimuth/Elevation Acceleration	$2\ ^\circ/\mathrm{s}^2$	$4\ ^\circ/\mathrm{s}^2$
Pointing Reconstruction	10 arcseconds	25-40 arcseconds

can optionally be added to the end of the light pipe and rotated, but this polarizer is not used in normal operations. For more detail about this calibration source and how it is used, see Section 3.1.2.

2.2.3 Observation Strategy

For the first season of observations, POLARBEAR has focused on scanning three different sky patches totaling 30 square degrees. These patches are named "RA4.5," "RA12," and "RA23" based on the approximate RA coordinate of the patch centers. The patches are chosen to have a low level of foreground contamination, provide overlap with data from other experiments, and to maximize the observing efficiency based on the time of day each patch is above the observing horizon of 30° elevation. These sky patches are shown in figure 2.2.

The observation strategy POLARBEAR employs to scan the CMB is to fix a particular center azimuth and elevation and scan back-and-fourth in azimuth around the center point while leaving the elevation of the telescope fixed. We refer to this scan pattern as a constant elevation scan (CES). CESs sample different parts of the sky by allowing the sky patch to drift past as the telescope scans around the chosen central azimuth and elevation. The central azimuth and elevation are chosen to match the central RA and DEC of the sky patch halfway through the CES. Each CES lasts 15 minutes, which is the time required for the sky patch to drift through the scan center.

There are important motivations for scanning the telescope at a constant

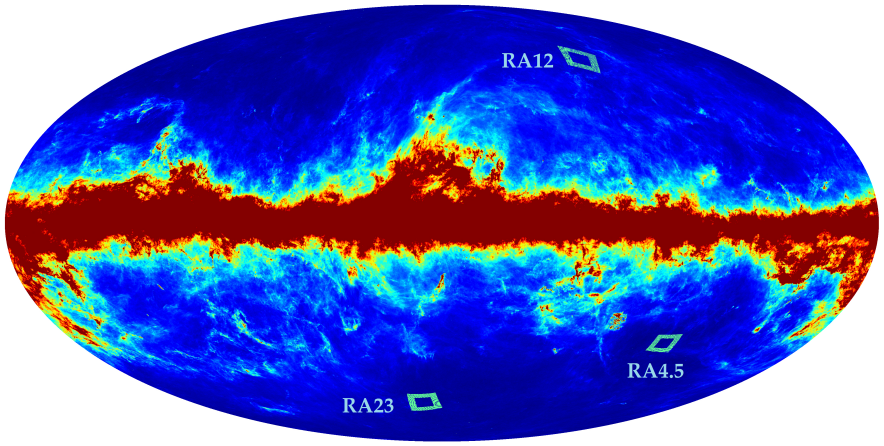

Figure 2.2: The three POLARBEAR sky patches observed during the first season of observations are shown overlaid on a full-sky 857 GHz intensity map from Planck [51]. Figure from [43].

elevation rather than staring at a fixed azimuth and elevation or tracking a fixed point on the sky. Because the amount of atmosphere the telescope looks through is a function of the observation elevation, maintaining a constant elevation helps to fix the amount of power each detector sees due to the atmosphere. CESs also confine signals from stray light on the ground to a small number of Fourier modes in the map; see section 4.5.1 for a discussion of this. Further, the focal plane is laid out in such a way that it must be scanned across the sky in order to Nyquist sample the Fourier modes on the sky [52]. Finally, atmospheric fluctuations cause the noise associated with measuring a particular point on the sky to be highly correlated over short time intervals. It is thus more efficient to measure a particular point on the sky once and return to it after enough time has passed that the noise is uncorrelated rather than make several continuous measurements of a point which would be subject to highly correlated noise.

2.2.4 Telescope Control

Scans

When the telescope scans the sky during a CES, it enters something called "track beam mode." In this mode telescope motion is coordinated with other

systems via a signal called the resource pulse synchronization (RPS). This pulse occurs at a frequency of 95.4 Hz, and the telescope control computer must provide a target azimuth and elevation offset to the telescope servo control system for each pulse period. The scan offsets are specified in terms of the offsets of the bearings along the azimuth and elevation axes relative to the scan center.

Our goal is to perform all CESs at the same azimuth throw and velocity on the sky. Because the azimuth throw on the sky is reduced relative to the bearing throw by a factor of cosine of the elevation, we must use different scans based on the elevation of the CES. We use custom software to generate a set of ten scans (lists of offsets specified every $\sim$10 ms) with different center elevations, and select the closest match for the elevation at which we are observing. A sample scan is shown in figure 2.3. The scans are generated by controlling the "jerk" at each time, where the jerk is defined as the time derivative of the acceleration. Because of the design of the telescope servo control system, the jerk of the scans must be finite. The jerk must be selected to produce the desired acceleration, velocity, and offset in the final scan file. Many of these scans are continuously linked together to form a CES.

Schedules

We use a custom software library that interfaces with the telescope control program to schedule telescope operations. This software is responsible for selecting which type of scan strategy to use based on the scan target, selecting scan centers and the appropriate scan file for CES scans, sequencing the calibration observations such as thermal source measurements and elevation nods with the observations of scan targets, and correctly marking all archived data so that it can be easily processed later. We refer to this software as the "scheduling library" because it is used to control the schedule of telescope operations.

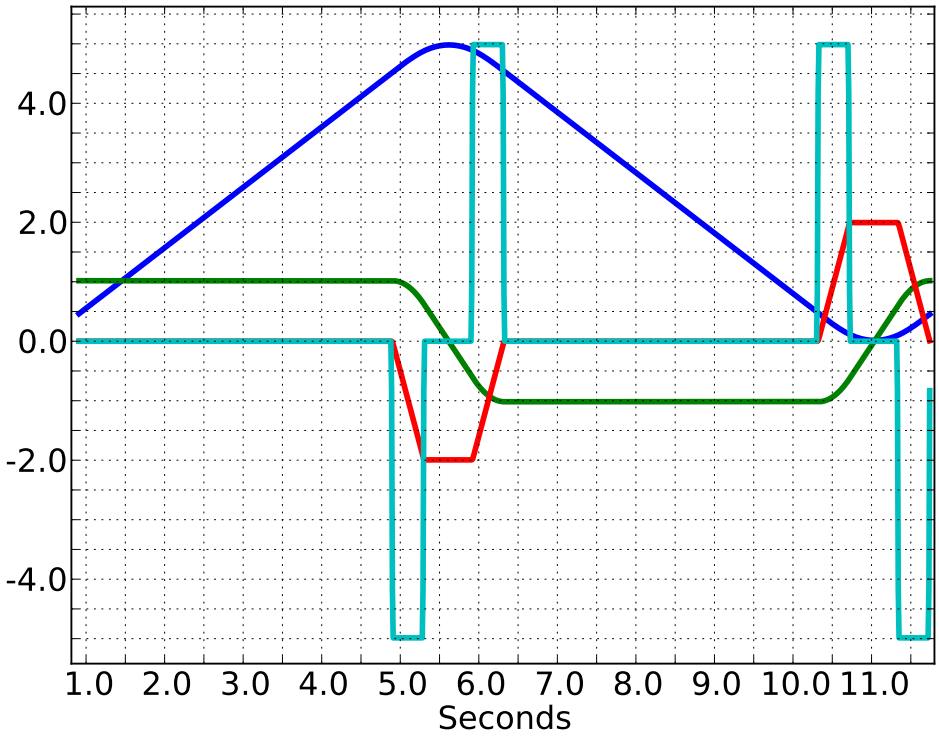

Figure 2.3: The characteristics of one POLARBEAR scan, corresponding to one back and forth motion of the telescope azimuth position. Many copies of these scans are continuously joined together to form a CES. The azimuth offset is shown in blue in units of degrees (°). The velocity is shown in green in units of °/s. The acceleration is shown in red in units of °/s^2. The azimuth jerk is shown in cyan in units of °/s^3. The scan shown here is designed to produce a 3.0° constant velocity sky throw at 0.8 °/s at a center elevation of 42.5°.

2.3 The POLARBEAR Cryostat

There is an intrinsic sensitivity limit for detectors measuring the CMB created by the temporal fluctuations in the rate of photon arrival [53]. In order to reach this limit, detectors must be cooled to the point where their own noise is sub-dominant to this effect. This requires a cryogenic environment to contain the detectors and other readout electronics. Additionally, all elements in the optical chain will be emissive at some level, so that it is impossible to ensure that every photon a detector sees originates from the sky. Because the photon noise contribution is higher for higher temperature emitters, cooling additional components in

the optical chain reduces the photon noise a detector is subjected to. The POLARBEAR cryostat cools the focal plane to less than 0.25 K, cools the SQUID ammeters used for detector readout to under 4 K, and cools other optical elements such as the refractive lenses and rotating half-wave plate (HWP). A cross-section of the POLARBEAR cryostat is shown in figure 2.4.

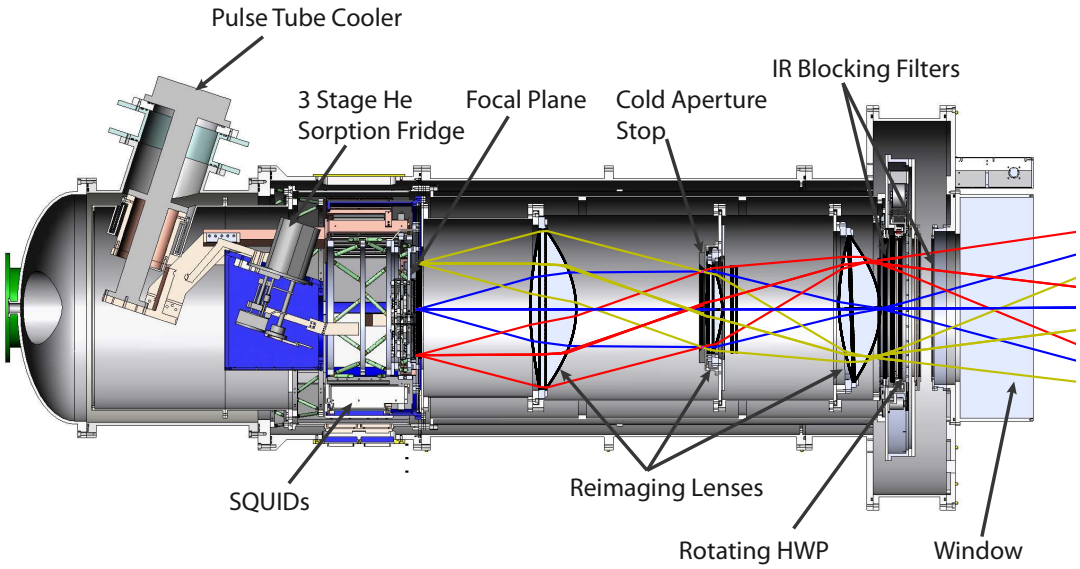

Figure 2.4: A cross-section drawing of the POLARBEAR cryogenic receiver. Figure from [50].

The cryostat, also referred to as the receiver, presented significant cryogenic engineering challenges related to its physical size, required to contain a 19 cm focal plane and re-imaging optics, and to its use of a single pulse tube cooler (PTC) as the only means of removing thermal energy from the cryostat. The re-imaging optics are needed to couple the reflective Gregorian-Dragone optics to the focal plane. The lenses for these optics are made of anti-reflection coated ultra-high-molecular-weight polyethylene.

The cryostat also contains a rotating HWP. The HWP is made of anti-reflection coated single crystal sapphire, which is birefringent, and at a thickness of 3.1 mm acts as a HWP for 150 GHz radiation. A bearing modified for cryogenic operation allows it to rotate in steps of 11.25 degrees, which allows the incoming polarization from the sky to be rotated to different angles before it reaches the

focal plane. This polarization angle rotation helps to average over systematic errors. The HWP is repositioned no more than once per day during observations.

The PTC is a commercial PT415 model built by Cryomech, Inc. It provides two-stage cooling and can reach temperatures lower than 4K on its coldest stage. The sub-Kelvin cooling is provided by a closed cycle three stage Helium sorption refrigerator build by Chase Research. It is the coldest stage of this refrigerator that cools the focal plane to below 0.25 K.

2.4 The POLARBEAR Focal Plane

The POLARBEAR focal plane is comprised of 1,274 transition edge sensor (TES) bolometers across seven wafers fabricated at the UC Berkeley Marvell Nanolab. While the use of TES bolometers has become standard in CMB experiments, POLARBEAR employs a unique focal plane architecture for coupling incoming radiation to the TESs. This coupling is achieved via a combination of contacting hemispherical dielectric lenslets and slot-dipole antennas. The contacting lenslets match the antenna response to the telescope optics and magnify the effective size of the antennas [54]. An image of the full focal plane array is presented in figure 2.5.

Each lenselt acts as a beam forming element for two slot-dipole antennas located underneath, oriented to be sensitive to orthogonal polarizations of the incoming radiation. Each antenna is coupled to a TES via microstrip waveguides. We refer to the pair of bolometers sharing the same lenslet as forming a focal-plane "pixel," and to the individual bolometers sensitive to orthogonal polarizations within that pixel as being either a "top" or "bottom" bolometer because of details of the fabrication process.

2.5 TES Bolometers

The purpose of POLARBEAR's bolometers is to linearly convert optical power received from the sky into a current which can be amplified and transmitted

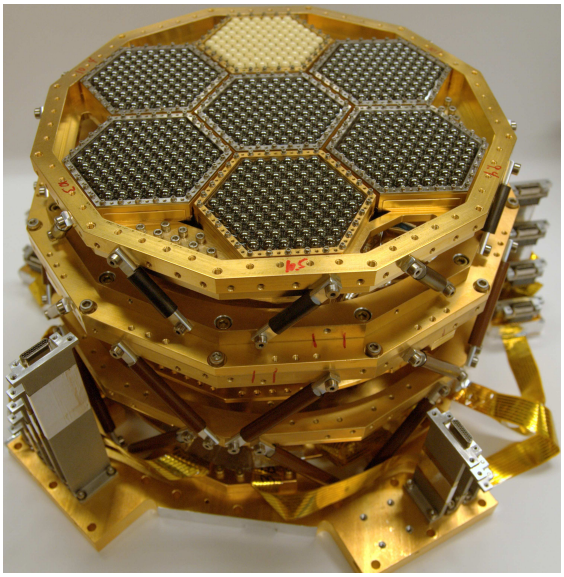

Figure 2.5: The POLARBEAR cryogenic focal plane insert. The seven detector wafer modules with anti-reflection coated dielectric lenslets are visible at the top of the image. The gray-colored lenslets on six of the wafer modules are made of silicon; the white dielectric lenslets on one wafer module are made of alumina. Figure from [54].

to room temperature electronics for storage and processing. A bolometer consists of a thermistor connected via a weak thermal link to a heat bath. The thermistor absorbs incoming optical power $P_{\rm opt}$ and electrical bias power $P_{\rm elec}$, the sum of which constitutes its operating power $P_{\rm tot}$. A cartoon illustration of this is shown in figure 2.6. A TES bolometer is designed so that it operates with the thermistor in the transition between being a normal and superconducting material. With a constant voltage bias, the large value of dR/dT in this superconducting transition creates a passive negative feedback mechanism which linearizes the bolometers response to changes in incoming optical power such that:

$$P_{\rm opt} + P_{\rm elec} = P_{\rm tot} \approx \text{constant} \tag{2.1}$$

so that a measurement of the current fluctuations through the bolometer $\Delta I_{\rm bolo}$ driven by the constant voltage bias constitutes a measurement of the fluctuations in optical power $\Delta P_{\rm opt}$ incident on the bolometer.

The desired operating power of the bolometer is fixed by the expected op-

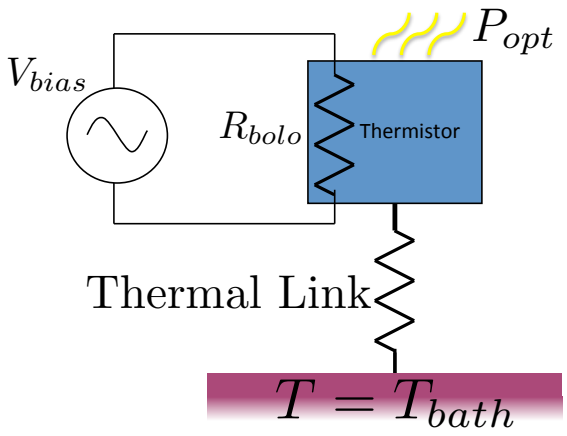

Figure 2.6: Cartoon diagram of a bolometer. The electrical power from the constant voltage bias and the optical power combine to give the total operating power. The thermal bath is provided by the silicon wafer cooled by the helium sorption fridge. The thermistor is connected to the rest of the wafer via a weak thermal link.

tical power coming from the sky, and the bath temperature is fixed by the helium sorption fridge to be about 0.25 K. The strength of the weak thermal link (between the thermistor and the bath temperature) as well as the transition temperature of the thermistor must be tuned so that the bolometer can operate given these parameters. As an additional constraint, the noise of the bolometer must be minimized. In general, the important noise sources for the bolometer are the photon noise discussed above, the phonon noise associated with the thermal carriers in the bolometer, and the readout noise associated with amplifiers and other electronics in the readout chain. The thermal carrier noise intrinsic to the bolometer can be minimized by choosing the correct ratio between the transition temperature and the bath temperature. With a bath temperature of 0.25 K this ratio must be carefully tuned in order for the bolometers to achieve photon noise limited performance as desired. Lower bath temperatures proposed for future experiments would make this optimization less important relative to the photon noise term.

2.6 Spectral Response

POLARBEAR observes the CMB through an atmospheric transmission window centered at 150 GHz. This window includes the peak emission of the CMB blackbody spectrum. It is bounded at the low end by an oxygen emission line and at the high end by a water emission line. Microstrip filters are fabricated on the bolometer wafers which allow only radiation in the desired band to deposit power on the bolometer. The center and width of the passband of these filters must be optimized to allow the instrument to observe with maximum efficiency. Too narrow a bandwidth means that the detectors collect fewer photons and must observe for a longer time to achieve an equivalent signal-to-noise ratio. A passband that is too wide or mis-centered will observe through the oxygen or water emission lines. Within these emission lines, the CMB photons will be absorbed by the atmosphere and the power from water or oxygen emission will be seen by the bolometer, resulting in significantly increased noise.

Achieving the proper passband was one of the most challenging aspects of fabricating the detector wafers. Each wafer was tested with a Fourier transform spectrometer (FTS) to ensure proper band placement before being deployed on the instrument. An example of such a measurement is shown in figure 2.7.

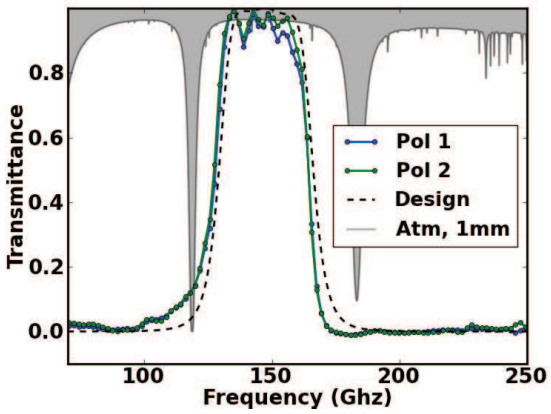

Figure 2.7: An FTS measurement of a focal plane pixel spectra, along with atmospheric absorption spectrum. The spectral bandpasses of the two bolometers with orthogonal polarizations within the pixel are shown as "Pol 1" and "Pol 2." The atmospheric spectrum shown is based on 1 mm of perceptible water vapor from the James Ax Observatory. Figure from [54].

2.7 From Power to Temperature

When POLARBEAR scans a particular part of the sky, it makes a measurement of the fluctuations in power coming from the sky over the integrated passband of the instrument, including the band-defining filters on the bolometer wafers. We are interested in measuring temperature fluctuations on the sky. We rely on our knowledge of the CMB having a blackbody spectrum to convert between units of power and temperature. For convenience we will define conversion to temperature units for two different emission spectra, K_{RJ} which will assume an emission spectra in the Rayleigh-Jeans limit, and K_{CMB} which will assume an emission spectra matching the CMB blackbody spectrum.

To proceed, we develop an expression for the power seen from the sky by each bolometer. For a thermal blackbody source at a temperature T, the Boltzmann occupation number is:

$$n_{\rm occ} = [\exp(\beta) - 1]^{-1} \tag{2.2}$$

with:

$$\beta = h\nu/k_B T \tag{2.3}$$

The occupation number $n_{\rm occ}$ is interpreted as the average volume density of photons per spatial mode as a function of frequency ν. Because the antennas we use are single-moded and each photon has energy $h\nu$, we may write the power received from the CMB by a bolometer as:

$$P_{\rm opt} = \int_0^\infty \eta(\nu) P(\nu) d\nu = \int_0^\infty \eta(\nu) h\nu n_{\rm occ} d\nu \tag{2.4}$$

where $\eta(\nu)$ indicates the fraction of photons from the source that are detected at the bolometer at a frequency ν. We approximate this integrand as constant over the narrow bandwidth $\Delta\nu$ defined as $\int_0^\infty \eta(\nu) d\nu$, with central frequency ν_c formed by the band defining filters as:

$$P_{opt} \approx \eta h \nu_c n_{{\rm occ},c} \Delta\nu \tag{2.5}$$

We now define the Rayleigh-Jeans temperature as:

$$T_{\mathrm{RJ}} \equiv T n_{\mathrm{occ},c} \beta_c \tag{2.6}$$

and see that $T_{\mathrm{RJ}} \rightarrow T$ as $\nu \rightarrow 0$. We will find it convenient to calibrate the instrument in terms of $\mathrm{K_{RJ}}$, but we will then want to convert between $\mathrm{K_{RJ}}$ and $\mathrm{K_{CMB}}$. The convenience of working in $\mathrm{K_{RJ}}$ units is driven by the fact that:

$$P_{\mathrm{opt}} = \eta \Delta\nu k_B T_{\mathrm{RJ}}, \tag{2.7}$$

and

$$\frac{\partial P_{\mathrm{opt}}}{\partial T_{\mathrm{RJ}}} = \text{constant}. \tag{2.8}$$

However, for our final analysis we will want to know the temperature in units of $\mathrm{K_{CMB}}$. First noting that:

$$\frac{dT_{\mathrm{RJ}}}{dT} = \frac{d}{dT} T n_{\mathrm{occ},c} \beta_c = n^2_{\mathrm{occ},c} \beta_c^2 e^{\beta_c}, \tag{2.9}$$

we may write:

$$\frac{\partial P_{\mathrm{opt}}}{\partial T} = \frac{\partial P_{\mathrm{opt}}}{\partial T_{\mathrm{RJ}}} \frac{dT_{\mathrm{RJ}}}{dT} = \frac{\partial P_{\mathrm{opt}}}{\partial T_{\mathrm{RJ}}} n^2_{\mathrm{occ},c} \beta_c^2 e^{\beta_c}. \tag{2.10}$$

Bearing in mind that the measured fluctuations in current through the bolometer are proportional to the fluctuations in optical power, we may also write:

$$\frac{\partial I_{\mathrm{bolo}}}{\partial T} = \frac{\partial I_{\mathrm{bolo}}}{\partial T_{\mathrm{RJ}}} n^2_{\mathrm{occ},c} \beta_c^2 e^{\beta_c}. \tag{2.11}$$

If we want to convert fluctuations in $\mathrm{K_{RJ}}$ to $\mathrm{K_{CMB}}$, we can evaluate expression 2.11 at $T = T_{\mathrm{CMB}}$. For $\nu_c = 150$ GHz and T=2.725 K, $n^2_{\mathrm{occ},c} \beta_c^2 e^{\beta_c} = 0.576$ so that:

$$\frac{\partial I_{\mathrm{bolo}}}{\partial T_{\mathrm{CMB}}} = 0.576 \frac{\partial I_{\mathrm{bolo}}}{\partial T_{\mathrm{RJ}}}. \tag{2.12}$$

In practice when we need this number we perform the integral in equation 2.4 using the measured detector bands, which vary between different wafers, making no approximation of the narrowness of the band.

2.8 Multiplexing & Data Acquisition

The 1,274 bolometers on the focal plane must all be simultaneously biased into the superconducting transition. To optimize the point in the transition to which each detector is biased, all detectors receive a slightly different level of voltage bias. The current through each bolometer must also be read out individually. The generation of voltage biases and digitization of the current signals is performed by room temperature electronics, which presents a challenge. Having individual wires running from room temperature to each bolometer for biasing and readout would lead to significant complexity inside the already constrained cryogenic space. It would also create unacceptable thermal loading on the cryogenic stages with each wire exiting the cryostat serving as a conduction path for heat to enter the cryostat. For this reason POLARBEAR uses a multiplexing scheme whereby eight bolometers can be individually voltage biased by a single pair of wires and read out by one other pair of wires. This is achieved by placing each bolometer in series with an LC filter tuned to different resonances. Eight different AC voltage biases are generated at different carrier frequencies (a "comb" of frequencies) tuned to the resonances of the individual filters, so that each bolometer sees only one voltage bias. Fluctuations in current from an individual bolometer are encoded into the sidebands of its carrier frequency via amplitude modulation, and the summed current from eight bolometers is amplified and exits the cryostat on one pair of wires. This technique is known as frequency domain multiplexing; it is analogous to AM radio.

The multiplexed bolometer data leaves the cryostat on 168 pairs of analog wires and are digitized by a set of 42 room temperature readout boards located on the telescope. These boards are referred to as Digital Frequency-Domain Multiplexing (DfMux) boards, and are designed by POLARBEAR collaborators at McGill University in Montreal [55] specifically for multiplexing arrays of TES bolometers. The data from each comb of frequencies is digitized at 25 MHz, demodulated into the individual bolometer time ordered data (TOD), and then each TOD is downsampled to 190.7 Hz. This data is then multicast over ethernet using the user datagram protocol (UDP) protocol and received by the data acquisition computer

located inside the control room. Each of the 42 boards appends its own timestamps to the bolometer data it transmits. These timestamps are based on the inter-range instrumentation group time codes "B" (IRIG-B) specification; the IRIG-B time signal is generated by a Global Positioning System receiver located at the observatory site and distributed to the DfMux boards. A synchronization pulse is used to ensure that the sample intervals of the DfMux boards are aligned to within 70 microseconds, though typically the alignment is much better. In practice this means that the individual time stamps are not needed and all bolometer data can be regarded as having been sampled in a time-synchronized way.

The DfMux boards generate the RPS signal that is used to synchronize other aspects of the experiment. This RPS signal is distributed to the telescope servo control system, which uses it to sample the encoders on the azimuth and elevation axes of the telescope synchronous with every other bolometer sample at a rate of 95.4 Hz. These data are returned to the control computer and archived along with the bolometer data.

All archived data are transmitted down the mountain by a high-bandwidth microwave link to a low-site control center in the town of San Pedro de Atacama, Chile. From there the Internet bandwidth is sufficient to send the data to the United States.

Figure 2.2 is a reprint of material as it appears in A Measurement of the Cosmic Microwave Background B-Mode Polarization Power Spectrum at Sub-Degree Scales with POLARBEAR. The POLARBEAR Collaboration: P. A. R. Ade, Y. Akiba, A. E. Anthony, K. Arnold, M. Atlas, D. Barron, D. Boettger, J. Borrill, S. Chapman, Y. Chinone, M. Dobbs, T. Elleflot, J. Errard, G. Fabbian, C. Feng, D. Flanigan, A. Gilbert, W. Grainger, N. W. Halverson, M. Hasegawa, K. Hattori, M. Hazumi, W. L. Holzapfel, Y. Hori, J. Howard, P. Hyland, Y. Inoue, G. C. Jaehnig, A. H. Jaffe, B. Keating, Z. Kermish, R. Keskitalo, T. Kisner, M. Le Jeune, A. T. Lee, E. M. Leitch, E. Linder, M. Lungu, F. Matsuda, T. Matsumura, X. Meng, N. J. Miller, H. Morii, S. Moyerman, M. J. Myers, M. Navaroli, H. Nishino, H. Paar, J. Peloton, D. Poletti, E. Quealy, G. Rebeiz, C. L. Reichardt, P. L. Richards, C. Ross, I. Schanning, D. E. Schenck, B. D. Sherwin, A. Shimizu, C. Shimmin,

M. Shimon, P. Siritanasak, G. Smecher, H. Spieler, N. Stebor, B. Steinbach, R. Stompor, A. Suzuki, S. Takakura, T. Tomaru, B. Wilson, A. Yadav, and O. Zahn, ArXiv e-prints, Mar. 2014. The dissertation author made essential contributions to many aspects of this work.

Figure 2.1 and figure 2.4 are reprints of material as it appears in The POLARBEAR experiment. Z. D. Kermish, P. Ade, A. Anthony, K. Arnold, D. Barron, D. Boettger, J. Borrill, S. Chapman, Y. Chinone, M. A. Dobbs, J. Errard, G. Fabbian, D. Flanigan, G. Fuller, A. Ghribi, W. Grainger, N. Halverson, M. Hasegawa, K. Hattori, M. Hazumi, W. L. Holzapfel, J. Howard, P. Hyland, A. Jaffe, B. Keating, T. Kisner, A. T. Lee, M. Le Jeune, E. Linder, M. Lungu, F. Matsuda, T. Matsumura, X. Meng, N. J. Miller, H. Morii, S. Moyerman, M. J. Myers, H. Nishino, H. Paar, E. Quealy, C. L. Reichardt, P. L. Richards, C. Ross, A. Shimizu, M. Shimon, C. Shimmin, M. Sholl, P. Siritanasak, H. Spieler, N. Stebor, B. Steinbach, R. Stompor, A. Suzuki, T. Tomaru, C. Tucker, and O. Zahn, Society of Photo-Optical Instrumentation Engineers (SPIE) Conference Series, vol. 8452 of Society of Photo-Optical Instrumentation Engineers (SPIE) Conference Series, Sept. 2012. The dissertation author made essential contributions to many aspects of this work.

Figure 2.5 and figure 2.7 are reprints of material as it appears in The bolometric focal plane array of the POLARBEAR CMB experiment. K. Arnold, P. A. R. Ade, A. E. Anthony, D. Barron, D. Boettger, J. Borrill, S. Chapman, Y. Chinone, M. A. Dobbs, J. Errard, G. Fabbian, D. Flanigan, G. Fuller, A. Ghribi, W. Grainger, N. Halverson, M. Hasegawa, K. Hattori, M. Hazumi, W. L. Holzapfel, J. Howard, P. Hyland, A. Jaffe, B. Keating, Z. Kermish, T. Kisner, M. Le Jeune, A. T. Lee, E. Linder, M. Lungu, F. Matsuda, T. Matsumura, N. J. Miller, X. Meng, H. Morii, S. Moyerman, M. J. Myers, H. Nishino, H. Paar, E. Quealy, C. Reichardt, P. L. Richards, C. Ross, A. Shimizu, C. Shimmin, M. Shimon, M. Sholl, P. Siritanasak, H. Spieler, N. Stebor, B. Steinbach, R. Stompor, A. Suzuki, T. Tomaru, C. Tucker, and O. Zahn, Society of Photo-Optical Instrumentation Engineers (SPIE) Conference Series, vol. 8452 of Society of Photo-Optical Instrumentation Engineers (SPIE) Conference Series, Sept. 2012. The dissertation

author made essential contributions to many aspects of this work.

Chapter 3

Instrument Calibration

In order to use the acquired data to reconstruct the signals coming from the sky, several calibration steps are required. There are four properties of the instrument that we need to know: The responsivity of each bolometer to fluctuations in temperature on the sky, the polarization orientation angle of each detector as a function of time, where on the sky each bolometer is pointing as a function of time, and finally the shape of the effective instrument beam. We will describe the calibration of each of these below.

3.1 Gain Calibration

The time ordered data (TOD) from each of the bolometers are recorded in uncalibrated units proportional to the current fluctuations through the TES. We refer to these units as "analog to digital converter counts" (ADC counts). In order to create maps of the CMB in temperature units we need to establish a calibration procedure for converting the ADC counts into Kelvins. In the CMB field this calibration of detector responsivities is commonly referred to as "gain calibration" and the multiplicative ratio between ADC counts and temperature is referred to as "gain." When working in the Rayleigh-Jeans limit, we will define the gain $g_{\frac{\mathrm{ADC}}{\mathrm{T_{RJ}}}}$ as:

$$g_{\frac{\mathrm{ADC}}{\mathrm{T_{RJ}}}} \equiv -\frac{\partial I_{\mathrm{bolo}}}{\partial T_{\mathrm{RJ}}} \tag{3.1}$$

with I_{bolo} expressed in units of ADC counts. We have absorbed the inverse relationship between current and optical power into the definition so that gains are positive quantities. This allows us to write:

$$d^i(t)[K_{\mathrm{RJ}}] = \frac{d^i(t)[\mathrm{ADC\,Counts}]}{g^i_{\frac{\mathrm{ADC}}{\mathrm{T_{RJ}}}}(t)} \tag{3.2}$$

where $d^i(t)$ indicates a TOD for a particular bolometer indexed by i, $[K_{\mathrm{RJ}}]$ or [ADC Counts] indicate the units the TOD is expressed in, and $g^i_{\frac{\mathrm{ADC}}{\mathrm{T_{RJ}}}}(t)$ indicates the gain for the bolometer i as a function of time. It will also occasionally be convenient to write $g_{\frac{\mathrm{T_{RJ}}}{\mathrm{ADC}}}$, which is simply the reciprocal of $g_{\frac{\mathrm{ADC}}{\mathrm{T_{RJ}}}}$. We will also use $g_{\frac{\mathrm{ADC}}{\mathrm{T_{CMB}}}}$ or $g_{\frac{\mathrm{T_{CMB}}}{\mathrm{ADC}}}$ when gain calibrating to CMB temperature units. Conversion between $g_{\frac{\mathrm{ADC}}{\mathrm{T_{RJ}}}}$ and $g_{\frac{\mathrm{ADC}}{\mathrm{T_{CMB}}}}$ is explained in section 2.7.

The POLARBEAR experiment uses several different astrophysical and ground-based calibration sources to establish this gain factor. These can be divided into relative and absolute calibrators. The best fit WMAP-9 C_ℓ^{TT} power spectrum [29] is used to perform absolute calibration; all other sources of calibration are relative. See section 4.7 for a discussion of the absolute gain calibration.

There are two types of relative gain calibration that must be accounted for: time-relative calibration, which tracks how gain factors change over time, and focal-plane relative calibration, which tracks how gains need to be scaled in order to co-add different detectors across the focal plane. A particularly important aspect of focal-plane relative gains is measuring the relative gains of the two detectors in a pixel pair. Because the TOD from the two bolometers in a pixel pair are directly differenced to form a polarization TOD, mis-calibrating the two bolometer gains relative to each other leads directly to a false polarization signal proportional to the temperature field. This is an important systematic, the constraints on which are discussed further in section 5.1.

Planets serve as good celestial sources for focal plane relative gain calibration measurements. The procedure for measuring gains from planets is described in 3.1.1. If gains were time-stable, we could perform a single high signal-to-noise

planet scan and used this for gain calibration. However, the gains vary with atmospheric opacity, the elevation at which the telescope is observing, the temperature of the bolometer wafers, and the tuning point of the bolometer. Because these variables can change rapidly, it is desirable to measure the calibration factor frequently for each bolometer. Observations of celestial sources like planets are time consuming and there are not always appropriate sources available for observation, so celestial sources do not make good time-relative calibrators.

The thermal calibration source described in section 2.2.2 provides an excellent time-relative calibrator. Gain calibration using this source is described in section 3.1.2. It provides a calibration for all detectors across the focal plane in a three minute observation and is always available because it does not rise and set as celestial sources do. However, its intensity varies across the focal plane, so the thermal source alone cannot function as a focal plane relative calibrator. A "bootstrapping" procedure is thus necessary whereby planets are used to calibrate the thermal calibration source, and then this local source is used more frequently to calibrate the bolometer responses. See section 3.1.3 for the details of this procedure.

Another good source of focal plane relative calibration is the use of elevation nods. This involves slewing the telescope up and down in elevation by a few degrees. The changes in atmospheric column density as a function of elevation create a signal for the bolometers. This is a particularly good calibrator for the two bolometers in a pixel pair because they are looking through the same column of atmosphere during the elevation nod. Elevation nods are less useful as time-relative calibrators because comparing data from two different times requires precise knowledge of the variation in atmospheric conditions between the measurements. We use elevation nods only as a consistency check for the thermal calibration source derived values.

3.1.1 Planet Gain Measurements

POLARBEAR uses gain calibration measurements from Venus, Jupiter and Saturn. These planets are bright enough to allow relatively brief observations to achieve sufficient signal-to-noise; typically POLARBEAR observes a source for 40

minutes in order to generate a calibration for all detectors. Their small angular diameter (typically $\sim$ 30 arcseconds) means they can be approximated as point sources, which simplifies the calibration procedure. What we seek is a way to use a planet measurement to determine the quantity $g_{\frac{\mathrm{ADC}}{\mathrm{T_{RJ}}}}$. For a point source this quantity will vary given the source's position within the detector beam. In fact what we want is the value of $g_{\frac{\mathrm{ADC}}{\mathrm{T_{RJ}}}}$ for a source filling the entire detector beam. Expressing the beam response function as $B(\theta, \phi)$, we let:

$$g_{\frac{\mathrm{ADC}}{\mathrm{T_{RJ}}}} = \int d\theta d\phi B(\theta, \phi) \tag{3.3}$$

where this equality defines the normalization for $B(\theta, \phi)$ to be in units of $\frac{ADC}{K_{RJ} \cdot \mathrm{steradian}}$. When we scan over a planet with an individual bolometer, we create a map from the TOD that is a convolution of the beam function with the source:

$$m(\theta, \phi) = \int d\theta' d\phi' T(\theta', \phi') B(\theta - \theta', \phi - \phi') \tag{3.4}$$

where $T(\theta, \phi)$ represents the spatial distribution of source temperature. Treating the planet as a point source, we let:

$$T(\theta, \phi) \rightarrow \delta(\theta)\delta(\phi) T_P \Omega_P \tag{3.5}$$

where the δs are Dirac delta functions, T_P represents the temperature of the planet and Ω_P represents the actual solid angle of the planet. The factors T_P and Ω_P ensure that the total signal in the map is correct. Planet temperatures are taken from millimeter-wave measurements published in [56]. There is limited data available for this purpose, and we do not attempt to model seasonal variations in temperature or variation in apparent temperature with, i.e., the change in angle of Saturn's rings as viewed from Earth. The possible impacts of this are discussed in section 3.1.4. The solid angle of the planet sources come from an ephemeris calculation using the exact observation time.

With the substitution from equation 3.5 we get:

$$B(\theta, \phi) = \frac{m(\theta, \phi)}{T_P \Omega_P} \tag{3.6}$$

which is equivalent to saying that the map is a map of the detector beam. We can then write:

$$g_{\frac{\mathrm{ADC}}{\mathrm{T_{RJ}}}} = \int d\theta d\phi \frac{m(\theta,\phi)}{T_P \Omega_P}. \tag{3.7}$$

Essentially, we have used the technique of scanning over a point source to allow the source to function as a beam-filling load that can be used to calibrate the detector gain.

When POLARBEAR observes a planet, it tracks the planet as it moves across the sky and relative to that tracking performs azimuth scans that are wide enough to sweep the entire focal plane across the planet. It also takes elevation steps between each azimuth scan and in this way allows every detector to scan the planet. The elevation steps used during this process are 2 arcminutes in size, which is not a high enough resolution to capture all of the important features of the detector beam. The map shown in figure 3.1 clearly shows the lack of scan coverage.

It is thus insufficient to simply integrate the map obtained from the planet scan. The technique we employ instead is to use the planet data to fit an elliptical Gaussian model to the beam data. The model used is:

$$m(x,y) = A_P \ \exp\left(-\left(\frac{x^2}{2\sigma_x^2} + \frac{y^2}{2\sigma_y^2}\right)\right) \tag{3.8}$$

where A_P, σ_x, and σ_y are the parameters being fit for and x and y are the flat-space projection[1] equivalents of θ and ϕ. A_P determines the amplitude of the source and σ_x, and σ_y determine the ellipticity of the beam. We also record the paramater errors σ_{A_P}, σ_{σ_x}, and σ_{σ_x}. There are additional coordinate-transform terms in the model that fit for the center of the planet and allow its major- and minor- axes to be rotated with respect to the x- and y- axes of the scan which are not shown here. This expression is then used as a representation for the beam, and its integral can be performed analytically:

$$g^{analytic}_{\frac{\mathrm{ADC}}{\mathrm{T_{RJ}}}} = \frac{2\pi A_P \sigma_x \sigma_y}{T_P \Omega_P}. \tag{3.9}$$

[1]The projection employed is the equal-area Sanson-Flamsteed projection.

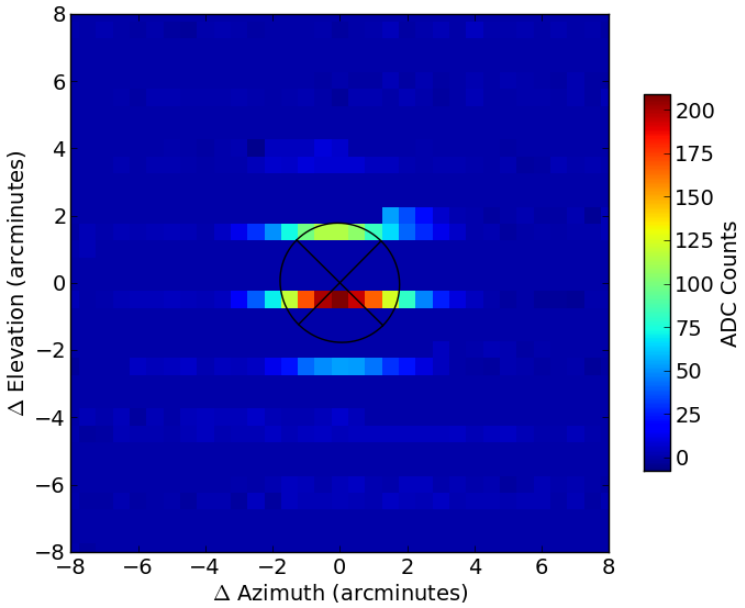

Figure 3.1: A beam map produced by scanning Saturn is shown for one bolometer. The map is produced with a pixel size of 30 arcseconds, making the 2 arcminute step size of the scan readily apparent. The best-fit elliptical Gaussian is shown in black at the FWHM contour, along with the orientation of the major- and minor-axes.

We refer to calibrations calculated in this way as being "analytic" planet calibrations. If the analytic elliptical Gaussian model were a perfect representation of the beam, this would be ideal. However, in addition to the main beam lobe which is approximately 3.5 arcminutes at full-width half-maximum (FWHM), there is additional sidelobe structure at a lower level further from the main beam which varies from detector to detector. In an attempt to compensate for this, the integration procedure is modified further. First, the integral of the main lobe is performed on the analytic model. The analytic model is then subtracted from a low resolution map (see figure 3.2a and 3.2b) to produce a map of residual structure. This residual structure map is then integrated over the region 4 to 8 arcminutes from the source center and added to the initial analytic integral. Gains calculated with this technique are referred to as "combined" gains because of the combination of analytic and numerical integrals. This technique is not ideal and still suffers from

the problems associated with low resolution mapping of the sidelobe structure.

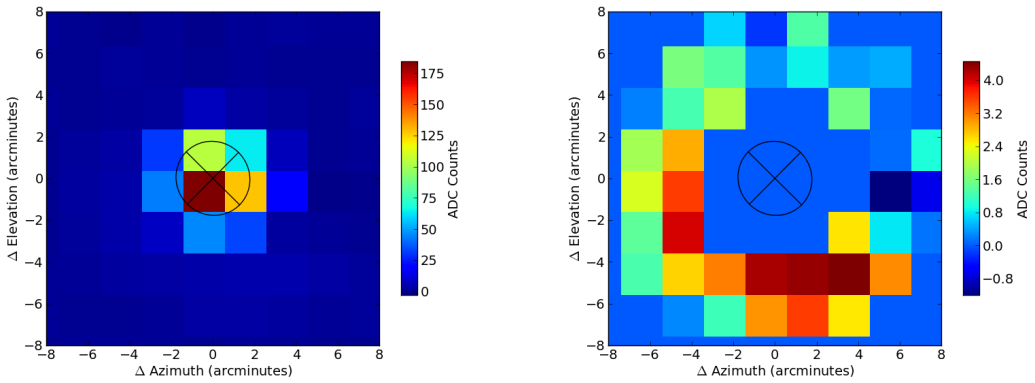

(a) A lower resolution map of the same scan shown in figure 3.1. Using a pixel resolution of 2 arcminutes conceals the coarseness of the scan and is used for performing numerical integration of the map.

(b) The same map as shown in figure 3.2a, but with a mask applied that sets pixels within a 4 arcminute radius or beyond an 8 arcminute radius to zero to demonstrate the limits of integration. Only this region of the map is included in the numerical integration procedure described in the text. Note also the change in color scale used in this image.

Figure 3.2: Beam maps used in gain calibration

An additional technique used in an attempt to overcome this problem is to employ a beam template to fit for gains from planets. This technique involves constructing a high-resolution template map for a beam that contains information about its main lobe and extended sidelobe structure. This template map is scaled in overall amplitude via a fitting procedure to match the low resolution data obtained during one planet scan, which is equivalent to scanning over part of the template. A numerical integral is then performed over the scaled template map to obtain $g_{\frac{\mathrm{ADC}}{\mathrm{T_{RJ}}}}$ as in equation 3.7. This method accounts for beam structure in a way that is not dependent on analytic approximations or integration of low-resolution maps.

An example beam template map is shown in figure 3.3. Instead of being constructed from an individual detector beam, this template is a sum of all active detectors on one detector wafer. POLARBEAR's scan strategy for these calibration scans does not include enough day-to-day variation to allow for individual detector

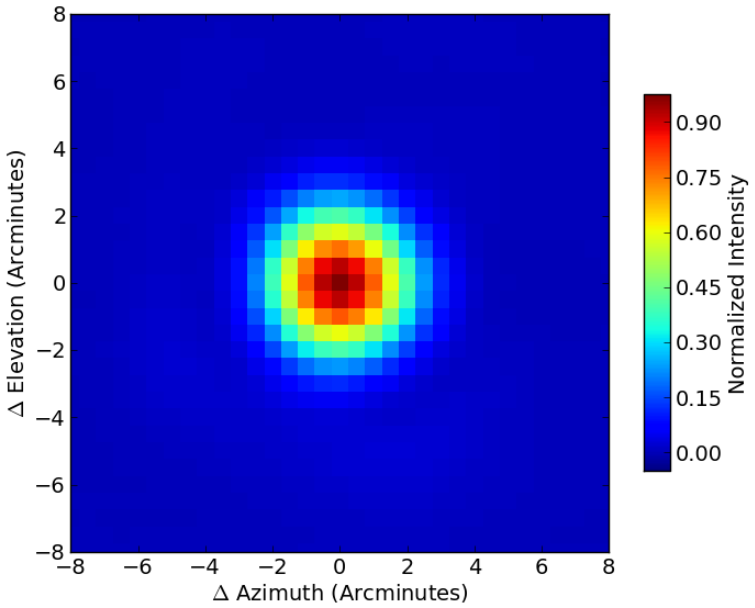

Figure 3.3: A high-resolution beam template constructed from coadding planet maps from all detectors in wafer 10.1. In addition to the main beam, sidelobe structure is subtly visible at around 6 arcminutes in radius.

templates to be constructed, and so the alternative is to build a template based on an entire wafer of detectors. Unfortunately, this template does not give consistent results and so only the "analytic" and "combined" gain techniques are used for actual calibrations. Future changes to the scan strategy will include daily offsets to allow for the creation of individual detector templates, which should improve the quality of future gain calibrations.

3.1.2 Thermal Calibration Source Measurements

The second component of the gain calibration procedure is the thermal calibration source described in section 2.2.2. The typical calibration procedure with this source is to spin the chopper located between the heater and the light pipe in order to produce a square wave signal in the detectors. This is done at a series of six different frequencies between four and fourty-four Hertz for thirty seconds each. The reference signal of the chopper is recorded and used to recover

an amplitude for the square wave in each active detector at each frequency, A_f. These amplitudes are then used to fit each bolometer for an overall DC response amplitude A_{therm} in units of ADC counts as well as a single-pole low pass filter time constant τ. The model used is:

$$A_f = \frac{A_{therm}}{\sqrt{1 + (2\pi f \tau)^2}} \tag{3.10}$$

and is fit across the six frequencies at which the thermal source is chopped. A sample TOD from one bolometer during part a thermal source calibration is shown in figure 3.4, and the associated fit is shown in 3.5.

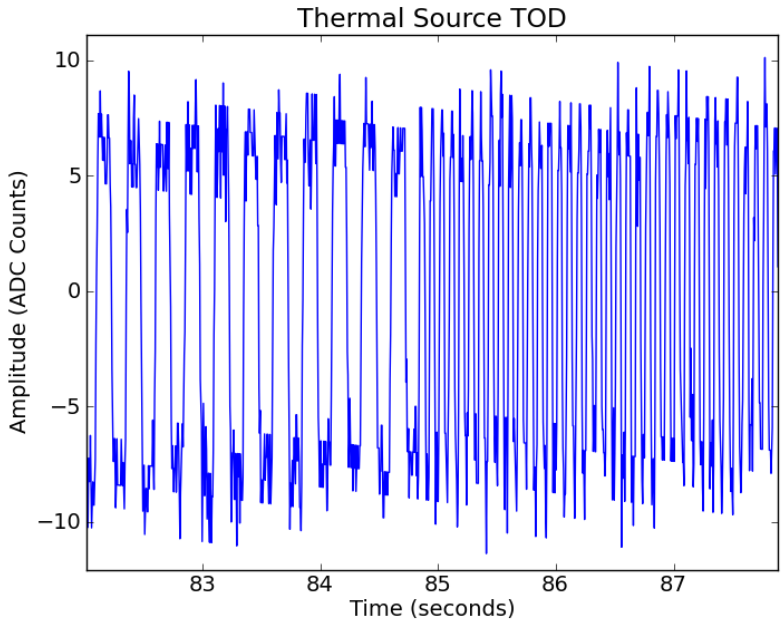

Figure 3.4: Time ordered data is shown from one bolometer over part of an observation of the thermal calibration source. The transition between the 4 Hz and 12 Hz chop frequencies is clearly visible.

3.1.3 Thermal Source Effective Temperature

As described above, neither the planet gain calibration nor the thermal source gain calibration are able to serve as both time and focal plane relative gain calibrators. It is thus necessary to combine these two sources of measurement to

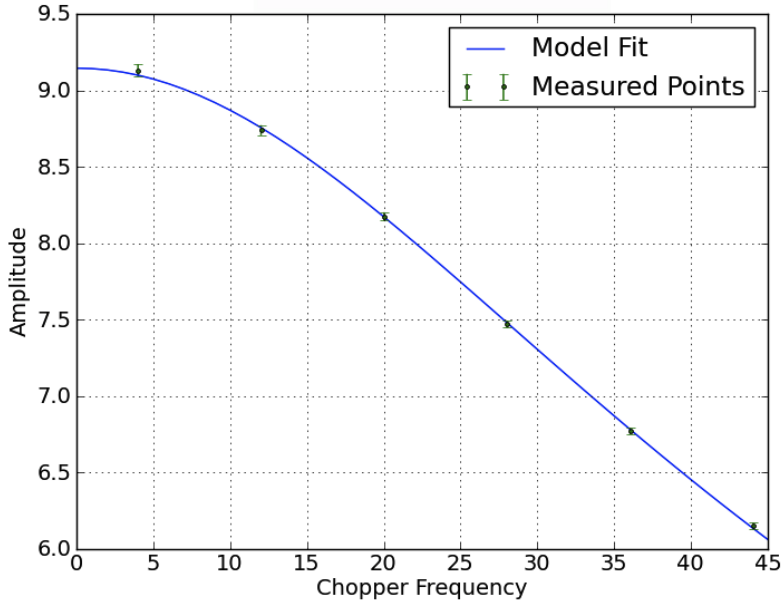

Figure 3.5: A fit to a full thermal source observation is shown for a single bolometer, along with the measured data points and error bars. This fit is to the same data which is partially displayed in figure 3.4 in the time domain. The parameters determined from the fit are: $A_{therm} = 9.1452$ ADC counts, $\tau = 4$ ms.

create a complete relative calibration source that will allow us to coadd data from different detectors across the focal plane and from scans taken a different times. To achieve this, a thermal calibration source measurement is taken immediately before and after each planet scan. For every bolometer on the focal plane, the planet scan can be used to form the quantity $g^{combined}_{\frac{\mathrm{ADC}}{\mathrm{T_{RJ}}}}$ or $g^{analytic}_{\frac{\mathrm{ADC}}{\mathrm{T_{RJ}}}}$ as described in section 3.1.1. The thermal source measurements also provide $A_{therm,pre}$ and $A_{therm,post}$ which are the amplitudes of the thermal source calibrations taken before and after the planet scan, respectively. We do not currently take account of when during a planet scan a particular bolometer is scanned over the planet, so we simply average these two terms:

$$A_{therm} = \frac{A_{therm,pre} + A_{therm,post}}{2} \tag{3.11}$$

and we model the error, including the term due to the gain drift that occurs during the planet scan, as:

$$\sigma_{A_{therm}} = \left| \frac{(A_{therm,pre} + \sigma_{A_{therm},pre}) - (A_{therm,post} - \sigma_{A_{therm},post})}{2} \right| \tag{3.12}$$

where $\sigma_{A_{therm},pre}$ and $\sigma_{A_{therm},post}$ are the errors on the thermal source gain fits before and after the planet scan. Interpolating the thermal source amplitude to the time at which a particular bolometer scans the planet will be explored as a potential improvement in the future.

With A_{therm} and $g_{\frac{\mathrm{ADC}}{\mathrm{T_{RJ}}}}$ we can form the effective thermal source temperature. Allowing individual bolometers to be indexed by i:

$$T^i = \frac{A^i_{therm}}{g^i_{\frac{ADC}{T_{RJ}}}} \tag{3.13}$$

with the error calculated as:

$$(\sigma^i_T)^2 = \left(\frac{\sigma^2_{A_{therm}}}{A^2_{therm}} + \frac{\sigma^2_{A_P}}{A^2_P} + \frac{\sigma^2_{\sigma_x}}{\sigma^2_x} + \frac{\sigma^2_{\sigma_y}}{\sigma^2_y} \right) (T^i)^2. \tag{3.14}$$

We now have an expression for the effective temperature of the thermal source.

Thermal Source Polarization & Effective Temperature Parameterization

We observe the thermal source to be subtly polarized in a way that varies across the focal plane. We believe this is related to the variation in angle at which light leaves the light-pipe to reach different sections of the focal plane, but have not constructed a detailed physical model. This polarization impacts the relative gain of two bolometers within a pixel, so it is important that it be well characterized. Because this polarization is rotated by the HWP, it creates a HWP dependent term in the gain model. While the polarization is rotated, the intensity of the source is unaffected, and this motivates studying the intensity and polarization separately. Re-parameterizing the expression for the thermal source effective temperature is thus desirable, and will in fact allow us to more easily compare different measurement techniques as well.

We allow for each pixel pair to see a polarized intensity $\tilde{Q}$ during a thermal source calibration. Letting j index the pixel number, t and b represent the top

and bottom bolometers within each pixel, and ϕ_P^j represent the angle between the pixel's polarization orientation and the orientation of the polarized intensity, we have:

$$\begin{aligned} T^{j,t} &= I^j + \tilde{Q}^j \cos(2\phi_P^j) \\ T^{j,b} &= I^j - \tilde{Q}^j \cos(2\phi_P^j) \end{aligned} \tag{3.15}$$

where we have also parameterized the sum of the two effective temperatures in a pixel with the intensity I:

$$I^j \equiv \frac{T^{j,t} + T^{j,b}}{2}. \tag{3.16}$$

We now define $P_{\rm frac}$ for each pixel pair:

$$P^j_{\rm frac} \equiv \frac{T^{j,t} - T^{j,b}}{T^{j,t} + T^{j,b}} = \frac{\tilde{Q}^j}{I^j} \cos(2\phi_P^j) \tag{3.17}$$

so that we may write:

$$\begin{aligned} T^{j,t} &= I^j(1 + P^j_{\rm frac}) \\ T^{j,b} &= I^j(1 - P^j_{\rm frac}). \end{aligned} \tag{3.18}$$

We now have a parameterization for the thermal source effective temperature with a single intensity and polarization parameter per pixel, and it is possible to measure I^j and $P^j_{\rm frac}$ separately. I^j will be independent of the HWP angle and $P^j_{\rm frac}$ will depend on the HWP angle. Note that the index j will be omitted to simplify the notation in some of what follows, but it is to be understood that I and $P_{\rm frac}$ have different values measured for each focal plane pixel.

In order to integrate the thermal source measurements into a pipeline for generating gains, we must have reliable measurements of the effective temperature of the thermal source as seen from each detector. We separate this task into measuring I and $P_{\rm frac}$ for each pixel. Our goal is to create templates for the focal plane I^j and $P^j_{\rm frac}$ that can be used to calibrate gains with any measurement of the thermal source. In the first approximation, the values of I affect the co-addition of different pixels across the focal plane, while values of $P_{\rm frac}$ affect the pixel-pair relative gain. In both cases we form the templates by combining measurements of many planet scans.

3.1.4 Thermal Source Intensity Template

The intensity measurements will be used to co-add data from detectors across the focal plane with varying sidelobe structure. Because these sidelobes affect the inferred gain, it is important that the variations in sidelobes be captured by the measurement. We thus use the *combined* planet gain measurements to create the intensity template. When we construct the polarization template below, we will only be comparing two bolometers in a pixel pair, and will use the *analytic* which is less noisy but doesn't capture differences in sidelobe structure. We form the individual bolometer effective temperature measurements as:

$$T^i = \frac{A^i_{therm}}{g^{combined}_{\frac{\mathrm{ADC}}{\mathrm{T_{RJ}}}}}. \tag{3.19}$$

Again, these individual bolometer measurements are summed to form I for each pixel as:

$$I \equiv \frac{T^t + T^b}{2}. \tag{3.20}$$

In order to co-add multiple planet measurements, we want to quantify the error on each one. We can combine equation 3.20 with equation 3.14 to write the error on I as:

$$\begin{aligned} \sigma_I^2 &= \left(\frac{\partial I}{\partial T^t}\right)^2 \sigma^2_{T^t} + \left(\frac{\partial I}{\partial T^b}\right)^2 \sigma^2_{T^b} + 2\mathrm{cov}(T^t, T^b)\frac{\partial I}{\partial T^t}\frac{\partial I}{\partial T^b} \\ &= \frac{\sigma^2_{T^t} + \sigma^2_{T^b}}{4}. \end{aligned} \tag{3.21}$$

We have no reason to think that the errors on the two temperature measurements should be correlated, so we set the covariance term to zero.

We compute I and σ_I for many planet measurements taken at different times over the season. Planet scans with fewer than 300 active channels are excluded to avoid problematic data. In order to be included in a measurement of I, both the top and bottom bolometers in a pixel must have successful gain fits from the planet and the thermal source. We average the measurements together, weighting each by $1/\sigma_I^2$, and requiring that each pixel have a minimum of three planet measurements to be given a value in the template.

Our standard intensity template is derived from 28 scans of Saturn taken in 2012. This template was settled on early in the analysis process, and deviations from it with newer data have been small. Figure 3.6 shows a plot of two times the value of the intensity template for all pixels across the focal plane.

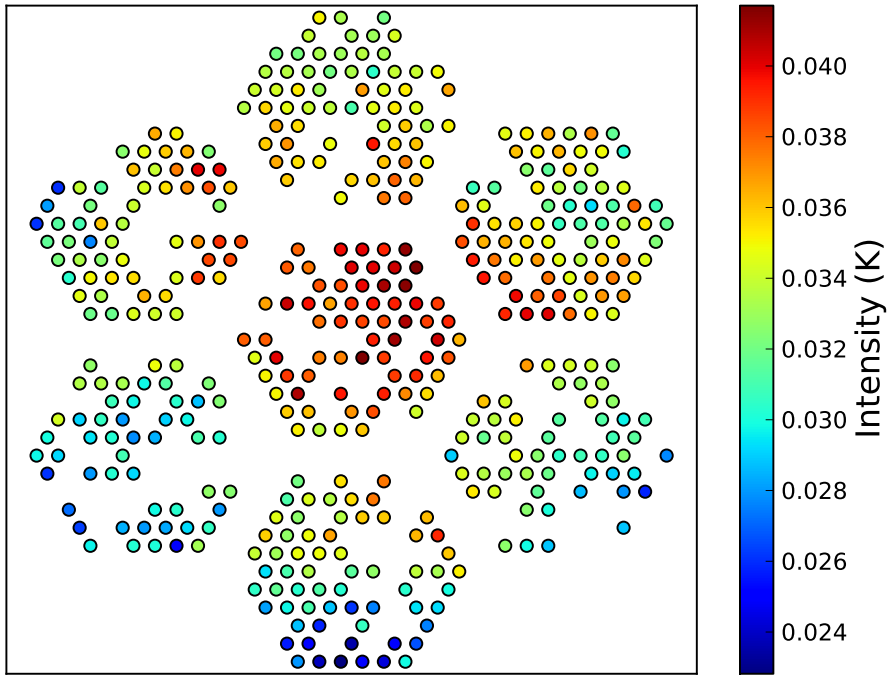

Figure 3.6: The intensity template for the chopped thermal source. Here we plot $2I$, which shows the actual value for the effective temperature of the source given our parameterization for I.

Celestial Source Temperature Drifts

Due to concern over un-modeled changes in celestial source temperatures, one important check of the intensity template is to allow individual planet scans to be scaled relative to each other. To do this, we take our initial template I^j that comes from the simple weighted co-addition of each measurement and fit for a scale factor to apply to each planet measurement. This is done as a χ^2 minimization

in the parameter S_T, which is the same for all j (where j again indexes the focal plane pixel):

$$\chi^2 = \sum_j \frac{(S_T I^j_{template} - I^j_{measurement})^2}{(\sigma^j_I)^2}. \tag{3.22}$$

We fit a different value of S_T for each planet measurement. With these independent scale factors, long term drifts in the planet temperature are no longer a concern for accurately measuring the relative detector gains across the focal plane. We again perform the weighted co-addition of the planet measurements, except scaling every pixel's intensity measurement and error by the factor of $1/S_T$ calculated for that planet scan to create a second template. If we call the template assembled from unscaled measurements I_{T1} and the template using scaled measurements I_{T2}, we find that $\langle |I^j_{T1} - I^j_{T2}| \rangle_j$ is less than 0.3% of the template values, which we consider to be negligible. We take this as evidence that our focal plane relative gain measurements are not adversely affected by long term temperature drifts in our celestial sources.

Thermal Source Temperature Drifts

The scaling procedure described above will correct for both long term drifts in a celestial source being measured, and for drifts in the thermal source temperature. However, while drifts in celestial source temperature are unimportant if they do not affect the template, changes in the thermal source temperature will affect the time-relative co-addition of data from different scans. Because the thermal source temperature is regulated, we do not expect to see long term drifts. To check this, we look for coherent time trends in the scale factors calculated above. Comparing shifts in scale factor between different celestial sources allows us to break the degeneracy between temperature drifts in our thermal source and temperature drifts in celestial sources. We see variations in scale factors at the few percent level, but with no long term trends that are are consistent between different celestial sources. Thus while we cannot rule out short term thermal source temperature fluctuations, we see no evidence for long term trends which would bias our gains across the full observation season.

3.1.5 Thermal Source Polarization Template

The thermal source polarization template $P^j_{\rm frac}$ must account for differences in the effective temperature of the thermal source between top and bottom bolometers in a pixel pair. We expect this term in the gain model to be more important in terms of its potential systematic error impact, and we also expect it to depend on the HWP angle.

Because the goal is to compare thermal source effective temperatures between two bolometers that are at the same point in the focal plane and looking through the same contacting lenslet, we expect sidelobe structure to be similar between the two. We thus choose to use the *analytic* planet gain. The *analytic* gain is in general a less noisy, though potentially more biased, measurement of the gain. Thus for the $P_{\rm frac}$ template we set:

$$T^i = \frac{A^i_{therm}}{\left(g^{analytic}_{\frac{\rm ADC}{\rm T_{RJ}}}\right)^i}. \tag{3.23}$$

Similarly, because we are comparing relative amplitudes between top and bottom bolometers in the same pixel, there is less concern about knowing the actual amplitude of the planet signal than with measurements of I. We thus combine measurements of Venus, Jupiter, and Saturn into the same data set as measurements of $P_{\rm frac}$.

In order to estimate the errors on individual planet measurements, we take our definition $P_{\rm frac} \equiv \frac{T^t - T^b}{T^t + T^b}$ and combine this with equation 3.14 to estimate the error on $P_{\rm frac}$ as:

$$\begin{aligned}
\sigma^2_{P_{\rm frac}} &= \left(\frac{\partial P_{\rm frac}}{\partial T^t}\right)^2 \sigma^2_{T^t} + \left(\frac{\partial P_{\rm frac}}{\partial T^b}\right)^2 \sigma^2_{T^b} + 2{\rm cov}(T^t, T^b)\frac{\partial P_{\rm frac}}{\partial T^t}\frac{\partial P_{\rm frac}}{\partial T^b} \\
&= 4\frac{(T^b)^2\sigma^2_{T^t} + (T^t)^2\sigma^2_{T^b} - 2{\rm cov}(T^t, T^b)T^tT^b}{(T^t + T^b)^4} \\
&= 4\frac{(T^b)^2\sigma^2_{T^t} + (T^t)^2\sigma^2_{T^b}}{(T^t + T^b)^4},
\end{aligned} \tag{3.24}$$

where we have again set the covariance between the two temperatures to zero in

the last step. We use this as a starting point for error estimation, but will allow for other sources of error that are unaccounted for in equation 3.24.

A further complication in building the polarization template is that the thermal source was dismounted for maintenance on three different occasions during the first observation season. While this maintenance does not seem to have affected the intensity of the source, it did change its polarization properties. We thus fit for four different $P_{\rm frac}$ templates over the four different thermal source "epochs." We use planet measurements from within each epoch to build our templates.

We expect our measurement of $P_{\rm frac}$ to depend upon both the HWP angle and the stimulator epoch we are in. We thus sort all of our planet measurements by date and by HWP angle. As with the intensity template measurements, planet scans are only included in our list of measurements if they have at least 300 successful bolometer gain fits to the planet and to the thermal source calibration before and after the planet scan.

To create our $P_{\rm frac}$ template within one epoch we begin by assigning the template $P_{\rm frac}$ value at HWP angle θ_{HWP} the median[2] value of all measurements at that angle. We then attempt to estimate the errors on the measured values of $P_{\rm frac}$ directly from the data in a way that is tolerant of outliers. For all θ_{HWP} with a number of measurements $N_{obs,\theta}$ greater than three, we calculate the median absolute deviation (MAD) of the measurements. The MAD is a statistic which is used infrequently enough to warrant definition here. The MAD for a given set X is calculated as:

$$\mathrm{MAD} \equiv \mathrm{median}_i(|X_i - \mathrm{median}_j(X_j)|) \tag{3.25}$$

For a given pixel, we choose the maximum value of the MAD from all the sets of measurements at different values of θ_{HWP} with greater than three measurements and use this maximum value as representative of the variance in $P_{\rm frac}$. We then calculate the error at each θ_{HWP} with a measurement as:

$$\sigma_{P_{\rm frac}} = \frac{\mathrm{MAD}}{1.48\sqrt{N_{obs,\theta}}} \tag{3.26}$$

[2]We use the standard technique of taking the mean of the two middle values for sets with an even number of measurements. HWP angles with only a single measurement of $P_{\rm frac}$ are dropped.

where the factor 1.48 corrects for the difference between the MAD and the standard deviation as estimators of variance. For values of θ_{HWP} with fewer than three measurements, we use the estimate for $\sigma_{P_{\rm frac}}$ from equation 3.24 if it is larger than the value calculated with 3.26.

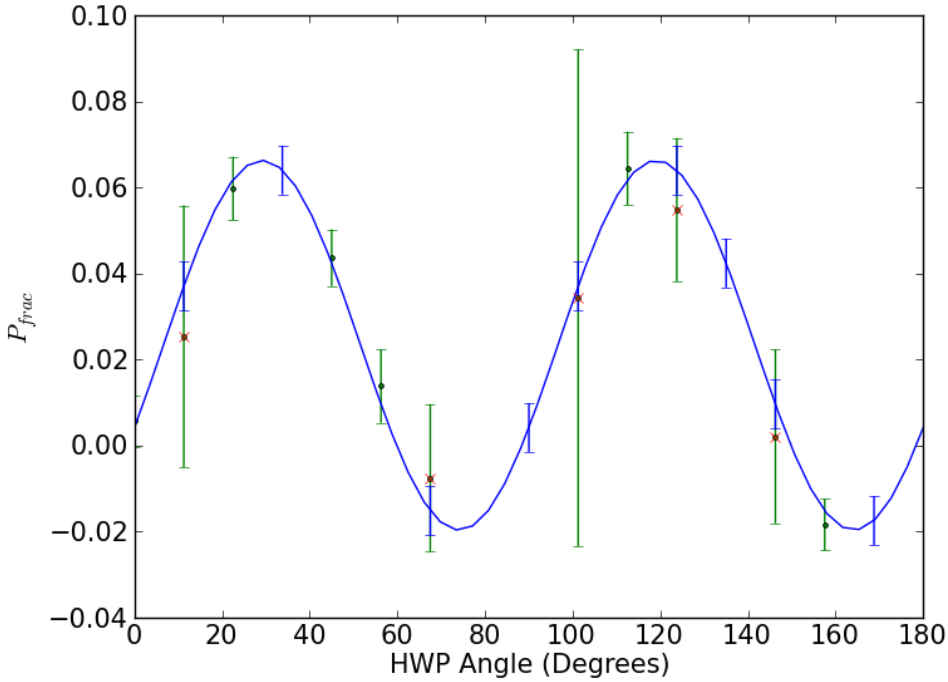

Figure 3.7: Thermal source polarization data and model fit are shown for a single bolometer over one epoch. The data is measured from 35 planet scans taken at 11 different HWP angles. Data from the planet measurements along with error bars are shown in green. The blue curve shows the model fit. Blue error bars indicate HWP angles where the model fits are used in the gain model due to lack of planet scan coverage. A red "X" over a green point indicates that the model fit replaced the planet scan data at that HWP angle.

Because we do not have a large number of planet scans at every HWP angle we would like to calibrate data for, we also create a model for $P_{\rm frac}$ as a function of HWP angle. We can then reconstruct $P_{\rm frac}$ at angles where we do not have enough planet scans to make the measurement with the desired precision. The model we use is:

$$P_{\mathrm{frac}}(\theta_{HWP}) = O_{NR} + P_a \cos(4\theta_{HWP} - 2\alpha). \tag{3.27}$$

In our model, O_{NR} represents an intrinsic relative gain offset for a pixel and has no HWP dependence. We would expect this term to arise from a source of polarization that is produced on the bolometer side of the HWP; mismatched bandpass spectra are a good candidate for generating this. P_a parameterizes the fractional amplitude of the polarization that is rotated by the HWP, and α sets the phase of that polarization. We thus expect P_a and α to account for the polarization that occurs in the thermal calibration source. The fit is performed using the median value weighted by the inverse square of the errors calculated above. An example of median P_{frac} values, errors, and the model fit is shown in figure 3.7. Though we will show some modeling of induced pixel-pair relative gain errors based on assuming these errors are correct, this will only serve as a cross check of other techniques to constrain relative gain error. The most important role the errors play is in dictating how to weight the measurements at different HWP angles during the fitting process.

To construct the final template over an epoch, we use the model fit to replace our planet measurements of $P_{\mathrm{frac}}(\theta_{HWP})$ at HWP angles where there are fewer than three direct measurements. This includes values of $P_{\mathrm{frac}}(\theta_{HWP})$ at angles where there are no planet measurements, but where we have CMB data we would like to gain calibrate. The errors on the model fit are estimated from the standard deviation of the model fit and the measurement at each point included in the fit. Information about the differences between the gain model epochs is summarized in table 3.1.

An example of the P_a values is shown in figure 3.8. The general form of the spatial distribution of polarization seen in this figure is maintained through all four epochs of the relative gain model. We see that at its maximum the thermal source is about 5.8% polarized. The origin of this polarization and the reason for it having this spatial distribution has not been investigated.

An example of values for α is shown in figure 3.9. The alternating rows of different polarization orientations within a wafer can be seen. Comparing the

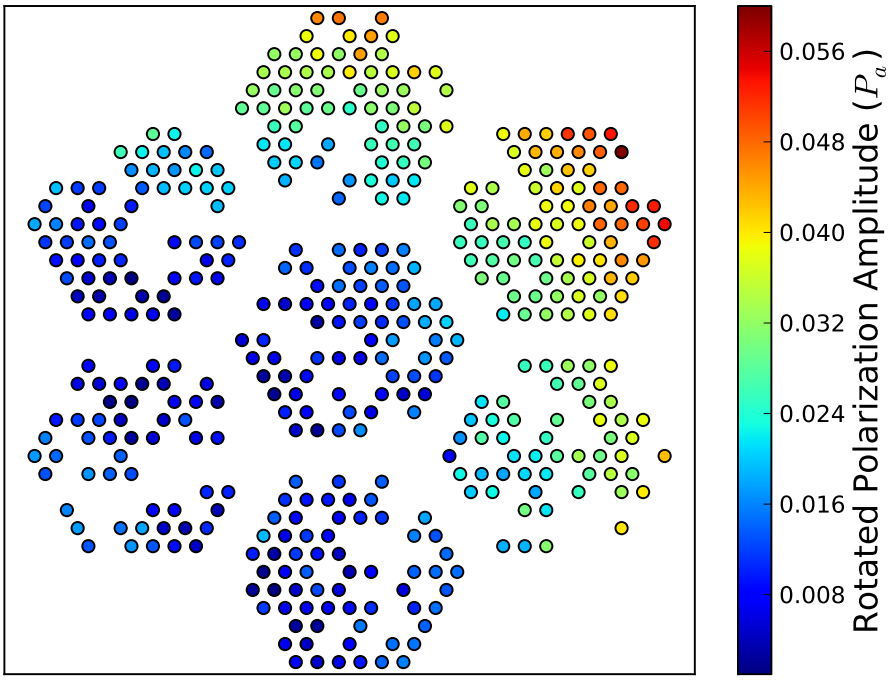

Figure 3.8: The thermal source P_a values for the first gain model "epoch," composed of the time between June 27th, 2012 and September 23rd, 2012. The variation in amplitude of the thermal source polarization in clearly seen as a function of focal plane position.

spacial distribution of P_a and α values, it is clear that the alternation of orientation angles between rows is most prominent where P_a is highest. The higher polarization in these regions gives more signal-to-noise on the fit, allowing for a better determination of α.

Finally, an example of O_{NR} values is shown in figure 3.10. There is no obvious geometric pattern here, other than the fact that the bottom wafer in the plot has a higher number of pixels with above average O_{NR}. This is wafer 9.4.

Combining values for P_a, α, and O_{NR} with direct values from the measurements of P_{frac} in the way described above allows us to construct the four $P^j_{\text{frac}}(\theta_{HWP})$ templates across the different epochs and thus correctly use the thermal calibration source to set the pixel-pair relative gain.

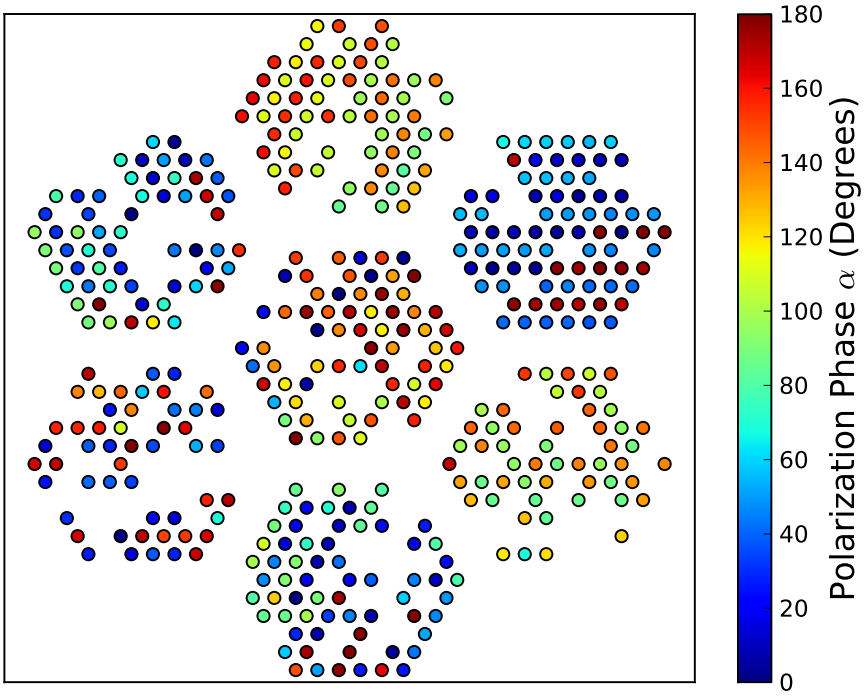

Figure 3.9: The thermal source α values for the first gain model "epoch," composed of the time between June 27th, 2012 and September 23rd, 2012. The alternation of polarization orientation along different rows of pixels within a wafer is clearly visible.

3.1.6 Gain Generation

Once we have our gain model templates $P^j_{\text{frac}}(\theta_{HWP})$ and I^j, we are able to generate gain values for any measurement taken with the thermal calibration source, assuming we also know the angle of the HWP at which the measurement was taken. Values of I^j are constant across all HWP angles and all gain epochs, but the values of $P^j_{\text{frac}}(\theta_{HWP})$ must be chosen for the correct HWP angle and gain model epoch. We use the values of I and P_{frac} for each pixel to form the thermal source effective temperatures T^t and T^b for the two bolometers in that pixel as in equation 3.18. We then generate our gain for each bolometer at each thermal source observation as:

Table 3.1: A summary of the four gain model epochs is shown. "# of Measurements" indicates the number of planet scans the template for the given epoch was created from. "HWP Angles" indicates the number of HWP angles sampled between the set of planet scans. "Cal. Method" indicates the calibration method used. The "direct" calibration method indicates the template is formed from direct measurement of $P_{\rm frac}$, "model" indicates values of $P_{\rm frac}$ are derived from the model in equation 3.17, and "both" indicates the template is formed from a combination of the two.

Epoch	Dates	# of Measurements	HWP Angles	Cal. Method
1	2012/06/27 - 2012/09/23	41	11	Both
2	2012/09/23 - 2012/10/03	8	7	Model
3	2012/10/03 - 2013/01/28	48	8	Both
4	2013/01/28 - 2013/06/13	52	2	Direct

$$g^i_{\frac{T_{RJ}}{ADC}} = \frac{T^i}{A^i_{therm}}. \tag{3.28}$$

This value of $g^i_{\frac{T_{RJ}}{ADC}}$ multiplies our TOD in ADC counts to produce a TOD in K_{RJ}. More details of gain generation for CMB observations are described in section 4.2.

3.2 Polarization Calibration

Each pixel on the focal plane can measure the polarization field by differencing the power in orthogonal polarization directions corresponding to the physical orientation of the antennas for that pixel. This is equivalent to performing a measurement of a linear combination of the Stokes Q and U parameters. In order to co-add data from different pixels and different scans, we must know which linear combination a particular pixel is measuring at a particular time. For this we must calibrate the relative polarization orientation angles of the pixels.

Further, we must also know the absolute orientation of our polarization sensitivity on the sky. Knowing this absolute orientation angle is the only way to ensure consistency between our definition of Q and U and the Fourier plane az-

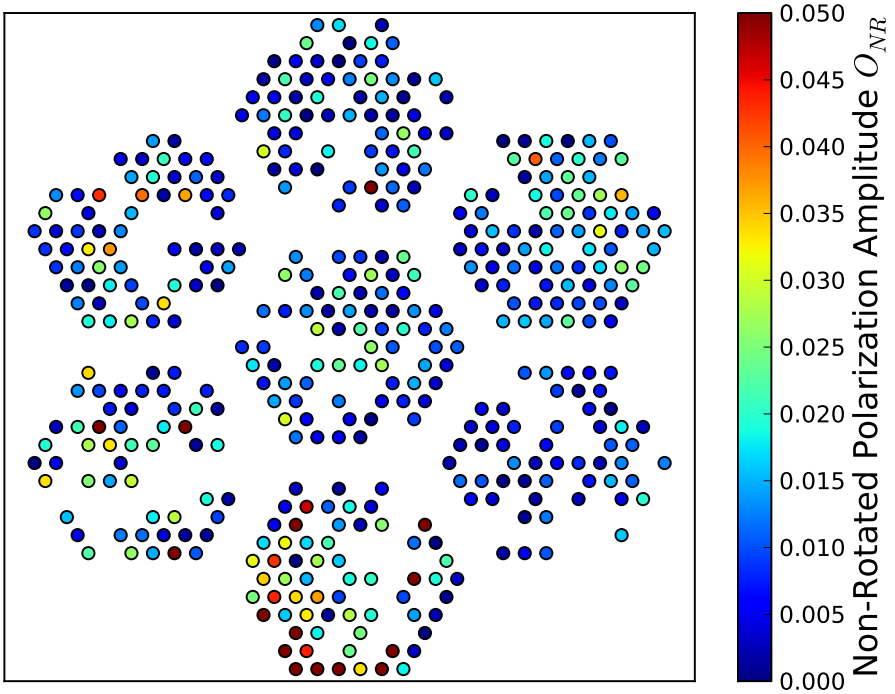

Figure 3.10: The thermal source O_{NR} values for the first gain model "epoch," composed of the time between June 27th, 2012 and September 23rd, 2012. This represents intrinsic pixel-pair relative gain which is not rotated by the HWP.

imuthal angle $\phi_{\vec{\ell}}$ from the Fourier decomposition of the polarization fields. Equation 1.19 makes it clear that offsetting $\phi_{\vec{\ell}}$ with respect to the frame in which we have defined Q and U is equivalent to rotating E into B. This is thus a significant source of potential systematic error for the C_ℓ^{BB} measurement.

If we have detector TOD from the top $d_{j,t}$ and bottom $d_{j,b}$ bolometers in a pixel j scanning over a source with polarized amplitude P oriented at an angle α, we detect:

$$d_j^{diff} = d_{j,t} - d_{j,b} = 2P\cos(2(\alpha - \Theta_j)) \tag{3.29}$$

where Θ_j is the polarization angle of the pixel j which we are interested in calibrating. Θ_j will change based on the HWP angle and based on the parallactic angle of the source we are measuring. We want to convert our measurements of

Θ_j into a measurement of θ_j defined by:

$$\Theta_j = \left(\frac{\pi}{2} - \theta_j\right) + 2\theta_{HWP}(t) + \theta_{PA}(t) \tag{3.30}$$

where we allow for a time dependent HWP angle $\theta_{HWP}(t)$ and parallactic angle $\theta_{PA}(t)$.

Measuring θ_j for all pixels across the focal plane relative to the same fixed angle on the sky α is equivalent to performing a relative calibration of the detector polarization angles. Measuring all the θ_j with respect to an α of known value in the RA/DEC coordinate system is equivalent to performing an absolute calibration of the detector polarization angles.

As with gain calibration, this calibration task separates into relative and absolute calibrations. Again, much like in the case of the gain calibration, we perform our relative calibration using local celestial sources and then use our knowledge of the CMB, in this case the C_ℓ^{EB} and C_ℓ^{TB} power spectra, to perform the absolute calibration. See section 4.8 for a discussion of absolute polarization angle calibration using the CMB.

3.2.1 Taurus A

Our primary source of relative polarization angle calibration is the celestial object Taurus A (Tau A), also known as M1 or the Crab Nebula. Tau A is approximately 7% polarized in our observation band, and is visible from the James Ax observatory site. We scan Tau A in an identical fashion to the planet scans described in section 3.1.1, though the analysis differs significantly. This data allows us to track our relative detector angle as a function of HWP angle and time. It also serves as a first pass for absolute calibration of the polarization orientation before it is finalized using the CMB.

POLARBEAR observed Tau A several times per week over the first season of observations, except for the period from May to July annually when Tau A is within 30° of the Sun on the sky. There are a total of 125 Tau A observations used to calibrate the first season data set. A full co-added map of all the observations is shown in figure 3.11.

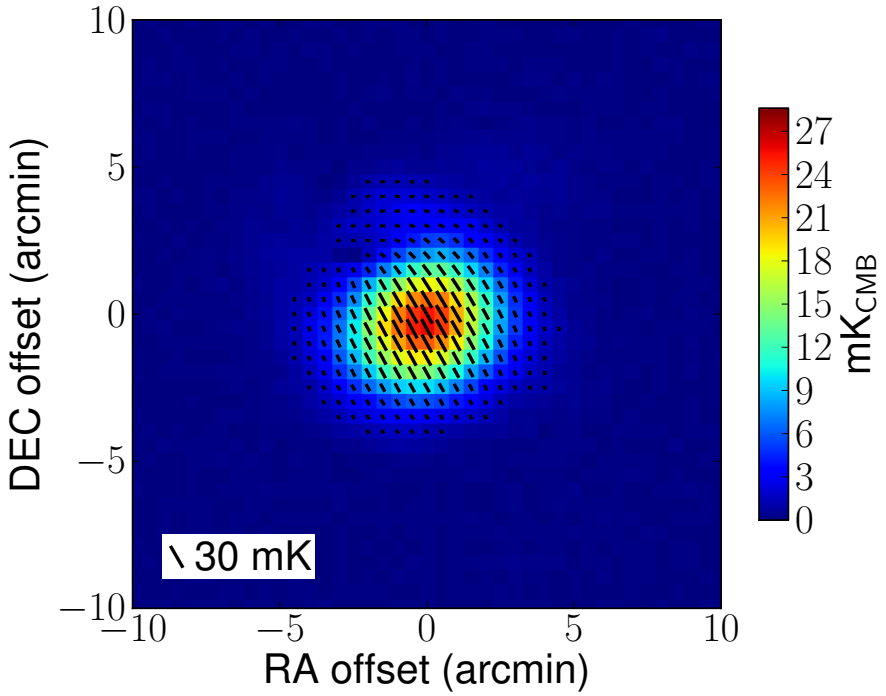

Figure 3.11: A full season co-added polarization map of Tau A observed by POLARBEAR. The orientation of the bars in the map pixels represent polarization angles at each map pixel, and the color represents the polarized intensity. Figure from [43].

To proceed with the determination of our set of θ_j, the bolometer and pointing TOD from each detector are collected across the 125 scans to form a single TOD for each bolometer. The TOD from all times a bolometer is within five arcminutes of the center of Tau A is included in the single full season TOD for that bolometer after gain calibrating, normalizing and filtering. The pointing data is used to find $\theta_{PA}(t)$ for the included times, and the HWP angle TOD $\theta_{HWP}(t)$ is constructed for this full season TOD as well.

Tau A's polarization has been measured at 90 GHz by the IRAM telescope as reported in [57]. We measure the polarization orientation angle of individual pixels by comparing the POLARBEAR full season TOD from Tau A to the data from the IRAM telescope. The IRAM beam is approximately 30 arcseconds at FWHM, so we first convolve the IRAM Tau A I, Q, and U maps with the POLARBEAR beam of each bolometer modeled as an elliptical Gaussian with parameters fit from

planet scans. We then create simulated TOD $I_{sim,j,(t/b)}(t)$, $Q_{sim,j}(t)$, $U_{sim,j}(t)$ using the POLARBEAR pointing information for each pixel j from our full season Tau A TOD to scan the IRAM maps. Our notation on the I TOD indicates there is an individual TOD formed for the top and bottom bolometers in the pixel j to accomodate any differential beam shape between them. We model our full season TOD as:

$$\begin{aligned} d_j^{diff}(t) &= \frac{1}{2}(I_{sim,j,t}(t) - I_{sim,j,b}(t)) \\ &+\epsilon_j[Q_{sim,j}(t)\cos(2\Theta_j(t)) + U_{sim,j}(t)\sin(2\Theta_j\{t\})] \\ &+\frac{\Delta g_j}{2}[I_{sim,j,t}(t) + I_{sim,j,b}(t)] \end{aligned} \tag{3.31}$$

where Θ_j is related to our calibration angle θ_j by equation 3.30. For each pixel there are three parameters to fit: the pixel polarization angle θ_j, the pixel polarization efficiency ϵ_j, and the pixel-pair relative gain error Δg_j. ϵ allows for some depolarization of the signal due to non-idealities of the detectors, and Δg allows for some leakage of temperature to polarization. When performing the fit we use $\theta_{HWP}(t)$ and $\theta_{PA}(t)$ to convert from Θ_j to θ_j. The fit is performed as a χ^2 minimization differencing between our real TOD and the model, and with errors given by the standard deviation of the real TOD. Note that Δg_j is an independent measurement of the pixel-pair relative gain which we can compare to our values from the thermal source template in section 3.1.5. This comparison will be addressed in section 5.1.1 as part of our C_ℓ^{BB} systematics discussion.

We compare the difference of our measured angles with theory and subtract a mean offset of each wafer from the distribution for that wafer. Pixels that are more than 3σ outliers in the full distribution across the focal plane are rejected and not considered in further analysis. A plot of the remaining pixel orientation angles θ_j are shown in in figure 3.12. A comparison between these measured angles and the angles as designed is shown in figure 3.13. The measured angles are used in combination with the HWP angle and $\theta_{PA}(t)$ in subsequent analyses to determine which linear combination of Q and U a pixel sees during a particular scan, making them the source of relative calibration of the polarization angles for the experiment. We also allow for a single global rotation of these angles, the choice

of which constitutes the absolute calibration. The absolute calibration procedure is described in section 4.8.

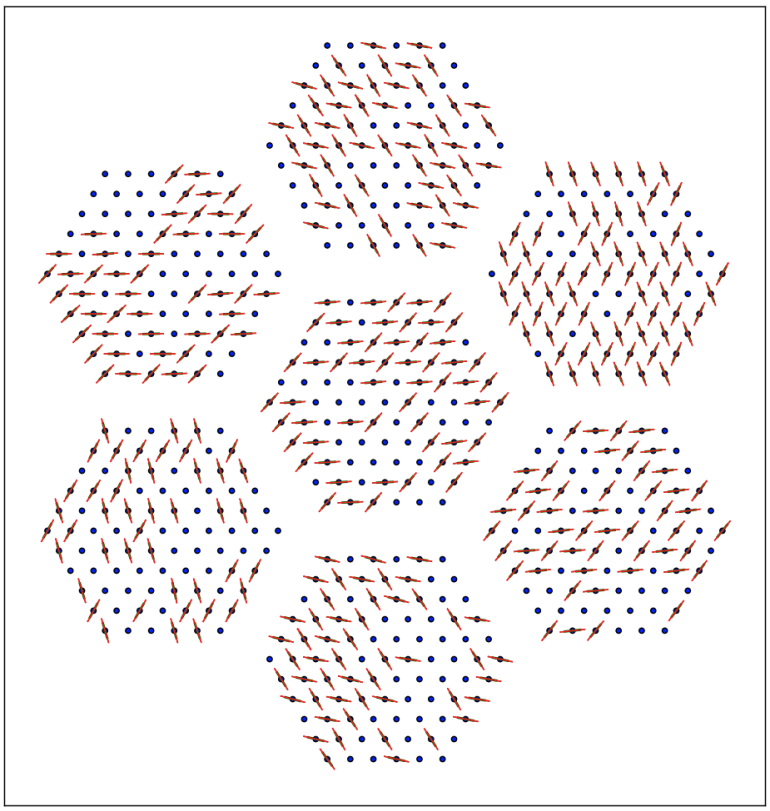

Figure 3.12: Polarization angles θ_j calibrated with Tau A plotted against the pixel location on the focal plane. The central angle is plotted in green, with error bars plotted in red at $\theta_j \pm \sigma_{\theta_j}$. The separation of the error bars are not visible at this scale. The intentional variation in polarization angle designed into each wafer is clearly seen.

3.2.2 Dielectric Sheet Calibrator

A hardware calibration source designed to perform both absolute and relative pixel polarization angle calibration is the dielectric sheet calibrator (DSC). The device uses a thin dielectric sheet to act as a partial beam splitter, largely transmitting radiation from the sky but also reflecting some thermal radiation from a room-temperature millimeter-wave absorber material. Different fractions of the room temperature black body radiation are reflected parallel and perpen-

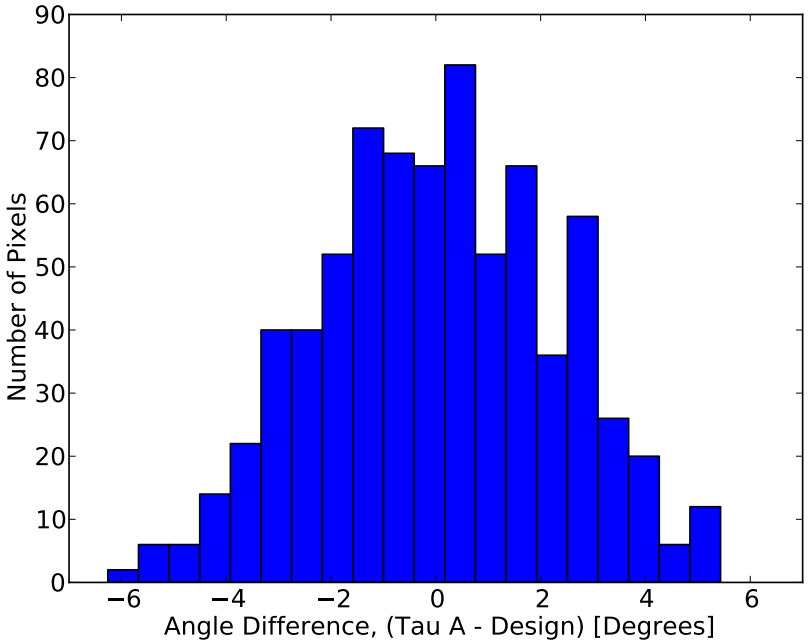

Figure 3.13: A comparison between design polarization angles and Tau A calibrated polarization angles. The difference $\theta_{j,\text{Tau A}} - \theta_{j,\text{design}}$ is shown.

dicular to the plane of incidence, which generates the polarization. The calibrator is arranged in such a way that light from the sky enters the cryostat after being transmitted through the sheet, as does the small fraction of reflected room temperature black body radiation. The calibrator has a heritage from the POLAR [58] and BICEP1 [59–61] and BICEP2 [62] experiments. The principle of operation is illustrated in figure 3.14.

For simplicity we may imagine that our detector polarization axis is aligned with the unprimed coordinate system in figure 3.14, and that this is also aligned with the coordinate system in which we are measuring the Stokes Q or U parameters. We may then write, following [63]:

$$\begin{aligned} I_x &= T_C + (T_H - T_C)R_{TE}, \\ I_y &= T_C + (T_H - T_C)R_{TM}, \\ Q &= (T_H - T_C)(R_{TE} - R_{TM}), \\ U &= 0, \end{aligned} \tag{3.32}$$

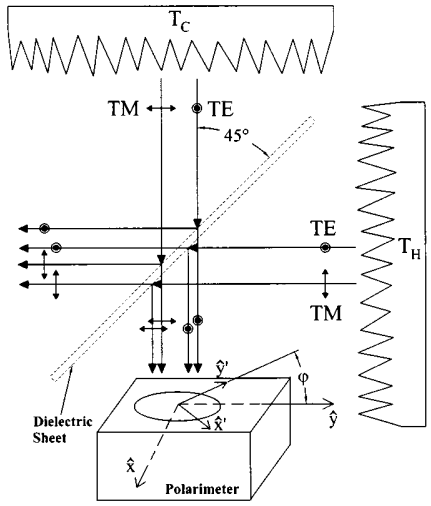

Figure 3.14: Schematic diagram of the DSC operating principle. T_C represents radiation coming from the sky at a lower effective temperature than radiation coming from a room temperature millimeter-wave black body T_H. Reflection and transmission coefficients are different between directions of polarization parallel and perpendicular to the plane of incidence. These two polarization orientations are represented by "TE" (perpendicular to the plane of incidence) and "TM" (parallel to the plane of incidence). Figure from [63].

where I_x and I_y are the signals seen by the two bolometers in a single pixel, Q is the signal seen by differencing the two bolometers, T_C represents the effective sky temperature after being propagated through the primary and secondary reflectors, T_H represents the temperature of our millimeter-wave absorber, and R_{TE} and R_{TM} represent the coefficients of reflection along the axes perpendicular and parallel to the plane of incidence, respectively. Note we have neglected any emission coming from the sheet. It is then possible to rotate these values around the optical axis by an angle ϕ:

$$\begin{aligned} I_{x'} &= I_x \cos^2(\phi) + I_y \sin^2(\phi), \\ I_{y'} &= I_x \sin^2(\phi) + I_y \cos^2(\phi), \\ Q' &= Q \cos(2\phi), \\ U' &= -Q \sin(2\phi). \end{aligned} \tag{3.33}$$

The physical calibrator is mounted on the telescope directly in front of the receiver, which places it after the primary and secondary reflectors in the optical

path of light coming from the sky. It is mounted with a bearing in such a way that we can rotate the sheet of dielectric material around the optical axis, the equivalent of changing ϕ in equation 3.33. This allows us to modulate the angle of polarization entering each detector, which modulates the signal each detector sees. By comparing the phase of the modulation across the focal plane we can calibrate the polarization angles relative to each other. A gravity reference is also installed which allows us to compare the angle of the sheet to the local gravity vector as the bearing rotates. In theory this should provide a frame of reference that would allow the DSC to serve as an absolute angle calibrator, but the gravity reference has not yet been made to work reliably. A Solidworks^{TM} rendering of the DSC mounted in the telescope is shown in figure 3.15.

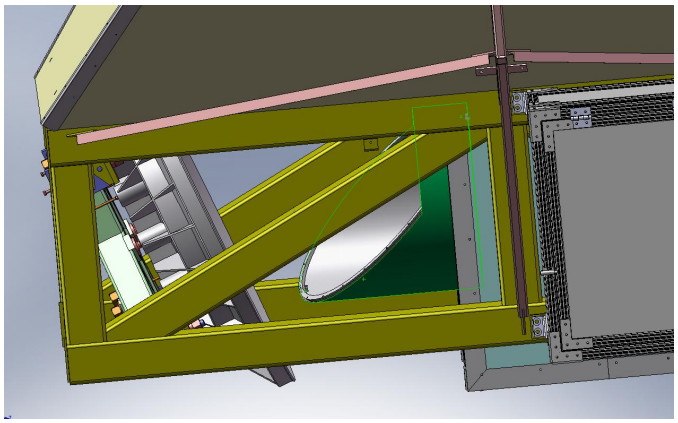

Figure 3.15: The DSC is seen mounted on HTT in this Solidworks^{TM} rendering. The frame for the DSC is pictured highlighted in green. The dielectric material is mounted between two elliptical rings (pictured) mounted on this cylinder at approximately 45° from the optical axis. The secondary reflector is pictured to the left of the DSC, and the primary reflector is up and to the right (not pictured).

The reflection coefficients $R_{TE/TM}$ along either axis are functions of the index of refraction of the dielectric material n, the wavelength of radiation, the thickness of the dielectric sheet, and of the angle of incidence θ. The material we chose to use is 0.003 inch thick polypropylene ($n \approx 1.5$). We have designed the mount for the DSC such that the angle of incidence for rays on the optical axis is 45°. However, rays off of the optical axis will have different angles of incidence. The angle of incidence required to reflect rays into a particular off-axis detector will

also change as a function of ϕ, so we must allow for θ to depend on ϕ. This means that in addition to the desired twice-per-rotation modulation ($2f$) of polarization by the calibrator, some detectors will also see a once-per-rotation modulation ($1f$) signal.

An optical encoder tape is mounted around the circumference of the DSC mounting cylinder. This allows us to record the angle ϕ of the calibrator to a resolution of half an arcminute while the DSC rotates.

Trial Run

The DSC was operated in March of 2013. It was used in two different modes, both of which involved stepping the calibrator in ϕ and integrating for 2 seconds at each position. This two second integration period provides sufficient signal to noise such that the calibration is limited by systematic effects and not statistical errors. In one mode the DSC was stepped at one degree increments over the full 360 degree range of ϕ. In the second mode the calibrator was stepped in two degree increments over 360 degrees, offset by one degree, and then stepped in reverse at two degree increments. The orientation of the calibrator in the ϕ direction is maintained between scans so that they may be compared. In total there were five measurements recorded using these techniques.

Gain calibrated pixel difference TOD are formed from the five measurements. The mean and standard deviation of each constant velocity position is recorded and associated with its encoder reported ϕ value, giving a measurement and error on a vector of ϕ values. The values from the five measurements are interpolated onto the same set of ϕs so that they may be directly compared. In order to combine the five measurements into a single set of values and errors, we compute the weighted mean and standard deviation at each value of ϕ across our five measurements, weighting values for each individual measurement by the inverse variance of the TOD over the two seconds they were recorded.

Our ultimate goal is to fit a model to these values that will allow us to determine the polarization orientation angle of the bolometers. However, during the data taking process it became apparent that the material we purchased was not

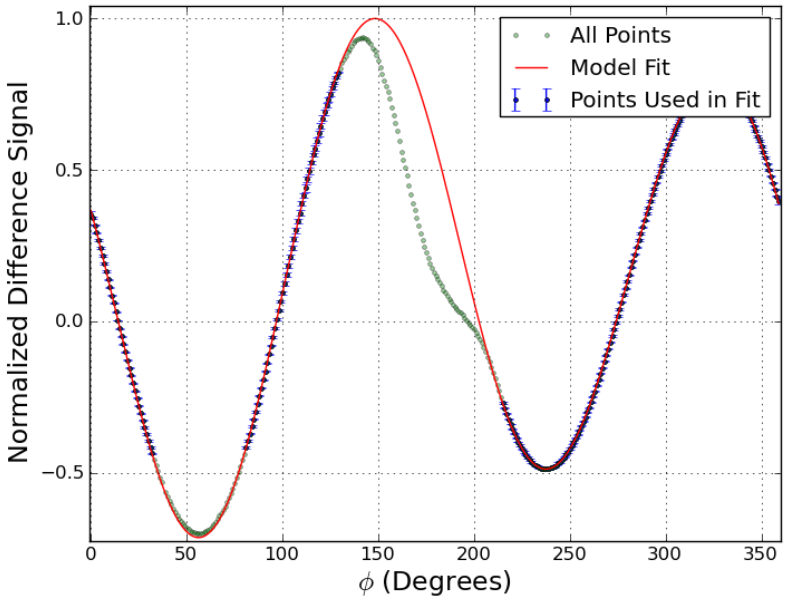

Figure 3.16: Normalized difference data are plotted for a single pixel as a function of DSC rotation angle ϕ. All recorded points are displayed in green. Points included in the model fit are shown with their error bars in blue. Green points without a corresponding blue point and error bar were excluded from the fit due to suspected detector saturation. The model fit is shown in red.

standard polypropylene. It is not clear if the emissivity of the material we received is significantly higher or if its index of refraction is different, or some combination of these effects. The result was that the polarization signals generated during rotation were much stronger than desired in a way that was sufficient to drive many of the bolometers out of their linear electrothermal feedback regime ("saturate" the bolometers), generating unreliable measurements. Our partial solution to this problem is to look at each bolometer TOD individually and set limits on how much the calibrated signal can change from the point where the detectors were biased. Values of ϕ where either bolometer in a pixel exceeded this threshold are excluded. We attempt no fits to pixels where more than 50% of our ϕ values have suspected saturation.

Proceeding with the data that remains, we take our set of values and errors for the difference signal in each pixel j and fit them to a model:

$$d_j^{diff}(\phi) = O_j + A_{1f,j}\cos(\phi - \theta_{1f,j}) + A_{2f,j}\cos(2(\phi + \theta_{2f,j})) \\ +A_{3f,j}\cos(3\phi - \theta_{3f,j}) + A_{4f,j}\cos(4\phi + \theta_{4f,j}). \tag{3.34}$$

This model allows for a single overall offset and an amplitude and phase of four harmonic terms that have one, two, three, and four periods over the full range of ϕ. We take $\theta_{2f,j}$ as the phase of our polarization orientation for pixel j; all other amplitudes and phases are present to accomodate unwanted systematic effects such as the variation of θ with ϕ, misalignment of the bearing with the optical axis of the receiver, or other more subtle variations such as changes in the thickness of the dielectric sheet over its surface or bowing of the dielectric material due to gravity, which could in principle generate a signal at any harmonic. An example of the DSC measurement and fit for a single pixel is shown in figure 3.16. Values of the θ_{2f} terms are shown in figure 3.17 for all pixels with successful measurements. These values contain information about the relative orientation of detectors on the focal plane but do not contain absolute orientation information. A comparison with the values determined by the Tau A measurement is shown in figure 3.18.

The results of this trial are far from ideal. The saturation observed in the bolometers prevented many pixels from being fit, and has left an unquantified residual contamination in pixels that were fit. We could attempt to quantify this error by investigating the dependence of our fit parameters on the values of our cut criteria. However, it is clearly preferable to perform a new measurement with a better dielectric material. A more rigorous investigation of systematic errors on the basis of a future measurement uncontaminated by saturation would yield a better understanding of the DSC's utility.

It is worth noting that because the DSC is located between the secondary reflector and the cryostat, it will never measure polarization rotation induced by the reflector optics. The overall optics of the instrument exhibit a degree of distortion, which will also rotate polarization angles. This distortion is believed to be induced by the reflector optics, though it is not currently well modeled. This distortion can be seen in figure 3.19. The intrinsic accuracy of the DSC will always be limited to the accuracy of our ability to model this effect, though the modeling of this may in

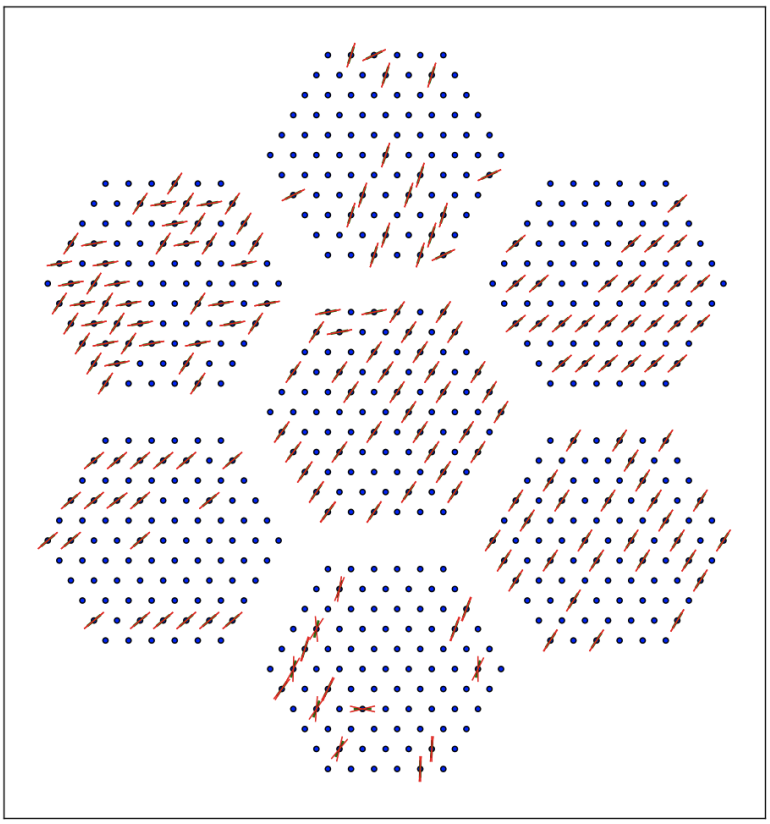

Figure 3.17: Relative polarization angles from the phase term θ_{2f} plotted with the pixel location on the focal plane. The central angle is plotted in green, with statistical error bars plotted at $\theta_j \pm \sigma_{\theta_j}$. The errors are most pronounced in the lowest wafer in the plot, and the separation of the error bars is visible there. Systematic errors are not estimated. Missing pixels were either not active during data acquisition or greater than 50% of their data was acquired with a saturated bolometer.

the future become very good. Polarized celestial sources or polarized calibration sources placed on nearby mountains include the effect of all optical elements and would not be limited by the need to model distortion induced by the reflectors.

3.3 Pointing and Beam Offsets

The encoders attached to the bearings of the azimuth and elevation axes of the telescope report the angular positions of these axes at 95.4 Hz while the telescope is scanning. The offsets of these values are designated such that they

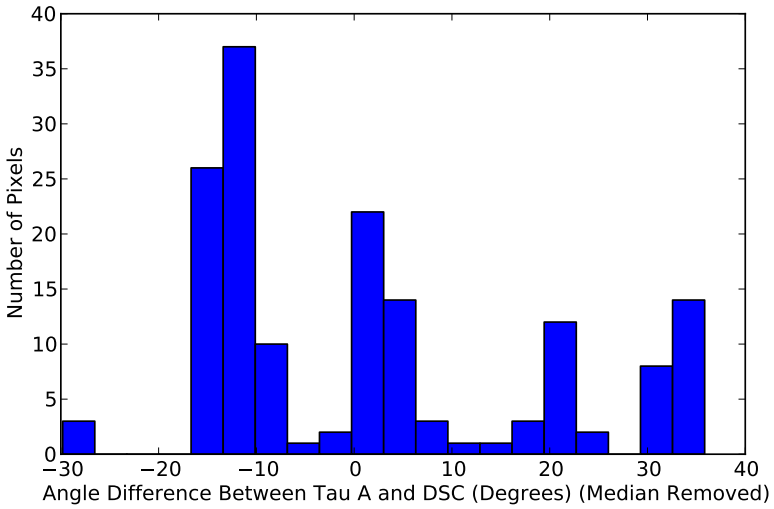

Figure 3.18: A comparison between Tau A and DSC angle measurements. The difference between the two measurement techniques is shown per pixel, with the median difference removed. The multi-peak structure is formed by the different wafers.

represent the approximate boresight direction of the antenna. Due to flexure of the antenna structure, non-orthogonality of the telescope axes, and other mechanical effects, the actual offset between the encoder reported positions and the true boresight pointing is a function of the azimuth and elevation the telescope is scanning at. We use the five-parameter model described in [64] to account for these effects, and refer to this fit as our "pointing model."

The pointing model was created by observing millimeter-wave sources of known locations which span a wide range of azimuth and elevation in the observation frame. The azimuth and elevation of each source is determined from the scan and compared to its known location to determine the correct offsets at the azimuth and elevation of the scan. The values of these offsets at different azimuths and elevations are used to fit the model parameters. The pointing model can then be used to correct the encoder reported azimuth and elevation values to the correct boresight azimuth and elevation. The best-fit pointing model recreates the locations of the input sources with an RMS accuracy of 25 arcseconds.

The pointing models establishes the boresight pointing of the antenna, but it is also necessary to know the offsets of individual bolometers relative to the

boresight. These offsets are established by using raster scans of Saturn and Jupiter of the type described in section 3.1.1. The detector offsets in combination with the boresight pointing model are used to build a pointing TOD for each bolometer. The measured beam offsets are shown in figure 3.19.

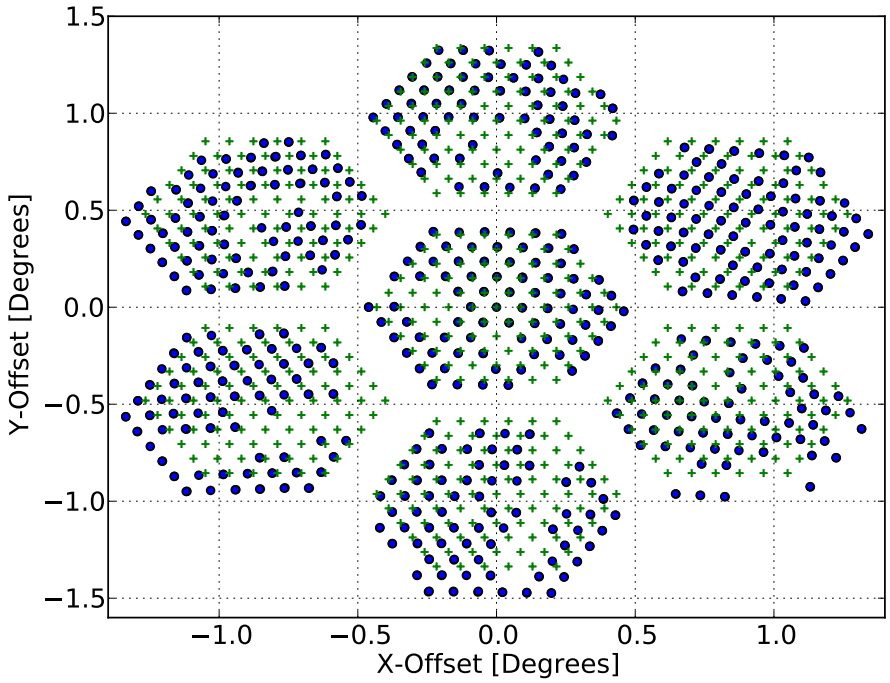

Figure 3.19: A comparison between the as-designed (distortion-free) beam offsets and the measured beam offsets. The as-designed offsets are shown as green plus marks, and the measured offsets are shown as blue circles.

3.4 Instrument Beam

The diffraction-limited optics in the telescope limit the spatial resolving power of the instrument. In terms of the sky maps that the instrument creates, this is equivalent to "blurring" the image of the sky. In Fourier space, it is equivalent to suppressing signal at higher ℓ-modes. We must measure and account for the effect the beam has on the measurements in order to accurately measure the power spectra we are interested in. We do this by measuring B_ℓ, the ℓ-space Fourier

transform of the noise weighted, co-added, azimuthally averaged beam map of all the working bolometers on the focal plane. The beam maps come from planet scans of the kind described in 3.1.1. We use B_ℓ to represent the combined effect of all our detectors mapping the sky.

Errors in the pointing model can create additional blurring in the map, or equivalently reduced sensitivity to structure at higher values of ℓ. This is because inaccuracies in the pointing model mean that when data from different azimuths and elevations are added together, the map is effectively blurred. We modify B_ℓ to create an effective $B_\ell^{\rm eff}$ that accounts for this blurring. This is modeled as:

$$B_\ell^{\rm eff} = B_\ell e^{-\ell(\ell+1)\sigma_p^2/2} \tag{3.35}$$

by fitting for σ_p in each patch by using the blurring of point sources within the temperature map of that patch. This means that we use a different effective beam for each patch. These effective beams are shown along with the B_ℓ calculated from Jupiter in figure 3.20 along with their uncertainties.

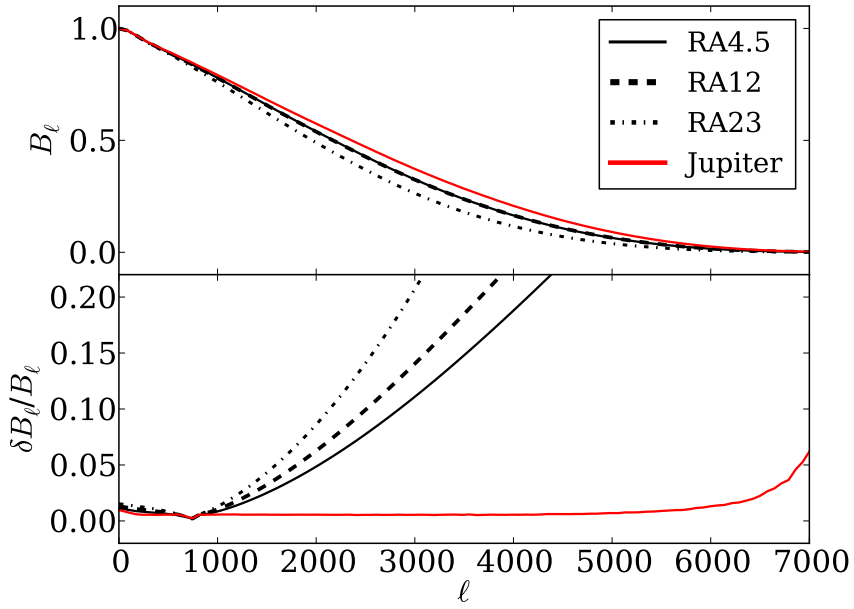

Figure 3.20: The B_ℓ calculated from Jupiter measurements is shown in red in the upper plot. The values of $B_\ell^{\rm eff}$ for each patch are shown as dotted lines. The errors are shown below. Figure from [43].

The knowledge of B_ℓ is used to correctly reconstruct the measured power spectra, as described in 4.6.

Figures 3.11 and 3.20 are reprints of material as it appears in A Measurement of the Cosmic Microwave Background B-Mode Polarization Power Spectrum at Sub-Degree Scales with POLARBEAR. The POLARBEAR Collaboration: P. A. R. Ade, Y. Akiba, A. E. Anthony, K. Arnold, M. Atlas, D. Barron, D. Boettger, J. Borrill, S. Chapman, Y. Chinone, M. Dobbs, T. Elleflot, J. Errard, G. Fabbian, C. Feng, D. Flanigan, A. Gilbert, W. Grainger, N. W. Halverson, M. Hasegawa, K. Hattori, M. Hazumi, W. L. Holzapfel, Y. Hori, J. Howard, P. Hyland, Y. Inoue, G. C. Jaehnig, A. H. Jaffe, B. Keating, Z. Kermish, R. Keskitalo, T. Kisner, M. Le Jeune, A. T. Lee, E. M. Leitch, E. Linder, M. Lungu, F. Matsuda, T. Matsumura, X. Meng, N. J. Miller, H. Morii, S. Moyerman, M. J. Myers, M. Navaroli, H. Nishino, H. Paar, J. Peloton, D. Poletti, E. Quealy, G. Rebeiz, C. L. Reichardt, P. L. Richards, C. Ross, I. Schanning, D. E. Schenck, B. D. Sherwin, A. Shimizu, C. Shimmin, M. Shimon, P. Siritanasak, G. Smecher, H. Spieler, N. Stebor, B. Steinbach, R. Stompor, A. Suzuki, S. Takakura, T. Tomaru, B. Wilson, A. Yadav, and O. Zahn, ArXiv e-prints, Mar. 2014. The dissertation author made essential contributions to many aspects of this work.

Chapter 4

Data Analysis

Over its first season of observations, POLARBEAR recorded more than 1.6 million bolometer-hours with successful gain calibrations following the procedures described in section 3.1. In the case of the C_ℓ^{BB} power spectrum analysis, our goal is to take these 1.6 million bolometer-hours, or more than one trillion individual bolometer samples, and reduce them to just four numbers which represent an estimate of the C_ℓ^{BB} power spectrum in four bins across a multipole range from $500 < \ell < 2100$. We focus on this range in ℓ-space because it contains the peak of the C_ℓ^{BB} spectrum predicted to be generated by gravitational lensing.

This process begins by preparing and cleaning the data. We then move to forming filtered sky maps of the three individual patches we scan. Using these maps, we then form estimates for the six power spectra C_ℓ^{TT}, C_ℓ^{EE}, C_ℓ^{TE}, C_ℓ^{TB}, C_ℓ^{EB}, and C_ℓ^{BB} that we want to measure. We will focus on providing a clear explanation of how this pipeline works, highlighting the specific choices made in the case of POLARBEAR data analysis. We will also point out where in this procedure the C_ℓ^{BB} pipeline branches into a separate pipeline for the C_L^{dd} analysis. We will then describe several studies done to constrain the impact of systematic errors on our results.

4.1 Low Level Data Processing

As described in section 2.8, the bolometer data is recorded at 190.7 Hz and the telescope encoder data from the elevation and azimuth axes is recorded at 95.4 Hz. For this analysis we are concerned with reconstructing signals at multipoles up to $\ell < 2100$. These multipoles have an angular period on the sky of roughly $\frac{360^\circ}{2100} = 0.17^\circ$. With a telescope scan velocity on the sky of 0.8 $^\circ/s$, these spacial frequencies are mapped into our TOD at a maximum frequency of about 4.7 Hz. The 190.7 Hz gives us substantially more bandwidth than we need to reconstruct our signals of interest. Our first data processing step is thus to down-sample the data by a factor of six to 31.8 Hz, still conservatively a factor of seven above the highest frequencies of interest. This reduction in data volume reduces the computational resources required in the subsequent stages of processing. At the same time our encoder data is linearly interpolated to the bolometer sample times and similarly down-sampled to 31.8 Hz. We are left with 31.8 Hz time synchronous bolometer and encoder TOD which we use in the remaining stages of the analysis.

4.2 Detector Gain Generation

During CMB observations the thermal calibration source is used at the beginning and end of every hour. The bolometer bias voltages are fixed over these hour long observation cycles, but the telescope changes its observation elevation every 15 minutes as described in section 2.2.3. We generate two gain values for every bolometer of the form:

$$g^i_{\frac{\mathrm{T_{RJ}}}{\mathrm{ADC}}} = \frac{T^i}{A^i_{therm}} \tag{4.1}$$

following the procedures outlined in section 3.1 and using the thermal calibration data from the beginning and end of every hour-long observation. We generate gains only for pixels where both the top and bottom bolometers have a successful fit for A^i_{therm}.

We make the choice to interpolate the bolometer gains as a linear function of time over this hour long period. An alternative would be to interpolate the

gain as a function of the elevation steps we take during the hour; that is, assume that the gain changes over the hour are directly related to the change in telescope elevation angle during the observation. This second possibility initially seems well motivated: the changes in atmospheric opacity associated with slewing the telescope elevation should change the gain of the detectors. However, we find that other effects such as varying atmospheric conditions dominate our changes in gain, and so we choose interpolation as a function of time to be the best approximation we can make. We will show later that the manner in which we interpolate has a negligible impact on our final estimate of the C_ℓ^{BB} spectrum.

We are left with a set of gains $g^i_{\frac{\mathrm{T_{RJ}}}{\mathrm{ADC}}}(t)$ as a linear function of time between the two thermal source observations. The gains are first interpolated to the beginning and end of every 15 minute CES and stored as one file per CES with the beginning and end gain values for each bolometer active in the scan. The gains are further interpolated to each time sample within the CES TOD when the data are loaded for processing.

4.3 Time Ordered Data Noise

Once we have the gain calibrations, we can compute the TOD noise of each pixel for each CES in which it is active. Computing this noise serves two purposes: it allows us to establish data selection criteria based on the noise in our data, and it is also used to weight the data so that we may optimally co-add it with data from different detectors or data taken at different times.

To compute the noise for each pixel, we take the gain calibrated top and bottom bolometer TOD for a single CES and compute their sum and difference. The sum TOD is the intensity TOD, corresponding to the total intensity in both polarizations. The difference TOD represents a linear combination of the Q and U Stokes parameters, depending on the polarization orientation angle of the pixel, the HWP angle, and the parallactic angle at the time of each sample in the TOD.

We subtract a first order Legendre polynomial from the sum and difference TOD over the CES and compute the power spectral density (PSD), which is the

square of the magnitude of the Fourier transform. This is the variance of the TOD as a function of frequency. We must then determine which frequencies are of interest to us in our analysis.

The range $500 < \ell < 2100$ corresponds to sinusoidal variations on the sky with an angular period of between 0.17° and 0.72°. These modes can be either variations of temperature or the Stokes Q or U parameters, depending on whether we are looking at intensity (pixel sum) or polarization (pixel difference). As the telescope scans over the sky, the spacial frequencies for a given CMB mode will map to different frequencies in the TOD depending on how the phase fronts of the mode on the sky are oriented with respect to the scan direction. Modes at a particular ℓ with phase fronts oriented perpendicular to the scan direction map to a TOD frequency of $\frac{\ell}{360^\circ} 0.8^\circ/s$, where $0.8^\circ/s$ is the scan speed of the telescope. Modes with non-perpendicular phase fronts map to lower frequencies, and modes with phase fronts parallel to the scan direction produce no modulation of the bolometer signal. This is represented in figure 4.1.

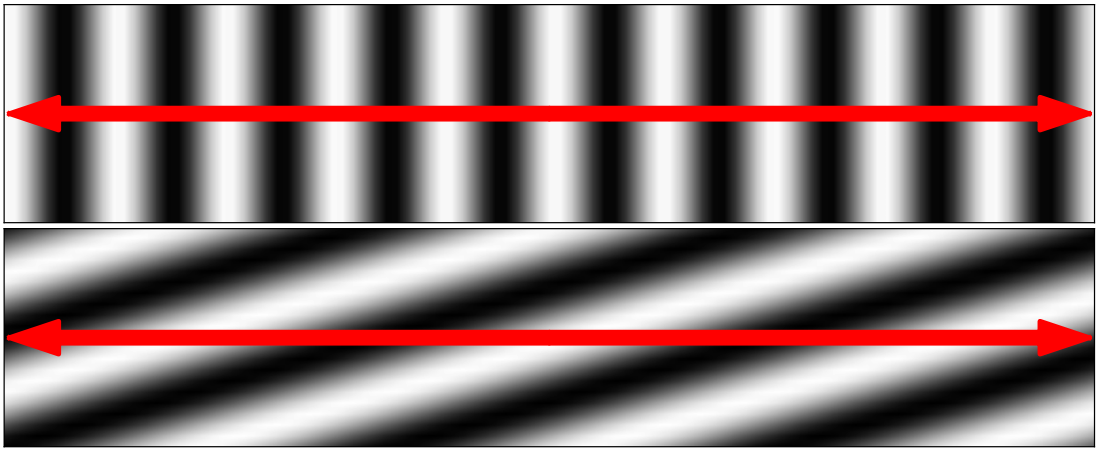

Figure 4.1: An example of single CMB modes representing either temperature or Q or U is shown on top and bottom in a black and white color scale. The modes on top and bottom have the same spatial period but a different orientation relative to the scan direction. The telescope scan direction is indicated with a red arrow. A mode at a given spatial scale ℓ maps to a maximum frequency in the bolometer TOD when the phase fronts of the mode are oriented perpendicular to the scan direction (top). Modes with an identical spatial period but non-perpendicular orientation map to lower frequencies in the TOD (bottom).

If we focus on phase fronts oriented perpendicular to the scan direction, then we are interested in frequencies between 1.1 Hz and 4.7 Hz, and non-perpendicular phase fronts will map to arbitrarily low frequencies. We are then left with a choice of what band of frequencies to calculate the noise over. The choice that was made early in the analysis process was to use the band of frequencies from 1-3 Hz, which we refer to as the "science band." The mean of the PSD for the sum and difference TOD over this 1-3 Hz band are stored and used as an estimate for the intensity and polarization noise variance for each pixel over the CES. Data weights for the intensity and polarization data during co-addition are chosen as the inverse of the variance calculated here. An example PSD of sum and difference TOD is plotted in figure 4.2.

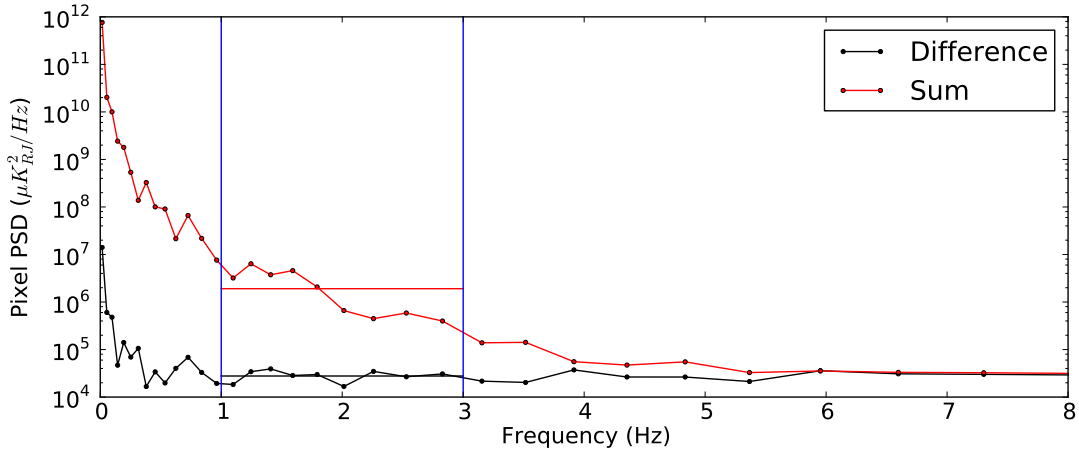

Figure 4.2: The sum and difference PSD are plotted for one pixel over a CES. The science band is indicated with vertical blue lines, and the means of the sum and difference PSDs over the science band are plotted as horizontal lines matching the color of the respective data. The excess low-frequency noise is clearly visible.

The choice of a single value to represent the noise in the TOD corresponds to assuming the noise is white when weighting the data. As a choice to represent this white noise level, the average over the 1-3 Hz science band is clearly not unique and is actually not optimal, particularly for the sum TOD. Extending the lower edge of the science band down to 0.25 Hz improves the noise in the final estimate of the temperature power spectrum by about 30%, though the impact on the polarization power spectra is at the sub-percent level. The final noise estimate

improves because this different choice of science band results in a more optimal weighting of the data. Because we are primarily concerned with polarization noise and because a great deal of data validation had already been done when this was discovered, the science band was left with its original bounds.

Figure 4.2 makes it clear that the noise properties of the sum and difference TOD are very different. This is because differencing the two bolometer TOD removes any noise that is common to both detectors, whereas summing the TOD does not. In particular, because the atmosphere is unpolarized the TOD noise due to the atmosphere, largely created by variations in water column density across the sky, is greatly suppressed in the difference TOD. Successfully differencing out the atmospheric noise requires the pixel-pair relative gain to be correct. Thus pixels for which the relative gain is not correct will see increased atmospheric noise and be down-weighted relative to pixels where the relative gain is correct, creating a further suppression of systematic errors associated with incorrect relative gain. It should also be possible to calibrate the relative gain within a pixel by matching the atmospheric noise signal in both bolometers in the pixel. We have experimented with atmospheric based relative gain calibration, though do not use it as our primary calibration technique. We do perform data cuts based on disagreement between atmospheric relative gain calibration and thermal source relative gain calibration as described below.

Finally, it is interesting to note that it is not necessary to employ the assumption of white noise when weighting the data. It would be possible to weight each frequency differently as the inverse of the PSD noise at that frequency, essentially whitening the data before co-adding different pixels. This technique corresponds to an ideal weighting of the data and could be used to further reduce the noise in our data. This procedure would introduce significant changes to later steps of the data processing and so it remains a project for future improvement of the pipeline.

4.4 Data Selection

Not all of the data POLARBEAR records during CMB scans is useable. We are only able to use data from pixels for which we have successful calibrations, such as a known polarization orientation angle and gains. Additionally, for our first science publications we have elected to only include data where the telescope is moving at a constant velocity. This is a conservative choice motivated by the desire to avoid the noise associated with extra vibrations or cable connector strain during acceleration. Data acquired at different velocities also breaks the assumptions employed above about which time domain frequencies contain information about a particular ℓ range on the sky. We thus discard data from the "turnarounds" as the telescope is changing scan direction. We define an individual constant velocity portion of our scan to be a "subscan," which can either be positive-going (azimuth value is increasing) or negative going (azimuth value is decreasing). Rejection of the accelerating portions of our scans results in a loss of 35.7% of our CES data.

We also attempt to exclude data from our analysis where the instrument was not functioning properly. This selection process can exclude focal plane pixels from ever being included, entire days or individual CESs from being processed, remove single pixel-pairs from a given CES, or remove individual subscans for one pixel-pair, depending on the type of problem.

4.4.1 Primary Data Selection Criteria

We describe our primary selection criteria here, and then quantify the impact of each cut below. Primary cuts are those which remove large sections of data such as pixels from a CES or entire CESs. We will describe criteria that remove individual subscans in the following section.

Some of the cuts we describe use statistics derived from the gains and PSD values of the detectors. It is useful to introduce a new gain value $g_{\rm frac}$ which quantifies the differential gain in a particular pixel during a particular scan. This quantity is not used for calibration but is a useful statistic for tracking the behavior of pixels. We let:

$$g^{j}_{\mathrm{frac}}(t) = \frac{g^{j,t}_{\frac{\mathrm{ADC}}{\mathrm{T_{RJ}}}}(t) - g^{j,b}_{\frac{\mathrm{ADC}}{\mathrm{T_{RJ}}}}(t)}{g^{j,t}_{\frac{\mathrm{ADC}}{\mathrm{T_{RJ}}}}(t) + g^{j,b}_{\frac{\mathrm{ADC}}{\mathrm{T_{RJ}}}}(t)}. \tag{4.2}$$

g_{frac} is thus the fractional difference in gain values between the top and bottom bolometers. It is computed as a function of time for a pair of bolometers in a focal plane pixel j over a particular CES.

RA12 Elevation Range Cut: We exclude data on the sky patch RA12 that was taken between the ranges of 65°- 70° in elevation. This data was identified as problematic during systematic error checks. We believe this is related to mechanical resonances in the telescope structure that are known to occur in this elevation range, but it is unclear why other patches are not affected.

Moon Proximity Cut: We exclude CESs where the center of the scan is within 20° of the Moon due to concern over sidelobes.

Sun Proximity Cut: We exclude CESs where the center of the scan is within 30° degrees of the Sun due to concern over sidelobes and thermal deformation of the primary reflector.

Scan Length Cut: Some CESs were affected by hardware or software problems that caused them to end too soon or continue for too long. These CESs are excluded.

PWV Cut: We exclude data where the precipitable water vapor was measured to be higher than 4 mm.

Encoder Malfunction Cut: There were intermittent malfunctions with our azimuth encoder. The root cause of these malfunctions is still being investigated, however the symptom is that the reported position can fail to update for a variable interval of time. Fortunately this malfunction is rare. We exclude CESs where on average more than one encoder sample per subscan recorded no telescope motion.

Array Median Gain Cut: We exclude CESs where the median gain across the entire focal plane is not between 100 and 305 ADC / $\mathrm{K_{CMB}}$.

Array Median Gain Derivative Cut: We exclude CESs where the median gain of all detectors on the focal plane is changing faster than 20% per hour.

g_{frac} Outlier Cut: We compute the interquartile range (IQR) for all values of g^{j}_{frac} for a particular pixel j over all the CESs where j was successfully gain calibrated.

We then exclude j from CESs where $g^j_{\rm frac}$ exceeds five times its IQR.

$g_{\rm frac}$ *Variance Cut:* We consider the set of IQRs for $g_{\rm frac}$ calculated for each pixel as described above. We then exclude a pixel j from all of our data when $\mathrm{IQR}(g^j_{\rm frac}) > 0.04$. This choice was motivated by desire to cut the extreme tail of the distribution of all pixel IQRs.

$g_{\rm frac}$ *Median Cut:* For each pixel we compute the median value of $g_{\rm frac}$ for all CESs where the pixel was gain calibrated. We then exclude the pixel from all of our data when this median value $m_{g_{\rm frac}}$ is outside of the range -0.2 $< m_{g_{\rm frac}} <$ 0.2.

$g_{\rm frac}$ *Derivative Cut:* We exclude a pixel j from a CES if $g^j_{\rm frac}$ changes by more than 10% per hour over the CES.

Bolometer Mean Gain Cut: Pixels are removed from a CES if either of the bolometers in them have a gain that is not in the range 20 to 2000 in units of ADC / $\mathrm{K_{RJ}}$.

Bolometer Gain Derivative Cut: Pixels are removed from a CES if either bolometer in them is changing gain at an hourly rate that is 20% different than the median hourly rate over all active bolometers for the CES.

Atmospheric Relative Gain Mismatch Cut: For each pixel we fit a relative gain value between the bolometers by matching the level of atmospheric fluctuations in their TOD. These fits are usually in good agreement with the thermal source derived values. We remove data where the atmospheric gain fit reports the ratios of the gains to be either infinite or zero.

Difference PSD Upper Bound Cut: If the variance found using the difference PSD for a pixel over the 1-3 Hz science band is larger than three times the median value over a CES, the pixel is removed from the CES.

Difference PSD Lower Bound Cut: If the variance found using the difference PSD for a pixel over the 1-3 Hz science band implies an NET less than 260 $\mu\mathrm{K}/\sqrt{\mathrm{Hz}}$ the pixel is excluded from the CES. Values below this are considered un-physically low.

Ground Template Cut: Before map making, our data is filtered in several different ways which will be described below. One of these filters is called the "ground template" filter; see section 4.5.1 for more description. We pre-compute the TOD

variance before and after applying this filter and identify the upper quartile value (above 75% of the data) of this difference. We then exclude pixels from a CES that are four times higher than this upper-quartile value.

Bad Pixel Cut: We remove five pixels from our data set due to large errors on the gain model fits.

Yield Cut: After all other exclusion criteria have been applied, we exclude CESs where there are not at least 50 focal plane pixels active. This is designed to ensure that all of the maps we make have good scan coverage.

In order to quantify the impact each criteria has on our data set we compute what fraction of our data it removes. This fraction is computed relative to all data for which we generate a gain. Instead of just computing this value in terms of bolometer-hours, we choose to do it in terms of polarization data weight. As discussed above, polarization data from a given pixel is weighted by the inverse variance of its difference TOD from 1-3 Hz. We compute the total weight for each pixel-CES as the product of the inverse variance times the duration of the CES. We use the sum over this product for all pixels and all CESs with gains generated, and take that to be the total data weight. We then compute the fraction of weight that each criteria removes. It is possible to characterize both the total fraction of weight a particular criteria removes from the data set and also the "orthogonal" fraction of data removed by a particular criteria, which we define as the fraction of data excluded by a particular criteria that is not also removed by another. These values are shown in table 4.1.

The total fraction of data removed by weight is 28.46%, or 40.44% in terms of pixel-hours, and 40.72% in terms of pixel-CESs. In total we retain 8,354 CESs across the three patches, with a median number of active pixels of 301.

4.4.2 Subscan Removal Criteria

Another set of cut criteria we implement remove individual subscans from pixel TODs. These are largely designed to find and remove "glitches" such as large spikes or other non-Gaussian features in the TOD, but also remove data when there was a problem with the instrument that affected a time period less than a

Table 4.1: Impact of POLARBEAR data selection criteria. The fraction and orthogonal fraction of data weight removed by each selection criteria is listed, along with the total weight removed by any cut.

Cut Name	**Cut %**	**Orthogonal Cut %**
RA12 Elevation Range Cut	7.24%	4.99%
Moon Proximity Cut	3.80%	2.37%
Sun Proximity Cut	2.23%	1.24%
Scan Length Cut	0.02%	0.00%
PWV Cut	3.43%	1.60%
Encoder Malfunction Cut	1.56%	0.67%
Array Median Gain Cut	1.71%	0.60%
Array Median Gain Derivative Cut	1.05%	0.21%
g_{frac} Outlier Cut	2.53%	1.14%
g_{frac} Variance Cut	1.20%	0.64%
g_{frac} Median Cut	0.68%	0.46%
g_{frac} Derivative Cut	0.38%	0.01%
Bolometer Mean Gain Cut	0.00%	0.00%
Bolometer Gain Derivative Cut	1.66%	0.54%
Atmospheric Relative Gain Mismatch Cut	0.69%	0.37%
Difference PSD Upper Bound Cut	1.67%	0.48%
Difference PSD Lower Bound Cut	0.52%	0.34%
Ground Template Cut	8.44%	4.46%
Bad Pixel Cut	0.33%	0.05%
Yield Cut	17.37%	0.14%
Total	28.46%	-

full CES.

We have three primary interests in establishing the subscan removal criteria: eliminating obviously bad data where the instrument was malfunctioning, preventing systematic contamination of our results, and reducing our error bars by the removal of non-Gaussian noise (the technique we use to calculate our error bars is discussed in section 4.6.5). We discuss our subscan removal criteria individually here.

RPS Signal Loss: There are brief periods of time where we fail to receive the RPS signal (see section 2.2.4), which results in a loss of pointing information. This pointing data is nominally interpolated and likely useable for brief periods, but we remove subscans where there was any loss of the RPS signal.

UDP Packet Loss: As described in section 2.8, all of our bolometer data is received over Ethernet using the UDP protocol, which does not guarantee packet delivery. We thus occasionally experience dropouts in bolometer data from parts of the focal plane. This data loss can be interpolated, and we set the requirement that no more than 10% of data from a subscan be lost. In practice this data loss is quite rare.

Servo Malfunction: We record both the commanded position of the telescope and the encoder reported position at each pointing sample. We do not expect perfect agreement between these, but if the telescope control system is malfunctioning this difference will increase. Disagreement between the commanded and actual positions will also increase when the grease in the speed reducer connecting the servo motor to the friction drive is too cold and becomes unacceptably viscous. In this condition the telescope is unable to meet its acceleration and velocity specifications, which results in the telescope being unable to execute our desired scan pattern. We remove subscans where the difference between any measurement of the commanded and actual azimuth position is larger than 0.5°.

Anisotropic Scan Noise: The telescope has certain mechanical resonances that lead to excess glitches in our data. While not always present, these resonances are largely elevation and scan speed dependent when they do occur. It has also been observed that they preferentially create noise in a particular scan direction. We thus compute the standard deviation of the difference TOD of all negative going (σ_{neg}) going and positive going (σ_{pos}) subscans independently. We then require that:

$$\frac{\sigma_{pos} - \sigma_{neg}}{\sigma_{pos} + \sigma_{neg}} < 0.23 \tag{4.3}$$

or we remove that pixel from the CES. This criteria removes about 2.5% of our data but is found to reduce our errors bars, though only at the sub-percent level.

Glitch Identification: To locate individual glitches in our TOD, we convolve each difference TOD with a set of kernels which are sensitive to different shapes or frequencies of glitches. Each kernel has a center based on a Lorentzian of different widths, with flat "wings" added at negative values to give each kernel zero net area. The central Lorentzian shape was motivated by matching the shape of glitches

located by eye in the TOD. The zero area criteria ensures the kernels have no response at zero frequency. These kernels and their frequency responses are shown in figure 4.3.

Each kernel is convolved with the difference TOD of a pixel over a full CES. We calculate the MAD (see equation 3.25) of each convolved TOD. We then remove subscans where the absolute value of the TOD of any of the convolutions exceeds 6.8 times its MAD. The choice of this criteria is driven by the competing requirements of aggressively removing glitches while not removing data that is consistent with Gaussian noise. These criteria are tuned such that we remove about 0.25% of subscans in white noise simulations and 1.4% of subscans from our real data. There was concern that criteria which removed more Gaussian noise could bias our signal, but this level was deemed acceptable. Implementing these convolution based subscan removal criteria reduces our C_ℓ^{BB} error bars by more than one percent relative to no glitch flagging. We interpret this result to mean that the data we removed was mis-weighted.

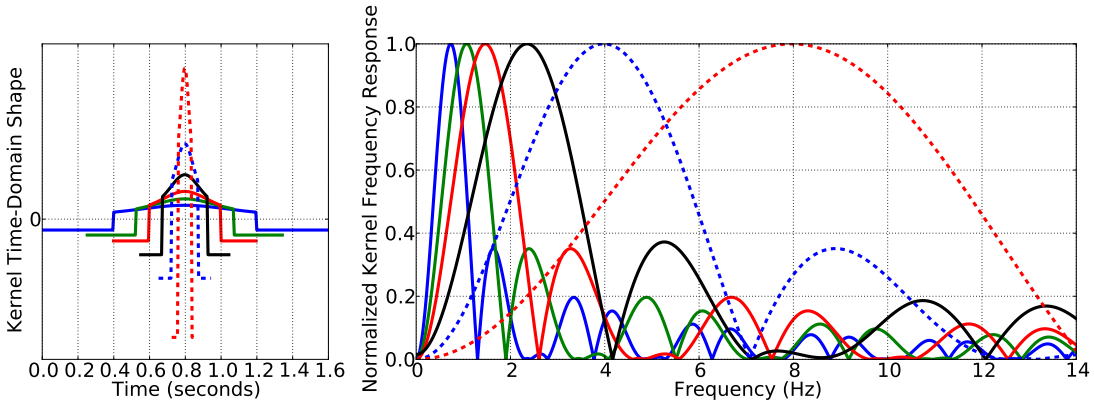

Figure 4.3: The set of six kernels used for TOD glitch finding are shown in the time (left) and frequency (right) domains. The frequency response is shown as the magnitude of the Fourier transform of the kernels. The kernels are zero-padded to the length of a CES before being Fourier transformed.

Cut Fraction: After all these subscan removal criteria described above have been applied, we ensure that not more than 30% of subscans have been removed for any of the active pixels during a CES. We consider pixels above this threshold to be suspicious, and remove all the data from these pixels over the CES.

Combining all of our criteria, we remove a total of 4.3% of our subscans while reducing our error bars at about the half-percent level. There is some elevation dependence to this removal, which is demonstrated in figure 4.4. The elevation dependence is likely due to changes in mechanical resonances and bearing scan speed as the observation elevation changes.

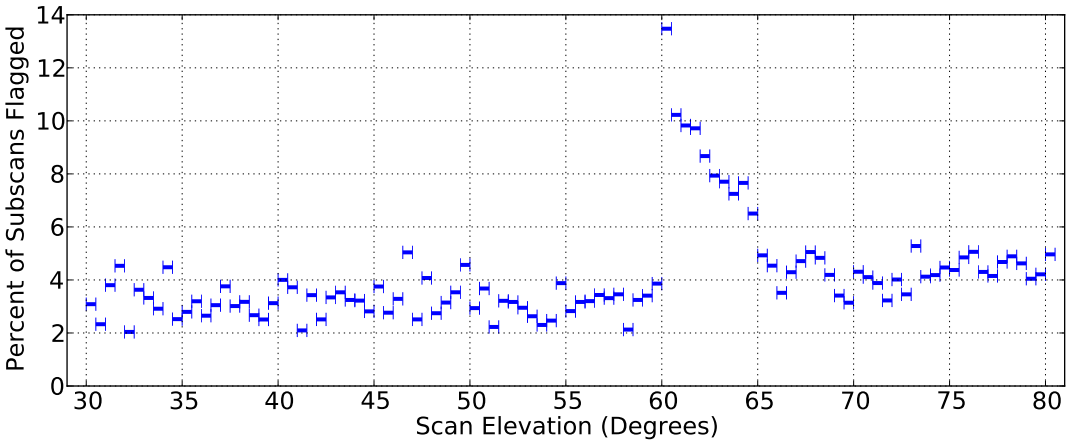

Figure 4.4: The percent of subscans removed by all flagging criteria are shown as a function of elevation. The overall fraction of subscans removed across all elevations is 4.3%.

Additionally, we investigated several other subscan removal criteria designed to search for what we refer to as "time-dependent scan-synchronous signals." A scan-synchronous signal is a signal which occurs in-phase with the telescope scan motion. These signals occur at the same azimuth location every time the telescope completes a subscan. Because the sky is drifting relative to the ground, this does not correspond to most legitimate signals received from the sky. We will see in the description of our TOD filtering below in section 4.5.1 that we remove scan-synchronous signals that occur at identical amplitudes in every subscan, but signals which occur at different amplitudes at the same point in every subscan are not completely removed. We refer to these as time-dependent scan-synchronous signals because their amplitude varies as a function of time but they still create a signal at the same fixed point in each subscan. However, if these signals do not also

occur at the same RA/DEC coordinates between different days they should only contribute noise and not actually bias our measurement of C_ℓ^{BB}. To investigate the impact of these signals, we developed several criteria based on the co-addition of the square of each subscan TOD and on the correlations of different subscan TOD across a CES which were successful in identifying and removing signals which we judged by eye to be time-dependent and scan-synchronous. They also removed many possibly false-positive signals which we did not judge to be scan-synchronous by eye. We then performed white noise simulations which involved scanning 100 different realizations of a simulated CMB sky with our real telescope pointing, adding white noise to each TOD in the amount calculated via the average PSD over the science band as described above. We performed these simulations on the same realizations of signal and noise with and without removing the set of subscans which were flagged by our time-dependent scan-synchronous signal criteria as applied to the real data. We used these simulations to compare the impact on C_ℓ^{BB} from removing the time-dependent scan-synchronous signals we identified in our real data with removing the same amount of data from white noise simulations without any scan-synchronous signals. We found that the change in C_ℓ^{BB} in the real data was consistent with removing the same amount of data from white noise simulations with a minimum PTE of 56%. In the absence of any evidence that our time-dependent scan-synchronous signals were occurring at the same RA/DEC coordinates between different days and with these simulations failing to indicate the removal of any systematic bias, we were not strongly motivated to implement these criteria. Furthermore, the removal of data associated with these criteria increased our error bars on C_ℓ^{BB} by more than 12%, and so without any evidence that they were useful for removing a systematic bias we elected to not implement these cuts in our final data removal criteria.

Overall, we believe our data selection criteria are conservative. We largely adopted a "when in doubt, cut it" philosophy for our first season of data, particularly with regard to our primary cutting criteria (those in table 4.1). It is likely that several of these criteria could be relaxed without contaminating our results, which would allow some data to be recovered. This will be explored in the future.

4.5 Filtering and Map Making

Our CMB maps are formed from our TOD using a procedure that is fairly standard in the field [59, 65]. It is frequently expressed as:

$$\boldsymbol{m} = \left(\boldsymbol{A}^T \boldsymbol{N}^{-1} \boldsymbol{A}\right)^{-1} \boldsymbol{A}^T \boldsymbol{N}^{-1} \boldsymbol{F} \boldsymbol{d} \tag{4.4}$$

which corresponds to minimizing the residual noise in the map under the assumption that the noise is white. This expression simultaneously succeeds at masking the complexity of some parts of the operation while also obfuscating the obvious. We will describe the procedure step-by-step here. On the right hand side of equation 4.4, $\boldsymbol{d}$ is a vector of our bolometer TOD, $\boldsymbol{F}$ represents a series of filters we apply to the TOD, $\boldsymbol{N}^{-1}$ represents our inverse variance noise weighting for each TOD sample, and $\boldsymbol{A^T}$ and $\boldsymbol{A}$ are objects called the pointing matrix and its transpose. $\boldsymbol{A}$ and $\boldsymbol{A}^T$ represent a way to use our telescope pointing data to inter-convert between a given time sample in the bolometer TOD and a map pixel in the sky map we are constructing (this will be described in more detail below). On the left hand side, $\boldsymbol{m}$ represents our map. The map is pixelated at two square arcminutes, below the actual resolution of the instrument, and uses the equal area projection described in [66] centered at the center of each of the three patches we scan. We approximate each patch as flat.

In words, the part of the equation that reads $\boldsymbol{A}^T \boldsymbol{N}^{-1} \boldsymbol{F} \boldsymbol{d}$ can be described as taking our detector TOD $\boldsymbol{d}$, filtering it in some way represented by $\boldsymbol{F}$, multiplying each time sample by its weight from $\boldsymbol{N}^{-1}$, and then projecting each sample onto an object representing our sky map at some particular map pixel using $\boldsymbol{A}^T$. The portion of the procedure that reads $\left(\boldsymbol{A}^T \boldsymbol{N}^{-1} \boldsymbol{A}\right)^{-1}$ can be interpreted as dividing each pixel in our map by the sum of the weights from $\boldsymbol{N}^{-1}$, as in a normal weighted averaging operation. We then finally arrive at the estimate of the sky map $\boldsymbol{m}$. This description hides some difficulty in creating two separate maps of polarization (one for Q and one for U) from the TOD, but is a good mental picture to have in mind.

It is worth noting that the filtering operation represented by $\boldsymbol{F}$ can also be interpreted as a different kind of weighting operation that is not associated with $\boldsymbol{N}^{-1}$. Our filtering attempts to project out parts of our TOD that have

a particularly low signal-to-noise ratio. The filtering removes signal and noise from any part of the TOD it projects out. The filtering corresponds to removing power from Fourier modes that make up our map, and this removal of power is anisotropic in the sense that some Fourier modes are affected more than others. While the bias introduced by weighting each mode in the map by $\boldsymbol{N}^{-1}$ is removed via $\left(\boldsymbol{A}^T\boldsymbol{N}^{-1}\boldsymbol{A}\right)^{-1}$, there is no similar operation at the map level to remove the bias introduced by the filtering. We are thus left with a *biased* estimate of the sky map, meaning that not all Fourier modes that make up the map are equally represented. Thus we cannot claim the maps we produce are accurate representations of the true sky. This bias is corrected later when the power spectrum is estimated so that we do make an unbiased estimate of the power spectrum.

4.5.1 Filtering

A series of three filters are applied to our TOD before they are mapped. These filters remove high frequencies, low-order polynomials per each subscan, and scan-synchronous signals.

Low-Pass Filtering

High frequencies are removed with a low-pass filter with a frequency profile:

$$F(f) = e^{-\log(\sqrt{2})\left(\frac{f}{f_{\mathrm{lpf}}}\right)^6}, \tag{4.5}$$

where $f_{\mathrm{lpf}} = 6.3$ Hz. Because projecting our TOD onto map pixels of a finite size represents a form of down-sampling, we first impose this low-pass filter to prevent aliasing higher frequencies from the TOD into the map domain. The full-season effect of the low-pass filtering is isotropic with respect to the azimuthal angle $\varphi_{\vec{\ell}}$ in Fourier space.

Polynomial Filtering

We subtract a Legendre polynomial from each subscan TOD to remove excess low frequency noise. A first order polynomial is fit and removed from the

difference TOD, while a third order is fit and removed from the sum TOD. The point sources in each sky patch are masked in the TOD and excluded from the polynomial fits to avoid spreading their power across the domain of the polynomial being subtracted. Figure 4.5 shows an example of the effects of the polynomial filtering over a full season of data. The effect is not isotropic with respect to the Fourier plane azimuthal angle $\varphi_{\vec{\ell}}$.

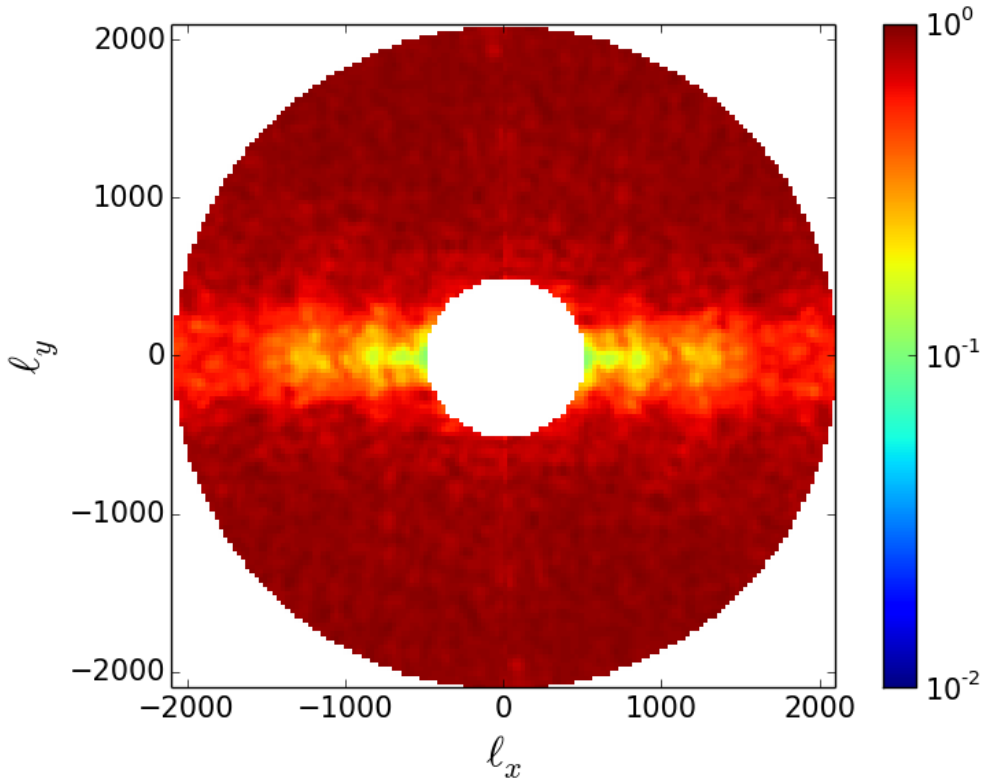

Figure 4.5: The anisotropic effect of polynomial filtering on BB is shown in 2D Fourier space for the sky patch RA23 for the entire season of data. The factor by which BB noise and signal are suppressed due to the polynomial filtering is plotted on a log color scale. Only the region from $500 < \ell < 2100$ is shown; the rest of Fourier space is masked out.

Ground Template Filtering

Our most complicated filter is the one designed to remove scan-synchronous signals. We refer to this filter as a "ground-template" filter because it removes sig-

nals which are fixed in azimuth and elevation space, as any stray light inadvertently scattered in from the ground would be. This filter makes use of our scan strategy which fixes the telescope at one elevation and scans over the same range of azimuth angles for fixed periods of time as discussed in section 2.2.3. After applying the low-pass and polynomial filters, we bin the TOD of a pixel from each subscan into azimuth bins that are 0.08° in width. We then create an average value in every bin over the full CES, and this average is referred to as the ground template for that CES. We then subtract the ground template from each subscan TOD to form a TOD free of average ground pickup.

Because of our use of RA/DEC coordinates for map making, the ground template filter has a very specific impact on certain Fourier modes in our maps. This effect is exploited by other groups [67] as an alternative method of filtering out ground signals, though without explanation. In fact, this effect does not appear to be well documented nor widely understood, so we explain it here. As discussed in section 2.2.3, our CES scans rely on sky drift to sample different parts of our sky patches. If we allow $\hat{\boldsymbol{RA}}$ and $\hat{\boldsymbol{DEC}}$ to be our basis vectors for the RA/DEC coordinate system, then sky drift corresponds to motion in the $\hat{\boldsymbol{RA}}$ direction. Most Fourier modes will change their phase relative to our scan pattern as the RA coordinate advances during the scan. Because the phases of these modes change, they do not add signal coherently in the same azimuth bin across the CES and are thus not captured by the ground template. However, modes with their wave vector oriented perpendicular to $\hat{\boldsymbol{RA}}$ remain at a fixed phase relative to the scan pattern and are thus removed by the ground template. This is demonstrated in figure 4.6.

Because the sky always drifts in the $\hat{\boldsymbol{RA}}$ direction, the same Fourier modes are removed by the ground template filter during every CES we perform. The ground template filter thus represents our largest source of anisotropic bias in the co-added maps we make. However, the removed modes correspond to a small fraction of the modes we sample.

An example application of the ground template filtering is shown in figure 4.7. The vertical band representing modes with phase fronts parallel to $\hat{\boldsymbol{RA}}$ is

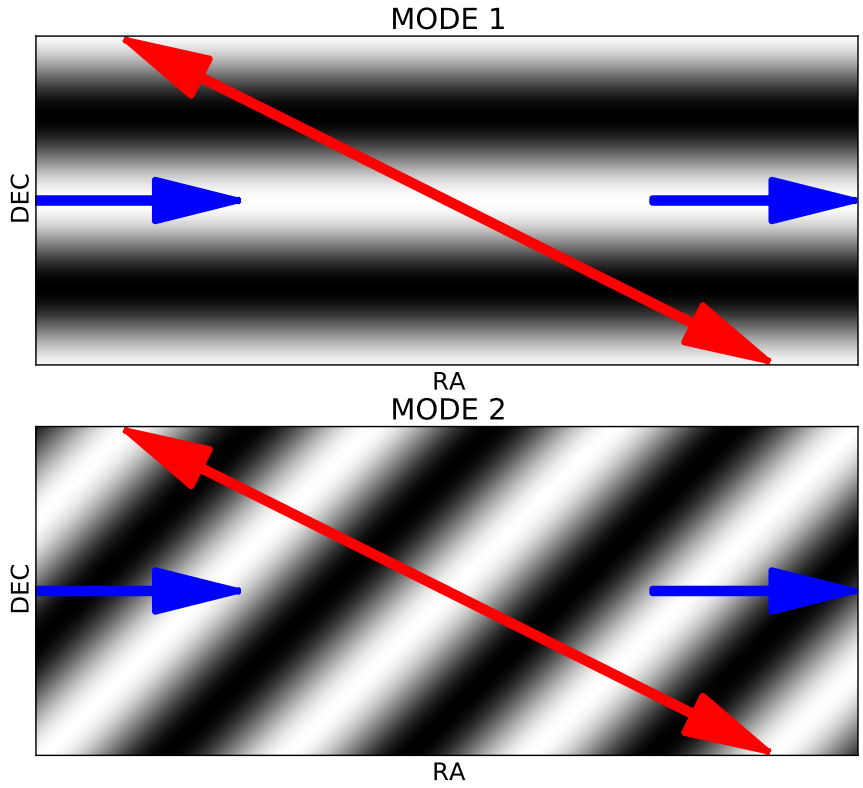

Figure 4.6: Fourier modes of either the Stokes I, Q, or U parameters are shown on a sky projection at the same spatial scale ℓ for two different orientations (MODE 1 and MODE 2). The telescope scan pattern over the CES is represented by the red arrows, and the direction of the sky drift is represented by the blue arrows. The scan direction is along a line of constant elevation, which is generally not aligned with RA or DEC. Sky drift corresponds to translating the RA coordinate relative to the scan pattern. Modes with their wave vector perpendicular to the RA direction (MODE 1) do not change phase relative to the scan pattern as the sky drifts and are thus removed by the ground template filtering. Modes with their wave vectors oriented in another direction (MODE 2) do change phase relative to the scan pattern as the sky drifts and are not removed.

clearly visible in the BB suppression ratio.

4.5.2 Pointing Matrix and Data Models

The pointing matrix $\boldsymbol{A}^T$ is a matrix assembled using the pointing TOD generated by the procedure in section 3.3. For the sum TOD, the pointing matrix converts between samples in the time domain indexed by t and the corresponding

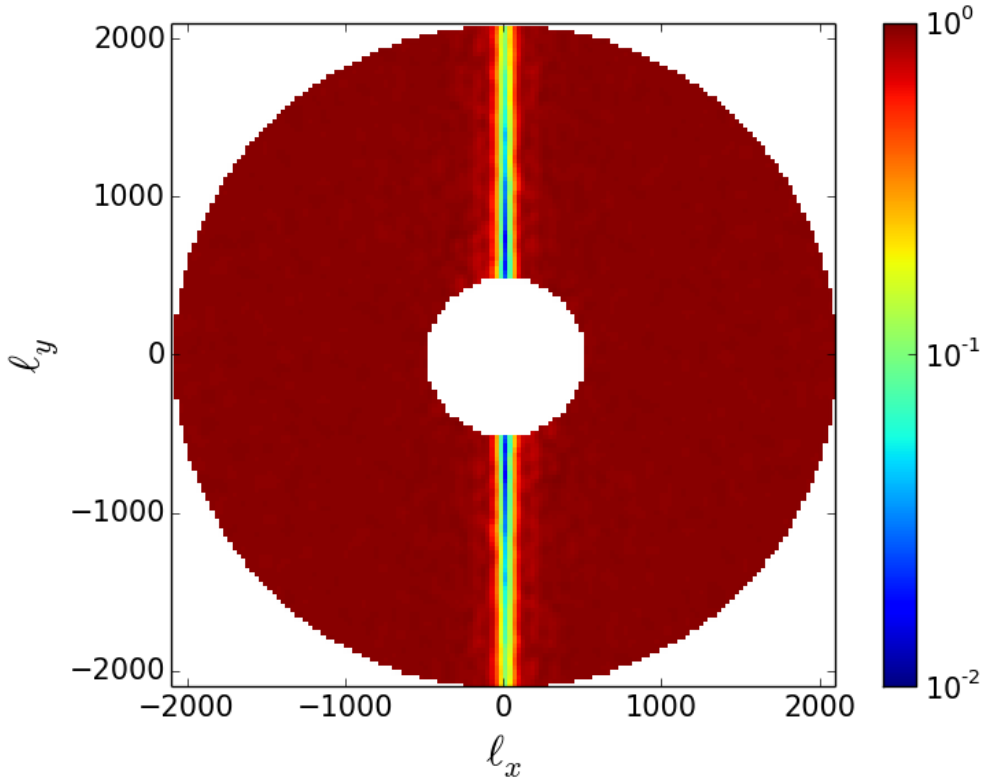

Figure 4.7: The anisotropic effect of ground template filtering on BB is shown in 2D Fourier space for the sky patch RA23 for the entire season of data. The factor by which BB noise and signal are suppressed due to the ground template removal is plotted on a log color scale. Only the region from $500 < \ell < 2100$ is shown; the rest of Fourier space is masked out.

map pixels on the sky indexed by p. The transpose of the pointing matrix $\boldsymbol{A}$ will project map pixels into the TOD. We may model this behavior as:

$$d_t^{\text{sum}} = \boldsymbol{A}_{tp} I_p + n_t^{\text{sum}}, \tag{4.6}$$

where d_t^{sum} represents our sum TOD, I_p represents the Stokes intensity parameter I at a given map pixel p, and n_t^{sum} represents the noise in the sum TOD. For the difference TOD, the same operation is modeled as:

$$d_t^{\text{diff}} = \boldsymbol{A}_{tp} \cos(2\Theta_t) Q_p + \boldsymbol{A}_{tp} \sin(2\Theta_t) U_p + n_t^{\text{diff}}, \tag{4.7}$$

where Q_p and U_p are the Stokes Q and U parameters at a given sky pixel p, Θ_t

is the polarization orientation angle defined in equation 3.30 of the detector in question at a given time index t, and n_t^{diff} is the noise in the difference TOD.

4.5.3 Solving for Maps

Constructing the Stokes intensity map is exactly as simple as our original naive reading of equation 4.4 lead us to believe. We bin our filtered, weighted TOD into map pixels and then divide by the sum of the weights.

Equation 4.7 makes it clear that the case of the polarization data is more complicated. The problem is that we are not simply making one map of polarization but two maps representing the Stokes Q and U parameters. We must specify how a TOD from a particular pixel contributes to either Q or U.

We allow $\boldsymbol{A}^T$ to become a coupling matrix such that it will project d_t^{diff} into two different maps with two different weightings. $\boldsymbol{A}^T$ must now couple $\cos(2\Theta_t)\boldsymbol{N_t}^{-1}\boldsymbol{d_t}$ into the appropriate Q pixel Q_p and $\sin(2\Theta_t)\boldsymbol{N_t}^{-1}\boldsymbol{d_t}$ into the appropriate U pixel U_p.

Considering 4.7 with the weighting $\cos(2\Theta_t)$ for Q and $\sin(2\Theta_t)$ for U, the weights W accumulate for a given map pixel Q_p or U_p as:

$$\begin{aligned} W_{Q_p} &= \sum_t N_t^{-1}[\boldsymbol{A}_{tp}\cos^2(2\Theta_t) + \boldsymbol{A}_{tp}\sin(2\Theta_t)\cos(2\Theta_t)] \\ W_{U_p} &= \sum_t N_t^{-1}[\boldsymbol{A}_{tp}\sin^2(2\Theta_t) + \boldsymbol{A}_{tp}\cos(2\Theta_t)\sin(2\Theta_t)] \end{aligned} \tag{4.8}$$

$\boldsymbol{A}^T\boldsymbol{N^{-1}}\boldsymbol{A}$ can then be written for each map pixel as:

$$\tilde{\boldsymbol{C}} = \boldsymbol{A}^T\boldsymbol{N^{-1}}\boldsymbol{A} = \begin{pmatrix} n_{cc} & n_{cs} \\ n_{cs} & n_{ss} \end{pmatrix} \tag{4.9}$$

with:

$$\begin{aligned} n_{cc} &= \sum_t N_t^{-1}\cos^2(2\Theta_t) \\ n_{ss} &= \sum_t N_t^{-1}\sin^2(2\Theta_t) \\ n_{cs} &= \sum_t N_t^{-1}\cos(2\Theta_t)\sin(2\Theta_t) \end{aligned} \tag{4.10}$$

where the sums run over all time samples at a given map pixel.

The last step required to construct our map $\boldsymbol{m} = \begin{pmatrix} \boldsymbol{Q} \\ \boldsymbol{U} \end{pmatrix}$ is to invert $\tilde{\boldsymbol{C}}$ to form $\left(\boldsymbol{A}^T \boldsymbol{N}^{-1} \boldsymbol{A}\right)^{-1}$. It is clear from equation 4.7 that measuring each sky pixel at only one value of polarization angle Θ_t measures a linear combination of Q and U, but is insufficient to reconstruct either Q or U. In general, having insufficient information to reconstruct both Q and U corresponds to $\tilde{\boldsymbol{C}}$ being singular. Measuring each map pixel from many different detector polarization angles ensures that this does not happen. Having more angular coverage (measurements at many values of Θ_t) also helps to evenly distribute noise in Q and U, and is useful for suppressing other systematic errors [46].

4.5.4 Co-added Maps

We form an individual map from every CES we include in our final data set. These can then be co-added to form a map of the entire season's observations. An example of a full season co-added map for a single patch is shown in figure 4.8.

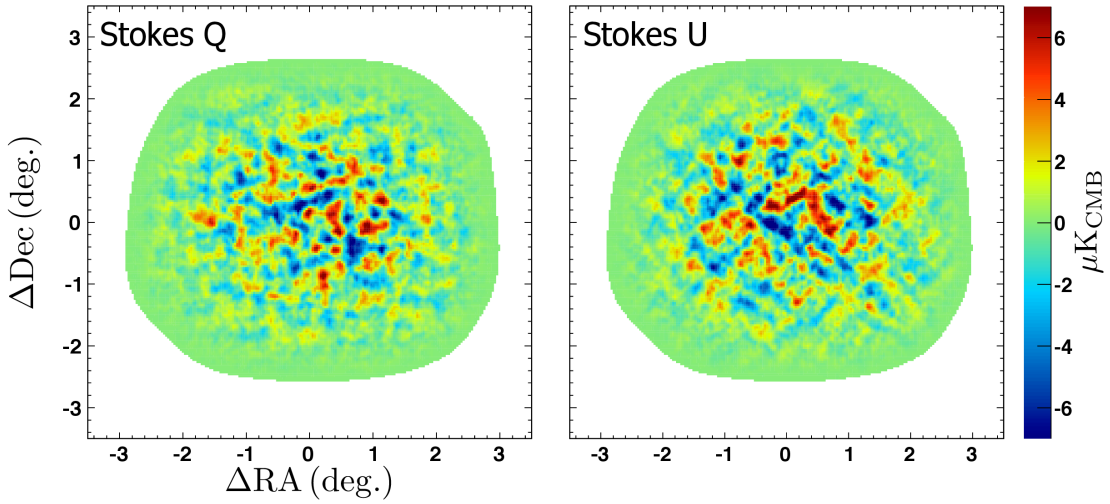

Figure 4.8: Co-added Q and U maps for the sky patch RA23 shown with the apodization described in section 4.6.1 applied. Figure from [43].

It is at this point in the pipeline that the C_ℓ^{BB} and other power spectra analyses diverge from the C_L^{dd} pipeline. The three full season co-added maps are

the inputs to the C_L^{dd} pipeline described briefly in section 4.9. For the C_ℓ^{BB} measurements, we form a daily map for every day we observed each patch during the season. The patches RA4.5, RA12, and RA23 have 148, 139, and 189 daily maps respectively.

4.6 Power Spectrum Estimation

We will describe here the major components of the C_ℓ^{BB} analysis pipeline, which largely follows the Monte Carlo Apodized Spherical Transform Estimator (MASTER) procedure outlined in [68]. We modify the estimator slightly by only using cross-spectra between maps obtained from different days, as described in [69, 70].

The MASTER technique is primarily used to account for the fact that we are attempting to measure power spectra, defined for the full sky, when we do not have a measurement of the full sky. It also accounts for the anisotropy in the maps created by filtering and for the finite angular resolution of the beam. For a given full sky spectra specified by its ensemble average $\langle C_\ell \rangle$, where the averaging is taken to occur over many realizations of the sky, MASTER models the procedure as:

$$\begin{aligned} \langle \tilde{D}_\ell \rangle &= \sum_{\ell'} K_{\ell\ell'} \langle D_{\ell'} \rangle + \langle \tilde{N}_\ell \rangle \\ K_{\ell\ell'} &= M_{\ell\ell'} F_{\ell'} B_{\ell'}^2 \end{aligned} \tag{4.11}$$

where we have replaced $\langle C_\ell \rangle$ with the flattened spectra $\langle D_\ell \rangle = \frac{\ell(\ell+1)}{2\pi} \langle C_\ell \rangle$ or $\langle \tilde{D}_\ell \rangle = \frac{\ell(\ell+1)}{2\pi} \langle \tilde{C}_\ell \rangle$. $\tilde{D}_\ell$ represents the flattened pseudo-spectra, which is what we will directly measure using our partial sky maps, $M_{\ell\ell'}$ represents the mode coupling matrix, F_ℓ represents the filter transfer function, B_ℓ represents the instrument beam in Fourier space, the measurement of which is described in section 3.4, and $\tilde{N}_\ell$ is the noise bias. The apodization created by our finite patch size (as well as the edge taper we apply to prepare each map, see below) correlates different Fourier modes from the full sky, and this is accounted for via the mode coupling matrix. The filter transfer function F_ℓ accounts for the loss of power in the Fourier modes due to filtering. As described before, the filtering can be de-

scribed as projecting out signal and noise in modes where the signal-to-noise ratio is particularly bad. This corresponds to down-weighting the filtered modes, and the filter transfer function ensures that the overall average is properly normalized.

In the case of POLARBEAR we use only cross-spectra in our estimate of $\langle \tilde{C}_\ell \rangle$. The cross-spectrum estimator is unbiased in the sense that the expectation value of the estimator is equal to our signal $\langle \tilde{C}_\ell \rangle$ [69], and thus we may set $\langle \tilde{N}_\ell \rangle = 0$. Including "auto-spectra," terms by cross-correlating maps from a single day with themselves, as is common in other analyses including the initial description of the MASTER procedure, introduces a noise bias which must be simulated and subtracted. Our use of only cross-spectra avoids this extra complication at the cost of losing the signal in the same-day cross correlations.

4.6.1 Map Preparation

The daily maps described above are the input to the power spectrum estimator. Before the maps can be Fourier transformed to form power spectra, they must be apodized. This apodization de-weights the higher noise map pixels at the edges of the map, and masks point sources. The temperature maps are apodized with an inverse noise variance cutoff at the edges of the map, and with a flat function where the CMB fluctuations are measured with a large signal-to-noise ratio. The Q and U maps are apodized identically to each other using a cutoff on an estimate of the maximum noise between the Q or U maps. Map pixels with an apodization window value below 1% of the peak are set to zero. Point sources in the map are also masked. The apodization edges are modified using the technique described in [71] to minimize E/B leakage. The inverse variance noise estimates for each map pixel are multiplied by the apodization mask and summed over the entire map to produce a single weight value for each map w_i^X, where i indexes the day each map belongs to and with $X \in [T, E, B]$.

4.6.2 2D Fourier Transforms

Once our daily maps are apodized, the next step is to form the 2D Fourier transform of each map. For the temperature spectra, the Fourier transforms of the maps are all we need to perform the correlations that produce the power spectra. For the polarization data we must form E and B from the Fourier transforms of the Q and U maps. E and B can be formed from Q and U in Fourier space using equation 1.19. However, the apodization that is applied to the maps essentially alters the basis over which the Fourier transforms are performed, meaning that the naively applied transform results in ambiguous (non-orthogonal) modes. The basis functions representing individual Fourier modes must be altered to account for this. After using equation 1.19 to form E and B in Fourier space, we correct for the mode-mixing [72] and generate the pure-E and -B 2D Fourier spectra. This procedure leaves us with our Fourier transforms of the daily maps $\tilde{\boldsymbol{m}}_i^X$, where i again indexes the map number and $X \in [T, E, B]$.

4.6.3 Power Pseudo-spectra

For our estimate of the power pseudo-spectrum $\tilde{D}_\ell$, we only want to compare maps from different days with each other. We estimate the pseudo-spectra as a weighted average of the products of maps between different days. The operation is:

$$XY_{\vec{\ell}} = \frac{1}{\sum_{i\neq j} w_i w_j} \sum_{i\neq j} w_i \tilde{\boldsymbol{m}}_i^X w_j \tilde{\boldsymbol{m}}_j^{Y*}, \tag{4.12}$$

where $X, Y \in [T, E, B]$ and i and j index the map number and run over the total number of days we have maps for each sky patch. This gives us an estimate of our 2D Fourier pseudo-spectra excluding the terms where $i = j$. Terms where $i = j$ represent the auto-spectra of daily maps, which we do not want to include. An example is shown in figure 4.9 for $X = Y = B$ (i.e. the 2D BB power pseudo-spectra) for the sky patch RA23.

If figure 4.9 were a true 2D power spectra, each Fourier-space pixel in the image would be independently drawn from a Gaussian random field with a variance

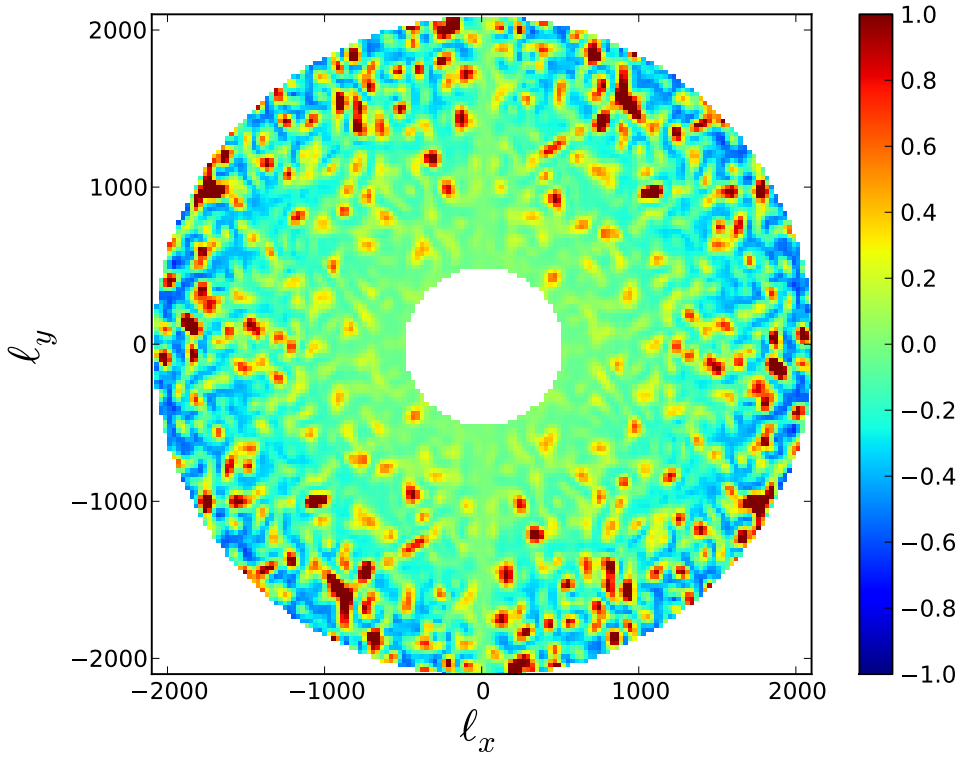

Figure 4.9: The flattened 2D BB Fourier pseudo-spectra for RA23 is shown normalized to the maximum value within $500 < \ell < 1100$ and shown only in the range of $500 < \ell < 2100$. The increasing noise as a function of $|\vec{\ell}|$ is clearly seen. The pixelization that is visible represents the true discretization of the Fourier space data.

equal to C_ℓ^{BB} at $\ell = |\vec{\ell}|$. Instead we see coherent "blobs" in the image that span many pixels. These structures are a result of the mode mixing caused by our finite apodization and represented by $M_{\ell\ell'}$ which must be accounted for in the final power spectrum estimation.

We form 2D estimates of TT, EE, TE, TB, EB, and BB in this way for each sky patch. We then average over radial bins of width $\Delta\ell = 40$ to arrive at high-resolution 1D pseudo-spectra. The narrow bin width and the size of our sky patch means that the signal in each bin is highly correlated with neighboring bins so that they are not independent measurements. An example of this high-resolution 1D pseudo-spectra is shown in figure 4.10 for the same data shown in

figure 4.9

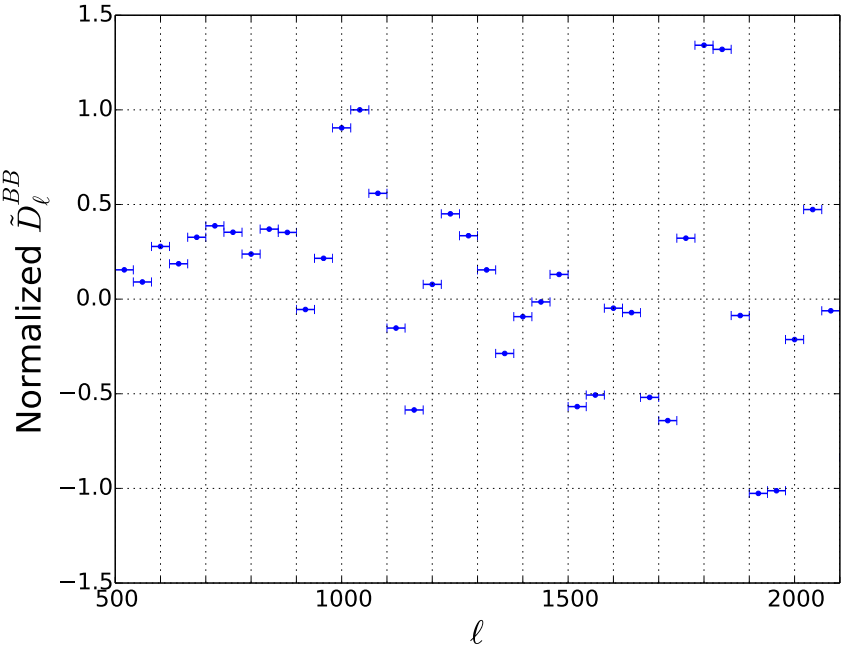

Figure 4.10: The 1D BB high-resolution power pseudo-spectra ($\tilde{C}_\ell^{BB}$) for RA23 over the full first season is shown normalized to the maximum value within $500 < \ell < 1100$ and shown only in the range of $500 < \ell < 2100$. This corresponds to the same normalization and range displayed in figure 4.9. Each point in this figure comes from averaging over an annular ring in figure 4.9 with widths and locations as indicated by the blue bars in this figure.

4.6.4 Power Spectra

We now need to use our estimates of $\tilde{D}_\ell^{XY}$ to estimate the true sky power spectra D_ℓ^{XY}. To do this we need to construct $K_{\ell\ell'} = M_{\ell\ell'} F_{\ell'} B_{\ell'}^2$. The process for estimating B_ℓ is described in section 3.4. The mode coupling matrix $M_{\ell\ell'}$ is calculated analytically from the apodization masks calculated for the full season co-added maps [73]. $M_{\ell\ell'}$ is calculated at the resolution of the psuedo-spectra ($\Delta\ell = 40$).

The filter transfer function F_ℓ is estimated via Monte Carlo simulations. A set of one arcminute resolution maps using Gaussian realizations of the WMAP-9 best fit ΛCDM power spectra [29] are generated. The instrument beam B_ℓ and

pointing TOD of each detector are used to scan these input maps to create simulated TOD. The noise weightings are also used to correctly weight the contribution of each detector. These TOD are filtered, mapped, and processed identically to the real data. The results of these simulations are used to determine F_ℓ given the knowledge of the initial input cosmology. Importantly, the value of the transfer function is not strongly dependent on the input cosmology. Additionally, the polynomial and ground template filtering can create E-to-B leakage. This leakage is assessed using map realizations with only TT and EE or TT and BB and the leakage is subtracted at the pseudo-spectra level.

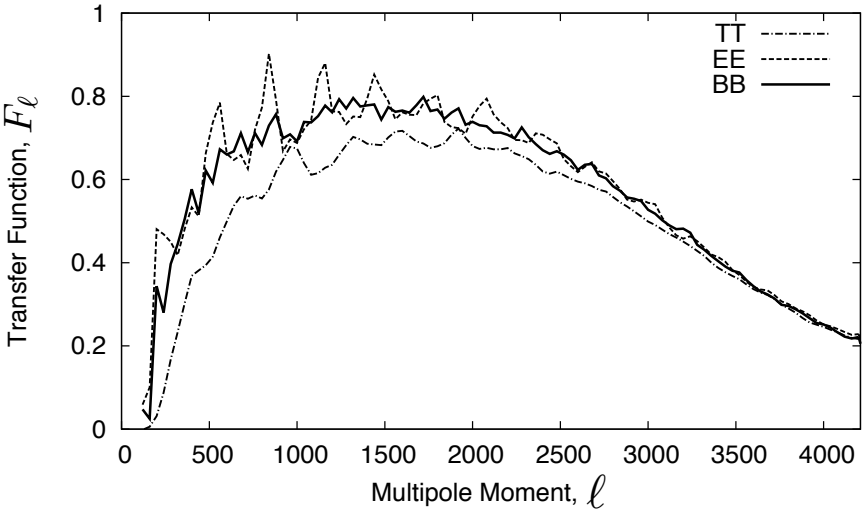

Figure 4.11: The filter transfer functions for TT, EE, and BB. This shows the impact of filtering on both signal and noise over the full first season. The decay of the transfer function at higher ℓs is due to the effects of the low-pass filtering. The sharp fall at lower ℓ is due to the polynomial filtering. As seen in section 4.5.1, the ground template is fairly homogeneous as a function of $|\ell|$ (though is highly anisotropic as a function of the Fourier space azimuthal angle $\varphi_{\vec{\ell}}$) and so it primarily affects the overall amplitude of the transfer function. Figure from [43].

$M_{\ell\ell'}$, F_ℓ, and B_ℓ are all calculated at the high-resolution ($\Delta\ell = 40$) binning. If it were possible to use these to directly solve equation 4.11 then this would suffice. However, because of the small, highly correlated bins we have used to calculate our pseudo-spectra, the mode coupling matrix $M_{\ell\ell'}$ is singular at this resolution. We thus cannot invert $K_{\ell\ell'}$ to solve equation 4.11 for the true D_ℓ given $\tilde{D}_\ell$.

We proceed by binning $\tilde{D}_\ell$ and $K_{\ell\ell'}$ into wider bins to produce $\tilde{D}_b$ and $K_{bb'}$. The advantage of the initial high-resolution binning is that the computationally intensive steps only need to be performed once, and different binning options can be implemented at the final step with little penalty. We choose four equally spaced bins between $500 < \ell < 2100$ using $\Delta\ell = 400$. This both reduces the correlations between the bins as well as reduces the error on each bin. We are left with:

$$\langle \tilde{D}_b \rangle = \sum_{b'} K_{bb'} \langle D_{b'} \rangle, \tag{4.13}$$

so our unbiased estimate of the band power D_b in each bin b is:

$$D_b = \sum_{b'} K^{-1}_{bb'} \tilde{D}_b \tag{4.14}$$

At this level of binning, each bin is sufficiently uncorrelated to allow us to invert $K_{bb'}$ to form $K^{-1}_{bb'}$ as required by 4.14.

4.6.5 Error Bar Estimation

The uncertainty in the binned power spectrum is estimated analytically as described in [67]. The analytically calculated error bars include two terms: a sample variance term based on the expected value from the binned best-fit WMAP-9 ΛCDM power spectra, and a noise variance term based on the noise in our maps. The sample variance term occurs because our measurement of the power spectrum corresponds to measuring the variance of a Gaussian distribution: each mode we measure corresponds to one "draw" from this distribution, and so with more modes our uncertainty on the variance decreases. This is related to the term "cosmic variance," which refers to the limited number of modes that exist on the full sky and corresponds to the ultimate sample variance that can be achieved. However, because we measure a small fraction of the sky our sample variance is higher than this cosmic variance limit.

With the appropriate weighting, the noise bias of the daily auto-spectra formed by cross-correlating maps from the same day of data is a good estimator for the variance of the power spectrum estimator. The signal is subtracted from

the auto-spectrum using the cross-spectrum estimator (equation 4.12) to form a estimate of the noise variance $N_{\vec{\ell}}$ as:

$$N_{\vec{\ell}} = \frac{\sum_i w_i^2}{(\sum_i w_i)^2}\Big[\frac{1}{\sum_i w_i^2}\sum_i w_i^2 \tilde{\boldsymbol{m}}_i^X \tilde{\boldsymbol{m}}_i^{Y*} - \frac{1}{\sum_{i\neq j} w_i w_j}\sum_{i\neq j} w_i w_j \tilde{\boldsymbol{m}}_i^X \tilde{\boldsymbol{m}}_j^{Y*}\Big], \tag{4.15}$$

where again $X, Y \in [T, E, B]$ and with i and j indexing the map number. This estimate of the noise variance is azimuthally averaged, binned, and multiplied by $K_{bb'}$ in the same way as the pseudo-spectra to estimate the noise variance in the binned power spectra. The noise variance and sample variance terms are both reduced by a factor of $\sqrt{\frac{2}{\nu_b}}$, where ν_b is the number of degrees of freedom, or independent Fourier modes, in each bin. ν_b is calculated analytically from the apodization masks as described in [68]. The loss of degrees of freedom (modes) due to filtering is not currently accounted for.

The error estimator is tested on simulated TOD formed by scanning simulated maps generated with WMAP-9 ΛCDM cosmology. Noise is injected into the TOD using either white noise or a noise model that takes account of measured temporal correlations of the detector noise. For both noise models, the uncertainty estimator correctly recovers the spread in power spectra estimated from random realizations of the sky and the noise to within 10%. For reasons we do not understand the analytic estimate appears to be biased high, which makes the errors conservative and so was considered acceptable.

4.7 Absolute Gain Calibration

Due to inaccuracies in planet temperature modeling and map reconstruction, the gains we measure in section 3.1 are only relative. In order to make an absolute measurement of C_ℓ^{BB} we need an absolute calibration of the gains. In order to do this, we co-add the C_ℓ^{TT} spectra from all three patches and fit for a single absolute gain factor to minimize the difference between our measurement of C_ℓ^{TT} and the binned best fit WMAP-9 ΛCDM C_ℓ^{TT} spectra. For our final data set,

this fit indicates that the gains must be increased by 32%, and so all gain factors are multiplied by 1.32 and the power spectrum estimation procedure is repeated. Accounting for the noise and sample variance as well as the beam uncertainty described in section 3.4, we find that the three patch C_ℓ^{TT} spectra as well as the combined C_ℓ^{TT} spectra is consistent with the WMAP-9 ΛCDM C_ℓ^{TT} spectrum.

4.8 Absolute Polarization Angle Calibration

As described in section 3.2, misaligning the polarization orientation angle of the instrument with respect to the coordinates in which E and B are calculated from Q and U results in a rotation of E into B. For a misalignment of angle α, this can be written as [74]:

$$\begin{aligned} E(\vec{\ell}) &= \cos(2\alpha)\widetilde{E}(\vec{\ell}) + \sin(2\alpha)\widetilde{B}(\vec{\ell}) \\ &\approx \widetilde{E}(\vec{\ell}) + 2\alpha\widetilde{B}(\vec{\ell}) \\ B(\vec{\ell}) &= -\sin(2\alpha)\widetilde{E}(\vec{\ell}) + \cos(2\alpha)\widetilde{B}(\vec{\ell}) \\ &\approx -2\alpha\widetilde{E}(\vec{\ell}) + \widetilde{B}(\vec{\ell}) \end{aligned} \tag{4.16}$$

where " $\widetilde{}$ " indicates a primordial quantity, and the approximations rely on $\alpha \ll \pi$. The relative amplitudes of E and B mean that leaking a small amount of E into B is a potentially significant source of systematic error:

$$\Delta C_\ell^{BB} = \langle BB(\vec{\ell}) - \widetilde{B}\widetilde{B}(\vec{\ell})\rangle_{\varphi_{\vec{\ell}}} \approx 4\alpha^2 C_\ell^{\widetilde{E}\widetilde{E}} \tag{4.17}$$

This rotation will also affect C_ℓ^{EB}, which is otherwise zero ($\widetilde{E}$ and $\widetilde{B}$ are uncorrelated):

$$\Delta C_\ell^{EB} = \langle EB(\vec{\ell})\rangle_{\varphi_{\vec{\ell}}} \approx 2\alpha C_\ell^{\widetilde{E}\widetilde{E}} + 2\alpha C_\ell^{\widetilde{B}\widetilde{B}} \approx 2\alpha C_\ell^{\widetilde{E}\widetilde{E}} \tag{4.18}$$

We thus fit for a rotation angle error using the measured value of C_ℓ^{EB}, remove the rotation in the Q and U maps, and again repeat the power spectrum estimation procedure. This leads to a correction of 1.08° relative to the Tau A calibrated value. The statistical uncertainty of this correction is ±0.20°. The C_ℓ^{EB} spectra before and after the self-calibration procedure are shown in figure 4.12.

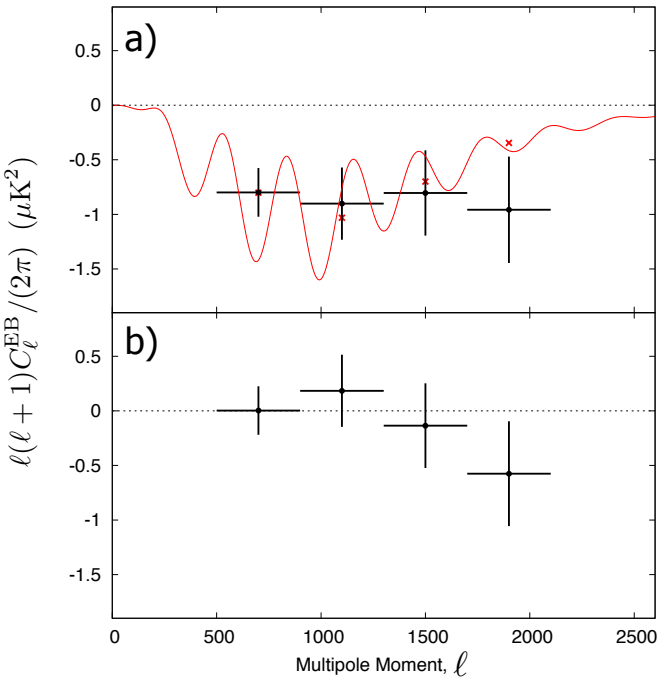

Figure 4.12: In **a)** the C_ℓ^{EB} spectrum is shown before the absolute angle calibration, which rotates all detector polarization angles by 1.08°. In **b)** C_ℓ^{EB} is shown after the absolute angle calibration procedure, and is consistent with zero. Figure from [43].

In addition to a polarization rotation introduced by an instrumental miscalibration, there are also potential mechanisms involving exotic physics for rotation the primordial polarization of the CMB before it reaches us [61]. If we are interested in measuring C_ℓ^{BB} generated by primordial gravitational waves or by gravitational lensing, de-rotation based on the C_ℓ^{EB} spectrum is the correct procedure. Measuring C_ℓ^{EB}, C_ℓ^{TB}, and C_ℓ^{BB} due to intrinsic rotation of CMB polarization will be a target of future stages of the experiment, but will require better control over systematic errors of polarization angle calibration without using the CMB.

4.9 C_L^{dd} Estimation

As described by equation 1.25, gravitational lensing will create correlations between different parts of the 2D Fourier plane. In particular, denoting averages

over ensembles of different CMB skies as $\langle\ \rangle_{\rm CMB}$, this leads to:

$$\begin{aligned}\langle E(\vec{\ell})E(\vec{\ell}')\rangle_{\rm CMB} &= \tilde{C}_\ell^{EE}(\vec{L}\cdot\vec{\ell})\cos(2\varphi_{\vec{\ell}\vec{\ell}'})\phi(\vec{L})\\ \langle E(\vec{\ell})B(\vec{\ell}')\rangle_{\rm CMB} &= \tilde{C}_\ell^{EE}(\vec{L}\cdot\vec{\ell})\sin(2\varphi_{\vec{\ell}\vec{\ell}'})\phi(\vec{L}),\end{aligned} \tag{4.19}$$

where $\vec{L} = \vec{\ell} + \vec{\ell}'$, $\tilde{C}_\ell^{EE}$ indicates the primordial (un-lensed) C_ℓ^{EE}spectrum, and $\varphi_{\vec{\ell}\vec{\ell}'} = \varphi_{\vec{\ell}'} - \varphi_{\vec{\ell}}$, as before. We may then define the estimators:

$$\begin{aligned}d_{EE}(\vec{L}) &= \frac{A_{EE}(L)}{L}\int\frac{d^2\vec{\ell}}{(2\pi)^2}E(\vec{\ell})E(\vec{\ell}')\frac{\tilde{C}_\ell^{EE}\vec{L}\cdot\vec{\ell}}{C_\ell^{EE}C_{\ell'}^{EE}}\cos(2\varphi_{\vec{\ell}\vec{\ell}'})\\ d_{EB}(\vec{L}) &= \frac{A_{EB}(L)}{L}\int\frac{d^2\vec{\ell}}{(2\pi)^2}E(\vec{\ell})B(\vec{\ell}')\frac{\tilde{C}_\ell^{EE}\vec{L}\cdot\vec{\ell}}{C_\ell^{EE}C_{\ell'}^{BB}}\sin(2\varphi_{\vec{\ell}\vec{\ell}'}),\end{aligned} \tag{4.20}$$

that with the appropriate normalization factors $A_{EE}(L)$ and $A_{EB}(L)$ give an estimate of the deflection $d(\vec{L}) \equiv L\phi(\vec{L})$ [38]. Note that $L\phi(\vec{L})$ in Fourier space is equivalent to $\nabla\phi(\hat{n})$ in real space, making this equivalent to our earlier description of the deflection field. Here $\tilde{C}_\ell^{EE}$ is the theoretical un-lensed power spectra, and C_ℓ^{EE} and $C_{\ell'}^{BB}$ are the theoretical lensed power spectra. These estimators weight the variance between different parts of Fourier space according to theoretical expectations of the power spectra to form a minimum variance estimate of the deflection. If the theoretical expectations are wrong then the estimators become non-optimal [38]. In the future, the theoretical lensed spectra could be replaced with measurements of C_ℓ^{BB} and C_ℓ^{EE} with sufficient signal-to-noise ratio, thus making the required theoretical inputs for the estimators disconnected from $C_\ell^{\phi\phi}$.

The POLARBEAR full season co-added maps for each of the three sky patches serve as inputs to a separate pipeline which estimates C_L^{dd}. The Q and U maps are transformed into E and B and estimates of d are formed based on the operators above. Estimates of d are then correlated with each other to produce an estimate of C_L^{dd}. Only the combinations $\langle d_{EE}d_{EB}^*\rangle_{\varphi_{\vec{L}}}$ and $\langle d_{EB}d_{EB}^*\rangle_{\varphi_{\vec{L}}}$ are used to estimate C_L^{dd} so as to focus on the conversion of E-modes to B-modes as a probe of the lensing. Estimates of the covariances come from simulations with noise matching the measured map noise. Simulations are performed with and without lensing. The presence of lensing in the simulations increases the covariances as well as correlates

the estimates from $\langle d_{EE} d^*_{EB} \rangle_{\varphi_{\vec{L}}}$ and $\langle d_{EB} d^*_{EB} \rangle_{\varphi_{\vec{L}}}$, which in the absence of lensing are uncorrelated.

Figures 4.8, 4.11, and 4.12 are reprints of material as it appears in A Measurement of the Cosmic Microwave Background B-Mode Polarization Power Spectrum at Sub-Degree Scales with POLARBEAR. The POLARBEAR Collaboration: P. A. R. Ade, Y. Akiba, A. E. Anthony, K. Arnold, M. Atlas, D. Barron, D. Boettger, J. Borrill, S. Chapman, Y. Chinone, M. Dobbs, T. Elleflot, J. Errard, G. Fabbian, C. Feng, D. Flanigan, A. Gilbert, W. Grainger, N. W. Halverson, M. Hasegawa, K. Hattori, M. Hazumi, W. L. Holzapfel, Y. Hori, J. Howard, P. Hyland, Y. Inoue, G. C. Jaehnig, A. H. Jaffe, B. Keating, Z. Kermish, R. Keskitalo, T. Kisner, M. Le Jeune, A. T. Lee, E. M. Leitch, E. Linder, M. Lungu, F. Matsuda, T. Matsumura, X. Meng, N. J. Miller, H. Morii, S. Moyerman, M. J. Myers, M. Navaroli, H. Nishino, H. Paar, J. Peloton, D. Poletti, E. Quealy, G. Rebeiz, C. L. Reichardt, P. L. Richards, C. Ross, I. Schanning, D. E. Schenck, B. D. Sherwin, A. Shimizu, C. Shimmin, M. Shimon, P. Siritanasak, G. Smecher, H. Spieler, N. Stebor, B. Steinbach, R. Stompor, A. Suzuki, S. Takakura, T. Tomaru, B. Wilson, A. Yadav, and O. Zahn, ArXiv e-prints, Mar. 2014. The dissertation author made essential contributions to many aspects of this work.

Chapter 5

Instrumental Systematic Error Constraints

The statistical uncertainty in our measurement of C_ℓ^{BB} comes from our data, as described in section 4.6.5. We also need to place constraints on the level of falsely generated B-mode polarization due to problems with mis-calibration or other instrumental defects. We assess the impact of many potential instrumental systematic errors on C_ℓ^{BB} and below and constrain them to be orders of magnitude smaller than the expected ΛCDM C_ℓ^{BB}power spectrum and our statistical error bars. We pay special attention to the effects of systematic errors in gain as calibration of detector gain has been a major theme of this dissertation.

5.1 Differential Gain Systematic Error Constraints

If the gain of the two bolometers in a pair are incorrect by different amounts, a false polarization signal will be generated when the TOD from the two detectors is differenced. This is frequently referred to as "leaking" temperature to polarization because the pixel can observe an unpolarized temperature field and record a polarization signal that is proportional to temperature.

The CMB temperature signal is orders of magnitude larger than the B-mode

signal we are searching for, and thus this leakage from temperature to polarization is a potentially significant source of systematic error. We will describe here several different techniques employed to constrain this error.

5.1.1 High Resolution Simulations

One way to study the potential impact of gain systematics is to compare the impact of using different gain models on C_ℓ^{BB}. We do this using noise-free simulations. Unlensed WMAP-9 ΛCDM spectra are used to generate maps with no C_ℓ^{BB}. These maps are scanned with real POLARBEAR pointing data to create noiseless TOD. A modified gain model is used to reverse-calibrate these TOD into ADC counts. The true POLARBEAR gain model is then used to reconstruct the maps in K_{CMB} units from the TOD generated by the alternate gain model. Any C_ℓ^{BB} power present in the final maps is a systematic effect generated by the differences in the gain models. We can then compare the amplitude of C_ℓ^{BB} generated by the difference in gain models to the theoretical value of C_ℓ^{BB} we are interested in measuring to see if the systematic error is relevant.

We use simulations of this kind to compare four variations of the gain model to the actual model employed in the analysis. The first is designed to study differences in the P_a and α terms in the gain model; that is, the terms that depend on the HWP angle. We use values of P_a and α determined from fits to elevation nod data taken during each different gain epoch. To generate this gain model the P_a and α values are replaced but the O_{NR} value is left unchanged from its planet derived value. All direct planet measurements are replaced with model fits where possible. Where this is not possible, the data is not included in the comparison.

The second model we compare to alters the O_{NR} term in the gain model. We solve for the value of O_{NR} for each pixel such that the fits for Δg_j from equation 3.31 are zero. This is equivalent to allowing the Tau A measurements to determine our O_{NR} values. Because O_{NR} is independent of the HWP angle, we simply apply the appropriate shift to all values of $P_{\rm frac}$ in or gain model regardless of whether the measured value of $P_{\rm frac}$ was derived from a direct measurement or a model fit. After generating these new gains, we also recompute the Tau A analysis to confirm

that no differential gain is measured after the correction is applied.

The third gain model removes the time interpolation from the gain model. The gains are derived entirely from the thermal source calibration measurement at the beginning of every hour and are assumed to be constant over that entire hour.

Finally, in the fourth gain model we shift all $P_{\rm frac}$ values by 1σ given the error bars described in 3.1. The results of comparing all four of these altered gain models to the gain model employed in analysis is shown in figure 5.1.

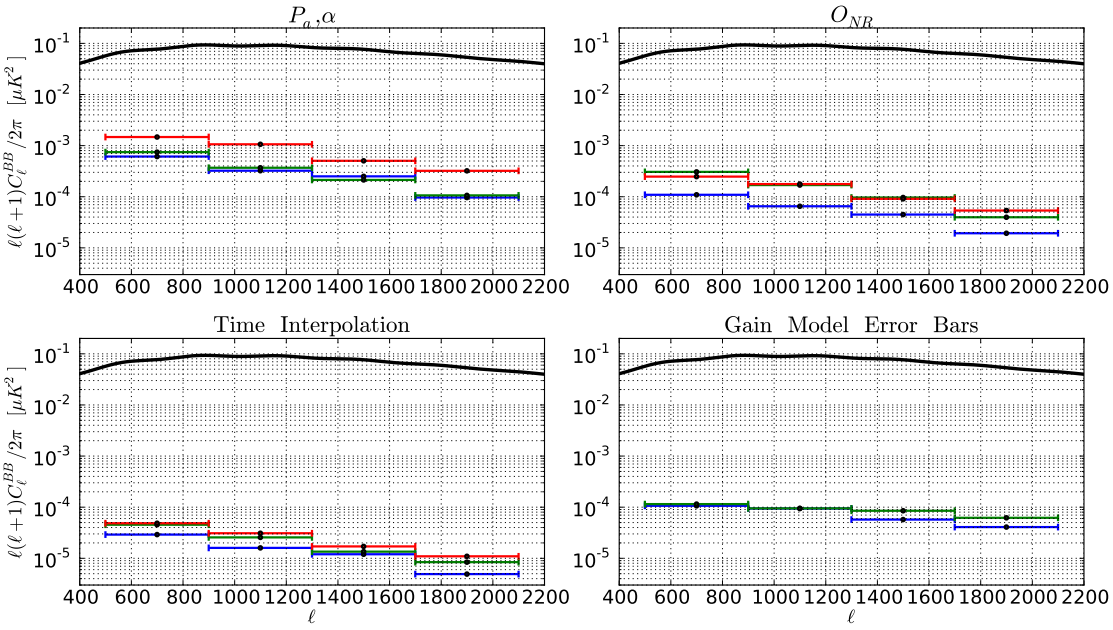

Figure 5.1: Changes to C_ℓ^{BB} resulting from altering the gain model are shown. The ΛCDM theory C_ℓ^{BB} curve is shown in black. The sky patch RA23 is shown in blue, RA12 in green, and RA4.5 in red. The "P_a, α" plot shows changes from the gain model using elevation nod data. The "O_{NR}" plot shows the changes introduced by using the Tau A derived O_{NR} values. The "Time Interpolation" plot shows the changes introduced by doing no gain interpolation. The "Gain Model Error Bars" show the changes introduced by shifting all $P_{\rm frac}$ values by one error bar width.

We have compared the impact of using completely independent measurements of all elements of our differential gain model. The results of these comparisons indicate changes in C_ℓ^{BB} that are much smaller than the signal we are trying to measure and much smaller than our statistical error bars. We therefore find the level of uncertainty implied by these comparisons to be acceptable.

5.1.2 Differential Gain Mapmaking

There is a specific source of potential relative gain error that we model and constrain further. Differences in the spectral band pass filters on bolometers within a pixel will alter the O_{NR} term in the gain model. We modify our instrument model slightly to produce a new set of maps which we use to constrain mis-estimation of this effect. Because pixels on the same detector wafer with the same polarization orientation are expected to share common spectral features, we combine data from these sets of pixels to increase our sensitivity to differential-band induced errors. We model difference TOD as:

$$d_t^{\rm diff} = G_t + \cos(2\Theta_t)Q_t + \sin(2\Theta_t)U_t. \tag{5.1}$$

This model takes advantage of the fact that the relative gain error introduced by differential spectra does not change as a function of waveplate angle. We proceed with map making, creating G, Q, and U maps for each of the two polarization orientations of pixels on each wafer. The G maps can then be correlated with temperature maps to estimate the gain leakage. No power is detected in any of the TG cross-spectra; the measured leakage value for each pixel type on each wafer is consistent with zero. Simulations that include wafer common mode differential gain leakage at the level constrained by the TG cross-spectra show negligible systematic bias. We take this as further evidence that the O_{NR} term in our gain model does not have error at a level relevant to our current measurement of C_ℓ^{BB}.

5.1.3 Temperature-Polarization Correlations

We introduce one further test of relative gain error useful for constraining error in any of the gain model terms. A technique for modeling differential gain leakage is to assume that the Q and U maps we measure can be written as follows:

$$\begin{aligned} Q(\vec{x}) &= \check{Q}(\vec{x}) + \gamma_1 T(\vec{x}) \\ U(\vec{x}) &= \check{U}(\vec{x}) + \gamma_2 T(\vec{x}), \end{aligned} \tag{5.2}$$

where quantities marked with a " ˇ " represent fields as they exist on the sky and

quantities without a " ˇ " represent the measured (perturbed) fields[1]. In this model, γ_1 and γ_2 represent uniform or averaged fractional leakage from temperature into Q and U, respectively. We can then write, using equation 1.19:

$$\begin{aligned} B(\vec{\ell}) &= -(\check{Q}(\vec{\ell}) + \gamma_1 T(\vec{\ell})) \sin(2\varphi_{\vec{\ell}}) + (\check{U}(\vec{\ell}) + \gamma_2 T(\vec{\ell})) \cos(2\varphi_{\vec{\ell}}) \\ &= \check{B}(\vec{\ell}) - \gamma_1 T(\vec{\ell}) \sin(2\varphi_{\vec{\ell}}) + \gamma_2 T(\vec{\ell}) \cos(2\varphi_{\vec{\ell}}). \end{aligned} \tag{5.3}$$

The 2D BB spectrum then takes the form:

$$\begin{aligned} BB = \check{B}\check{B} - 2\gamma_1 T\check{B} \sin(2\varphi_{\vec{\ell}}) + 2\gamma_2 T\check{B} \cos(2\varphi_{\vec{\ell}}) \\ +\gamma_1^2 TT \sin^2(2\varphi_{\vec{\ell}}) + \gamma_2^2 TT \cos^2(2\varphi_{\vec{\ell}}) - 2\gamma_1\gamma_2 TT \sin(2\varphi_{\vec{\ell}}) \cos(2\varphi_{\vec{\ell}}), \end{aligned} \tag{5.4}$$

where we have allowed the dependence on $\vec{\ell}$ to become implicit. We can then azimuthally average the spectra to get:

$$\begin{aligned} C_\ell^{BB} &= C_\ell^{\check{B}\check{B}} + \gamma_1^2 \langle TT \sin^2(2\varphi_{\vec{\ell}}) \rangle_{\varphi_{\vec{\ell}}} + \gamma_2^2 \langle TT \cos^2(2\varphi_{\vec{\ell}}) \rangle_{\varphi_{\vec{\ell}}} \\ &\quad -2\gamma_1\gamma_2 \langle TT \cos(2\varphi_{\vec{\ell}}) \sin(2\varphi_{\vec{\ell}}) \rangle_{\varphi_{\vec{\ell}}} \\ &\approx C_\ell^{\check{B}\check{B}} + \gamma_1^2 C_\ell^{TT} \langle \sin^2(2\varphi_{\vec{\ell}}) \rangle_{\varphi_{\vec{\ell}}} + \gamma_2^2 C_\ell^{TT} \langle \cos^2(2\varphi_{\vec{\ell}}) \rangle_{\varphi_{\vec{\ell}}} \\ &\quad -2\gamma_1\gamma_2 C_\ell^{TT} \langle \cos(2\varphi_{\vec{\ell}}) \sin(2\varphi_{\vec{\ell}}) \rangle_{\varphi_{\vec{\ell}}} \\ &= C_\ell^{\check{B}\check{B}} + C_\ell^{TT} \frac{(\gamma_1^2 + \gamma_2^2)}{2}. \end{aligned} \tag{5.5}$$

The terms proportional to $T\check{B}$ are set to zero because there should be no correlation between T and B on the sky. Further, all terms with $T\check{B}$ are proportional to $\cos(2\varphi_{\vec{\ell}})$ or $\sin(2\varphi_{\vec{\ell}})$, which also average to zero. We conclude that:

$$C_\ell^{BB,leakage} = \frac{(\gamma_1^2 + \gamma_2^2)}{2} C_\ell^{TT} = \gamma_{\rm eff}^2 C_\ell^{TT}, \tag{5.6}$$

defining:

$$\gamma_{\rm eff} = \sqrt{\frac{\gamma_1^2 + \gamma_2^2}{2}}. \tag{5.7}$$

[1]The symbol " ˜ " is typically used to indicate primordial quantities as a way of differentiating them from quantities that have been altered since the last scattering surface by, e.g., gravitational lensing. Here we use a similar notation but emphasize that our meaning is slightly different: " ˇ " indicates a quantity as it appears on the current sky including all effects that occur between the telescope and the last scattering surface.

Using equation 5.6 we can directly account for the impact of gain leakage on the BB spectrum via the γ_1 and γ_2 parameters. We thus seek a technique for measuring the values of γ_1 and γ_2, and ultimately γ_{eff}.

Differential Gain Leakage Estimators

We could construct a set of estimators for γ_1 and γ_2 defined in equation 5.2 by correlating with Q and U with T:

$$\begin{aligned} TQ &= T\check{Q} + \gamma_1 TT \\ TU &= T\check{U} + \gamma_2 TT. \end{aligned} \tag{5.8}$$

$C_\ell^{T\check{Q}}$ and $C_\ell^{T\check{U}}$ vanish, and so azimuthally averaging these spectra gives:

$$\begin{aligned} C_\ell^{TQ} &= \gamma_1 C_\ell^{TT} \\ C_\ell^{TU} &= \gamma_2 C_\ell^{TT}, \end{aligned} \tag{5.9}$$

so that:

$$\begin{aligned} {\gamma_1}^{TQ} &= \frac{C_\ell^{TQ}}{C_\ell^{TT}} \\ {\gamma_2}^{TU} &= \frac{C_\ell^{TU}}{C_\ell^{TT}}. \end{aligned} \tag{5.10}$$

However, Q and U include the variance from the E-mode signal, and it is instead desirable to derive estimators for the γs that come from E and B separately. We will explore this concept in a bit more detail below.

To proceed, we write down a model for E and B including differential gain parameterized by γ_1 and γ_2. We also allow for a polarization rotation angle error α:

$$\begin{aligned} B &= -\left(\check{Q} + \gamma_1 T\right)\sin(2\varphi_{\vec{\ell}}) + \left(\check{U} + \gamma_2 T\right)\cos(2\varphi_{\vec{\ell}}) - 2\alpha E \\ &= \check{B} - \gamma_1 T \sin(2\varphi_{\vec{\ell}}) + \gamma_2 T \cos(2\varphi_{\vec{\ell}}) - 2\alpha E \\ E &= \left(\check{Q} + \gamma_1 T\right)\cos(2\varphi_{\vec{\ell}}) + \left(\check{U} + \gamma_2 T\right)\sin(2\varphi_{\vec{\ell}}) \\ &= \check{E} + \gamma_1 T \cos(2\varphi_{\vec{\ell}}) + \gamma_2 T \sin(2\varphi_{\vec{\ell}}). \end{aligned} \tag{5.11}$$

Now correlate both E and B with T:

$$\begin{aligned} TB &= T\check{B} - \gamma_1 TT\sin(2\varphi_{\vec{\ell}}) + \gamma_2 TT\cos(2\varphi_{\vec{\ell}}) - 2\alpha TE \\ TE &= T\check{E} + \gamma_1 TT\cos(2\varphi_{\vec{\ell}}) + \gamma_2 TT\sin(2\varphi_{\vec{\ell}}). \end{aligned} \tag{5.12}$$

At this point, a simple azimuthal average over $\varphi_{\vec{\ell}}$ eliminates dependence on γ_1 and γ_2. That is, the set of γs integrate out of $\langle TB\rangle_{\varphi_{\vec{\ell}}} = C_\ell^{TB}$ and $\langle TE\rangle_{\varphi_{\vec{\ell}}} = C_\ell^{TE}$ and leave no γ dependence because TT is isotropic while the $\sin(2\varphi_{\vec{\ell}})$ or $\cos(2\varphi_{\vec{\ell}})$ average to zero. Notice that the dependence on α is preserved, which of course is what makes C_ℓ^{TB} a useful estimator for correcting the polarization rotation angle.

If we instead weight the 2D spectra by $\cos(2\varphi_{\vec{\ell}})$ or $\sin(2\varphi_{\vec{\ell}})$ before averaging, we preserve the dependence on the γs:

$$\begin{aligned} \langle TB\sin(2\varphi_{\vec{\ell}})\rangle_{\varphi_{\vec{\ell}}} &= \langle T\check{B}\sin(2\varphi_{\vec{\ell}})\rangle_{\varphi_{\vec{\ell}}} - \gamma_1\langle TT\sin^2(2\varphi_{\vec{\ell}})\rangle_{\varphi_{\vec{\ell}}} \\ &\quad +\gamma_2\langle TT\sin(2\varphi_{\vec{\ell}})\cos(2\varphi_{\vec{\ell}})\rangle_{\varphi_{\vec{\ell}}} - 2\alpha\langle TE\sin(2\varphi_{\vec{\ell}})\rangle_{\varphi_{\vec{\ell}}} \\ &\approx C_\ell^{T\check{B}}\langle\sin(2\varphi_{\vec{\ell}})\rangle_{\varphi_{\vec{\ell}}} - \gamma_1 C_\ell^{TT}\langle\sin^2(2\varphi_{\vec{\ell}})\rangle_{\varphi_{\vec{\ell}}} + \gamma_2 C_\ell^{TT}\langle\sin(2\varphi_{\vec{\ell}})\cos(2\varphi_{\vec{\ell}})\rangle_{\varphi_{\vec{\ell}}} \\ &\quad -2\alpha C_\ell^{TE}\langle\sin(2\varphi_{\vec{\ell}})\rangle_{\varphi_{\vec{\ell}}} \\ &= -\frac{\gamma_1 C_\ell^{TT}}{2}, \end{aligned} \tag{5.13}$$

$$\begin{aligned} \langle TB\cos(2\varphi_{\vec{\ell}})\rangle_{\varphi_{\vec{\ell}}} &= \langle T\check{B}\cos(2\varphi_{\vec{\ell}})\rangle_{\varphi_{\vec{\ell}}} - \gamma_1\langle TT\sin(2\varphi_{\vec{\ell}})\cos(2\varphi_{\vec{\ell}})\rangle_{\varphi_{\vec{\ell}}} \\ &\quad +\gamma_2\langle TT\cos^2(2\varphi_{\vec{\ell}})\rangle_{\varphi_{\vec{\ell}}} - 2\alpha\langle TE\cos(2\varphi_{\vec{\ell}})\rangle_{\varphi_{\vec{\ell}}} \\ &\approx C_\ell^{T\check{B}}\langle\cos(2\varphi_{\vec{\ell}})\rangle_{\varphi_{\vec{\ell}}} - \gamma_1 C_\ell^{TT}\langle\sin(2\varphi_{\vec{\ell}})\cos(2\varphi_{\vec{\ell}})\rangle_{\varphi_{\vec{\ell}}} + \gamma_2 C_\ell^{TT}\langle\cos^2(2\varphi_{\vec{\ell}})\rangle_{\varphi_{\vec{\ell}}} \\ &\quad -2\alpha C_\ell^{TE}\langle\cos(2\varphi_{\vec{\ell}})\rangle_{\varphi_{\vec{\ell}}} \\ &= \frac{\gamma_2 C_\ell^{TT}}{2}, \end{aligned} \tag{5.14}$$

$$\begin{aligned} \langle TE\sin(2\varphi_{\vec{\ell}})\rangle_{\varphi_{\vec{\ell}}} &= \langle T\check{E}\sin(2\varphi_{\vec{\ell}})\rangle_{\varphi_{\vec{\ell}}} + \gamma_1\langle TT\sin(2\varphi_{\vec{\ell}})\cos(2\varphi_{\vec{\ell}})\rangle_{\varphi_{\vec{\ell}}} \\ &\quad +\gamma_2\langle TT\sin^2(2\varphi_{\vec{\ell}})\rangle_{\varphi_{\vec{\ell}}} \\ &\approx C_\ell^{T\check{E}}\langle\sin(2\varphi_{\vec{\ell}})\rangle_{\varphi_{\vec{\ell}}} + \gamma_1 C_\ell^{TT}\langle\sin(2\varphi_{\vec{\ell}})\cos(2\varphi_{\vec{\ell}})\rangle_{\varphi_{\vec{\ell}}} + \gamma_2 C_\ell^{TT}\langle\sin^2(2\varphi_{\vec{\ell}})\rangle_{\varphi_{\vec{\ell}}} \\ &= \frac{\gamma_2 C_\ell^{TT}}{2}, \text{ and} \end{aligned} \tag{5.15}$$

$$\begin{aligned}\langle TE\cos(2\varphi_{\vec{\ell}})\rangle_{\varphi_{\vec{\ell}}} &= \langle T\check{E}\cos(2\varphi_{\vec{\ell}})\rangle_{\varphi_{\vec{\ell}}} + \gamma_1\langle TT\cos^2(2\varphi_{\vec{\ell}})\rangle_{\varphi_{\vec{\ell}}} \\ &\quad +\gamma_2\langle TT\sin(2\varphi_{\vec{\ell}})\cos(2\varphi_{\vec{\ell}})\rangle_{\varphi_{\vec{\ell}}} \\ &\approx C_\ell^{T\check{E}}\langle\cos(2\varphi_{\vec{\ell}})\rangle_{\varphi_{\vec{\ell}}} + \gamma_1 C_\ell^{TT}\langle\cos^2(2\varphi_{\vec{\ell}})\rangle_{\varphi_{\vec{\ell}}} + \gamma_2 C_\ell^{TT}\langle\sin(2\varphi_{\vec{\ell}})\cos(2\varphi_{\vec{\ell}})\rangle_{\varphi_{\vec{\ell}}} \\ &= \frac{\gamma_1 C_\ell^{TT}}{2}.\end{aligned} \tag{5.16}$$

We see that the dependence on α is conveniently integrated out by this weighting scheme, which further increases its robustness. We now have four estimators, which we can write in their simplest form as:

$$\begin{aligned}\gamma_1^{TB^*} &\equiv -\frac{2\langle TB\sin(2\varphi_{\vec{\ell}})\rangle_{\varphi_{\vec{\ell}}}}{C_\ell^{TT}} \\ \gamma_1^{TE^*} &\equiv \frac{2\langle TE\cos(2\varphi_{\vec{\ell}})\rangle_{\varphi_{\vec{\ell}}}}{C_\ell^{TT}} \\ \gamma_2^{TB^*} &\equiv \frac{2\langle TB\cos(2\varphi_{\vec{\ell}})\rangle_{\varphi_{\vec{\ell}}}}{C_\ell^{TT}} \\ \gamma_2^{TE^*} &\equiv \frac{2\langle TE\sin(2\varphi_{\vec{\ell}})\rangle_{\varphi_{\vec{\ell}}}}{C_\ell^{TT}}.\end{aligned} \tag{5.17}$$

However, we find that we can reduce the variance of these estimators by not approximating the 2D TT spectrum as constant in the averaging terms $\langle TT\sin^2(2\varphi_{\vec{\ell}})\rangle_{\varphi_{\vec{\ell}}}$ and $\langle TT\cos^2(2\varphi_{\vec{\ell}})\rangle_{\varphi_{\vec{\ell}}}$, and instead choose to leave these terms in the estimator without this approximation. We define this additional, similar set of estimators as:

$$\begin{aligned}\gamma_1^{TB} &\equiv -\frac{\langle TB\sin(2\varphi_{\vec{\ell}})\rangle_{\varphi_{\vec{\ell}}}}{\langle TT\sin^2(2\varphi_{\vec{\ell}})\rangle_{\varphi_{\vec{\ell}}}} \\ \gamma_1^{TE} &\equiv \frac{\langle TE\cos(2\varphi_{\vec{\ell}})\rangle_{\varphi_{\vec{\ell}}}}{\langle TT\cos^2(2\varphi_{\vec{\ell}})\rangle_{\varphi_{\vec{\ell}}}} \\ \gamma_2^{TB} &\equiv \frac{\langle TB\cos(2\varphi_{\vec{\ell}})\rangle_{\varphi_{\vec{\ell}}}}{\langle TT\cos^2(2\varphi_{\vec{\ell}})\rangle_{\varphi_{\vec{\ell}}}} \\ \gamma_2^{TE} &\equiv \frac{\langle TE\sin(2\varphi_{\vec{\ell}})\rangle_{\varphi_{\vec{\ell}}}}{\langle TT\sin^2(2\varphi_{\vec{\ell}})\rangle_{\varphi_{\vec{\ell}}}}.\end{aligned} \tag{5.18}$$

It is interesting to note the relationship that exists between the set of estimators defined in equation 5.10 and those defined using TE or TB. If we start

with the expression $\frac{\gamma_1^{TB^*}+\gamma_1^{TE^*}}{2}$, we find the following:

$$\begin{aligned}
\frac{\gamma_1^{TB^*}+\gamma_1^{TE^*}}{2} &= \frac{2\frac{\langle TE\cos(2\varphi_{\vec{\ell}})\rangle_{\varphi_{\vec{\ell}}}}{C_\ell^{TT}} - 2\frac{\langle TB\sin(2\varphi_{\vec{\ell}})\rangle_{\varphi_{\vec{\ell}}}}{C_\ell^{TT}}}{2} \\
&= \frac{C_\ell^{T\check{E}}}{C_\ell^{TT}}\langle\cos(2\varphi_{\vec{\ell}})\rangle_{\varphi_{\vec{\ell}}} + \gamma_1\langle\cos^2(2\varphi_{\vec{\ell}})\rangle_{\varphi_{\vec{\ell}}} + \gamma_2\langle\sin(2\varphi_{\vec{\ell}})\cos(2\varphi_{\vec{\ell}})\rangle_{\varphi_{\vec{\ell}}} \\
&\quad -\frac{C_\ell^{T\check{B}}}{C_\ell^{TT}}\langle\sin(2\varphi_{\vec{\ell}})\rangle_{\varphi_{\vec{\ell}}} + \gamma_1\langle\sin^2(2\varphi_{\vec{\ell}})\rangle_{\varphi_{\vec{\ell}}} - \gamma_2\langle\sin(2\varphi_{\vec{\ell}})\cos(2\varphi_{\vec{\ell}})\rangle_{\varphi_{\vec{\ell}}} \\
&= \frac{C_\ell^{T\check{E}}}{C_\ell^{TT}}\langle\cos(2\varphi_{\vec{\ell}})\rangle_{\varphi_{\vec{\ell}}} - \frac{C_\ell^{T\check{B}}}{C_\ell^{TT}}\langle\sin(2\varphi_{\vec{\ell}})\rangle_{\varphi_{\vec{\ell}}} + \gamma_1\langle\cos^2(2\varphi_{\vec{\ell}}) + \sin^2(2\varphi_{\vec{\ell}})\rangle_{\varphi_{\vec{\ell}}} \\
&= \frac{C_\ell^{T\check{Q}}}{C_\ell^{TT}} + \gamma_1 = \frac{C_\ell^{TQ}}{C_\ell^{TT}} = \gamma_1^{TQ}.
\end{aligned} \tag{5.19}$$

We can use a similar construction for γ_2^{TU} and conclude that:

$$\begin{aligned}
\gamma_1^{TQ} &= \frac{\gamma_1^{TB^*}+\gamma_1^{TE^*}}{2} \\
\gamma_2^{TU} &= \frac{\gamma_2^{TB^*}+\gamma_2^{TE^*}}{2}.
\end{aligned} \tag{5.20}$$

We know that the cosmological variance in the E-modes is much greater than in the B-modes, and so we expect for instance that $\gamma_1^{TB^*}$ will be a lower variance estimator than $\gamma_1^{TE^*}$. Thus using estimators based on TQ and TU are equivalent to mis-weighting the contributions of the estimators derived from TE and TB. By separating into the TB and TE contributions we are free to choose a more optimal weighting.

For use on real data, we form the estimators γ_1^{TB}, γ_1^{TE}, γ_2^{TB}, and γ_2^{TE} using our standard cross-spectrum pipeline described above. We form the 2D TT, TB and EB spectra as normal, but then add in the factors of $\sin(2\varphi_{\vec{\ell}})$, $\cos(2\varphi_{\vec{\ell}})$, $\cos^2(2\varphi_{\vec{\ell}})$, and $\sin^2(2\varphi_{\vec{\ell}})$ as appropriate before the azimuthal averaging operation to form the pseudo-spectra as in equation 5.18. Because the gain leakage estimators are formed using ratios of two spectra, we do not run simulations to compute the filter transfer functions F_ℓ, and we also set the mode coupling $M_{\ell\ell'}$ to the identity matrix and the beam B_ℓ to unity everywhere when estimating the true spectra from the pseudo-spectra. Our results will come from comparison with white noise simulations which are treated identically, and so we do not believe these choices

impact our results.

Another important point to consider as we switch from the analytic derivation above to the practical application of these estimators is that the 2D Fourier space quantities we are using are formed from our biased maps. This bias in the maps can lead to a bias in our estimates of the gain leakage. For instance, in equation 5.13 we assume that $\langle TT \sin(2\varphi_{\vec{\ell}}) \cos(2\varphi_{\vec{\ell}}) \rangle_{\varphi_{\vec{\ell}}} = 0$. However, if our filter has created a bias by anisotropically suppressing Fourier modes, it is equivalent to removing or de-weighting them in the integral required for performing this average, meaning this term can be non-zero even if TT is isotropic. This bias is unrelated to not correcting the filter transfer function because it is a problem that occurs in the azimuthal averaging that takes place before the transfer function would ever be applied.

Estimators on Real Data

The estimators γ_1^{TB}, γ_2^{TB}, γ_1^{TE}, and γ_2^{TE} yield one value of γ_1 and γ_2 for each power spectrum bin. We would like to combine these values to estimate $\gamma_{\rm eff}$. We use leakage-free simulations to find the minimum variance combinations of the estimators to produce $\gamma_{\rm eff}$. We use simulations with artificial gain leakage to test for bias of the estimators by comparing the average estimated value of leakage to the known simulated value. We find that estimators constructed with TE suffer from greater γ-dependent bias than those constructed with TB, and so elect to use only the TB set of estimators. We find that the appropriate weighting to produce a minimum variance estimate of $\gamma_{\rm eff}$ is not altered by simulated leakage.

We use the minimum variance combinations to form estimates of $\gamma_{\rm eff}$ for our real data and simulations with no gain leakage. We then compare the spread in estimated values of $\gamma_{\rm eff}$ with no leakage to our measured value from the real data. We use the distribution of simulated values to compute the probability to exceed (PTE) for our measured value under the assumption of zero leakage, and find that all patches are consistent with no leakage, with a minimum PTE across the three patches of 27%. The results of this test are shown in figure 5.2.

In order to understand the utility of this test, we also created simulations

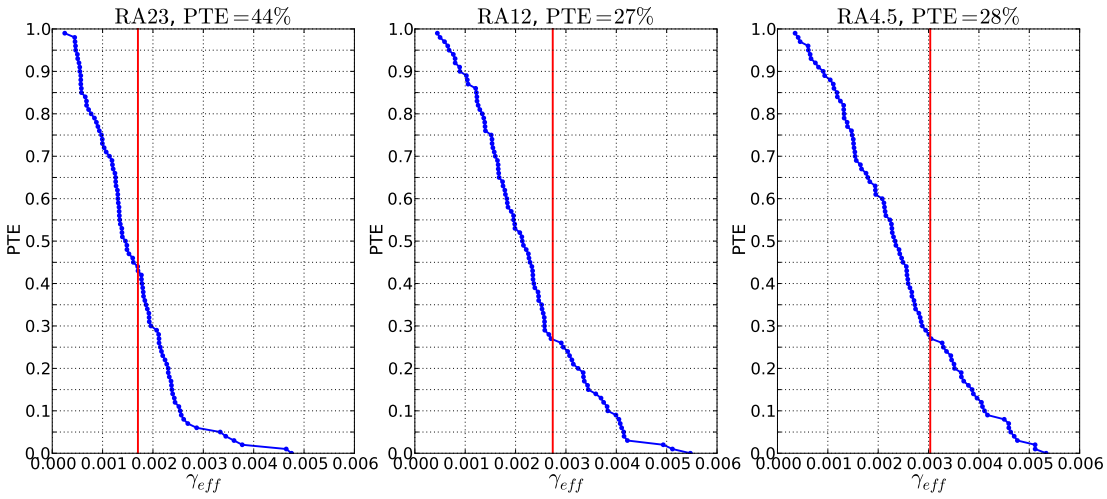

Figure 5.2: TB correlation measurements of $\gamma_{\rm eff}$ and PTEs for zero leakage are shown for the three sky patches. The distribution of $\gamma_{\rm eff}$ values from zero-leakage simulations for each patch are shown in blue. The measured value from real data on each patch is shown in red. All measured values are consistent with the hypothesis of zero leakage, with a minimum PTE across the three patches of 27%.

with uniform leakage of $\gamma 1 = \gamma 2 = 0.005$ and $\gamma 1 = \gamma 2 = 0.003$, equivalent to 0.5% and 0.3% uniform leakage, respectively. We find that all measured vales of $\gamma_{\rm eff}$ from our 0.5% leakages simulations exceed the real value measured in RA23. 86% of our simulations with 0.3% leakage exceed the measured value of leakage in RA23. We interpret this to mean that this test has the ability to constrain uniform leakage to be less than 0.5% while showing no evidence for leakage. The distributions for simulated leakage are shown in figure 5.3.

While this constraint is weaker than the others studied above, it is sensitive to all terms of the gain model, and constructed directly from the final data set we include in our analysis. Future efforts to remove bias and combine the TB and TE estimators will improve this technique.

5.2 Further Systematic Error Checks

In addition relative gain leakage, our measurement of C_ℓ^{BB} is sensitive to to a large number of other systematics. We use several techniques to study these systematic errors. The first is the high-resolution signal only simulations introduced

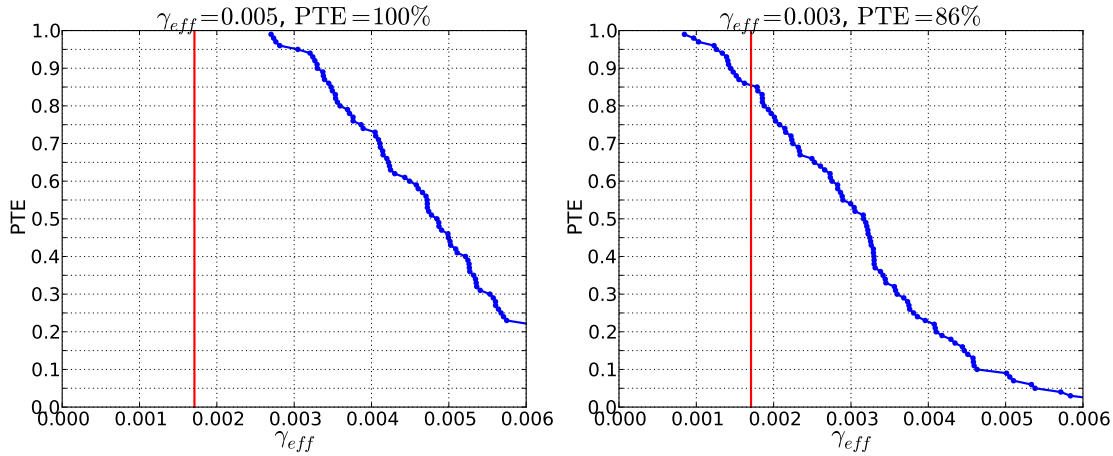

Figure 5.3: TB correlation measurements of $\gamma_{\rm eff}$ and PTEs for simulated leakage on the sky patch RA23. Measured values of $\gamma_{\rm eff}$ are shown in red and the results of simulations with 0.5% (left) and 0.3% (right) leakage are shown in blue. All simulations with 0.1% leakage exceed the actual measured value of $\gamma_{\rm eff}$, while 85% of simulations with 0.5% leakage exceeded the measured value. This is a measure of the statistical constraining power of this test and not a detection of leakage.

in section 5.1.1 in the context of studying relative gain leakage. This simulation framework is used to study other errors as well. We also employ an extensive suite of null tests which we will describe below.

5.2.1 Simulations

The simulation pipeline introduced in section 5.1.1 is also used to study the possible spurious C_ℓ^{BB} power generated by polarization orientation angle errors, errors in the pointing model, differential beam effects, as well as the relative gain calibration errors that were already discussed. We describe the simulations performed here; the results are summarized in figure 5.4.

Instrument Polarization Angle Errors

From the procedure described in section 3.2.1, the error on each pixel's polarization orientation angle is estimated to be $\pm 1^\circ$ and the error on the relative orientation angle of each wafer to the others is estimated to be $\pm 0.83^\circ$. Random realizations of polarization angle orientations are created for the focal plane using

these values and used to scan simulated maps free of BB signal to produce simulated TOD. These TOD are then re-processed using the measured polarization orientation angles. The overall orientation angle, not constrained to be zero in the simulation, is corrected using measurements of the C_ℓ^{EB} spectrum as done with the real data. The remaining level of C_ℓ^{BB} in the maps indicates contamination from the rotation angle error.

Pointing Model Errors

The now familiar technique of scanning a simulated map without BB power with one pointing model to create TOD, and then reconstructing the map using a different pointing model is used to study pointing model errors. The errors in the pointing model are derived from fitting pointing models to different sets of sources. The discrepancies found in this way exceed the statistical uncertainties on individual pointing model fits, so we chose them to represent the errors.

Bolometer Differential Pointing

If two bolometers within a pixel pair have their beam centers at slightly different points on the sky, this will couple the gradient of CMB temperature into the polarization measurement. The differential pointing offsets for all pixels on the focal plane are measured by comparing planet maps between the two bolometers within a given pixel pair. The normal map making procedure assumes that there is no differential pointing; the error generated by this assumption is quantified via simulations scanning simulated BB free maps with the measured differential pointing and reconstructing them using the assumption of no differential pointing.

Differential Beam Shapes

Differential ellipticity and differential beam size are also measured via planet scans. Their impact on $C_\ell^{BB}$is simulated using analytic models of how the beam parameters couple do derivatives of the CMB temperature map.

Readout Crosstalk

Because of the frequency domain multiplexing used in POLARBEAR, electrical crosstalk between different detector channels is expected. This is measured to be nominally 1% with the frequency spacing employed between channels in the readout. Simulations were performed using 2% crosstalk between nearest-neighbors in multiplexing frequency space. These simulations, which already show the effect to be negligible, did not include the effect of HWP rotation which would have further reduced the impact.

A summary of all the systematic error constraints is presented in figure 5.4 and table 5.1.

We also estimate limits on sources of multiplicative bias to the C_ℓ^{BB} estimate. The uncertainties in the beam model create uncertainties in the absolute gain calibration to the WMAP-9 ΛCDM C_ℓ^{TT} spectra, which we estimate to be 4.1%. The estimate of the polarization efficiency generated from Tau A (see section 3.2.1) leave a multiplicative uncertainty of 3.6%. Finally, the results of the transfer function estimation described in section 4.6.4 have some dependence on the input cosmology, leading to an additional 3.9% multiplicative uncertainty in the final estimate of C_ℓ^{BB}.

5.2.2 Null Tests

An extensive suite of null tests in used to check for internal consistency of the data and to search for possible systematic biases. The idea behind a null test is to split the data into two parts and check them for consistency. The consistency is checked by differencing the measurements resulting from the two sets of data, expected to be zero, resulting in the "null" designation. Because our mapmaking procedure anisotropically removes Fourier modes based on how each scan is executed, it is not generally possible to difference maps from two sets of data in a way that we expect to yield a null result. We thus work in power spectrum space, ensuring that the difference between power spectra of the two sets in question is consistent with zero. We compute these null tests for both $C_\ell^{BB}$and C_ℓ^{EB}.

The choice of which data splits to use depends on which systematic effect

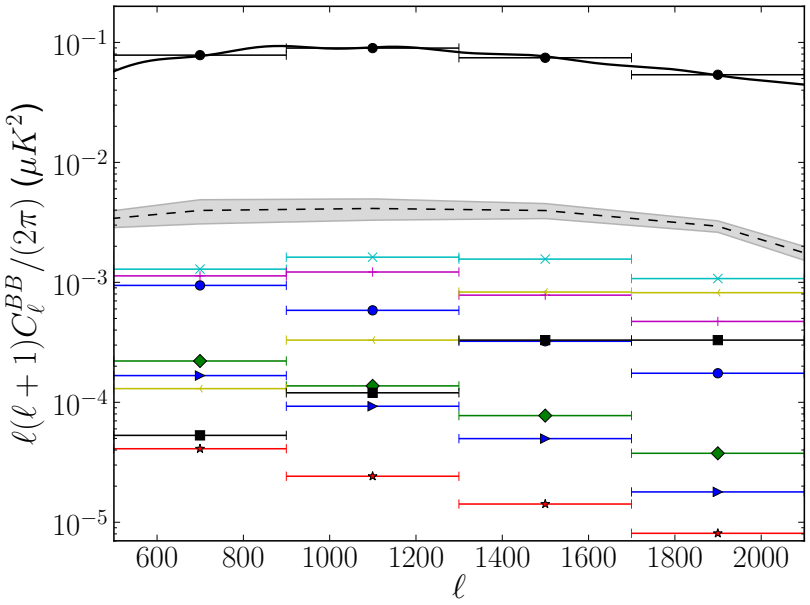

Figure 5.4: Possible bias from instrumental systematics errors in the C_ℓ^{BB} power spectra (ΛCDM theory spectra shown in black), as described in sections 5.1 and 5.2. Both the individual sources of uncertainty (solid color) and the cumulative bias coming from their combination (black dashed) are displayed after the combination of all CMB patches. The grey-shaded region show the 1σ bounds on the cumulative bias limit. This is found through Monte Carlo simulations of our observations with the systematics included. The effects included in this analysis were the pointing model and differential pointing uncertainty (light blue, cross mark), the residual uncertainty in instrument polarization angle after self-calibration (purple, plus mark), the differential beam size and ellipticity (yellow arrow and black square mark respectively), the electrical crosstalk (blue, arrow mark), the drift of the gains between two consecutive thermal source calibrator measurements (red star mark), and the O_{NR} gain model changes and P_a and α gain model changes (green diamond and blue circle mark respectively). Figure from [43].

is being investigated. In general, including many tests dilutes the statistical power of any one test. This is because when considering what constitutes a statistical "failure" of a null test, the total number of tests being run must be accounted for. Finding a single test with a PTE of 5% is far more likely in a suite with hundreds of tests than it is when considering one test alone. The criteria by which we evaluate the success of our tests must account for this.

We build null tests from a total of nine data splits: first vs. second half of the

Table 5.1: Estimates of the maximum contribution to C_ℓ^{BB} due to instrumental uncertainties that could bias (additively) the B-mode signal as estimated using the simulations described in sections 5.1 and 5.2.1. The linear sum of these effects in each band power is taken as an upper limit on the possible instrumental bias on the measurement.

Source of uncertainty	*Measurement technique*	*Maximum spurious* D_ℓ^{BB} $[10^{-4}\,\mu K^2]$
Boresight pointing	Comparison of pointing models	5.5
Differential pointing	Planet beammaps	7.1
Instrument & relative polarization angle	C_ℓ^{EB} statistical uncertainty and Tau A	12
Pixel-pair relative gain: O_{NR}	Comparison with Tau A; differential-gain map-making	2.2
Pixel-pair relative gain: P_a, α	Comparison with elevation nods	9.4
Pixel-pair relative gain: temporal drift	Comparison of compensation versus no compensation	0.41
Differential beam ellipticity	Planet beammaps	9.4
Differential beam size	Planet beammaps	3.3
Electrical crosstalk	Simulation of measured level	1.7
Total possible bias	*bin central* ℓ: 700, 1100, 1500, 1900	40, 41, 39, 29

season, patch rising vs. patch setting, high patch elevation vs. low patch elevation, high detector gain vs. low detector gain, good vs. bad weather, polarization orientation angle relative to the detector wafer, left vs. right side of the focal plane, positive vs. negative going subscans, and angle between the sky patch and the moon when the scan was taken. For each split we calculate a null spectrum $C_b^{\rm null}$ and $\chi_{\rm null,b} \equiv C_b^{\rm null}/\sigma_b$ and its square $\chi^2_{\rm null,b}$, where σ_b is estimated from simulations.

For each data split, we also run 500 Monte Carlo simulations that include

signal and white noise. The spread of the Monte Carlo simulations are compared to the real data to establish PTEs for the null hypothesis of no systematic error induced differences between the data sets. We require that the PTEs conform to a uniform distribution as reported by the Kolmogorov-Smirnov test, a standard technique for comparing sample distributions with theoretical reference distributions. Because this test is not sensitive to extreme outliers, we also have several different techniques for examining the outliers. We sum values of $\chi_{\mathrm{null,b}}$ and $\chi^2_{\mathrm{null,b}}$ in different ways and compute PTEs that are sensitive to problems focused on a particular spectral bin b across all tests, a particular spectrum (either C_ℓ^{BB} or C_ℓ^{EB}) across all bins and splits, or a particular data split across all bins and spectra. We then compute the PTE of a single test having the minimum PTE we find given the total number of tests we perform and require that it be above 5%. We find PTEs for this statistic are 32.8%, 55.6%, and 18.0% for RA4.5, RA12, and RA23 respectively. We thus find no evidence for systematic contamination or mis-calibration in the POLARBEAR data set or analysis procedures.

Figure 5.4, and table 5.1 are a reprint of material as it appears in A Measurement of the Cosmic Microwave Background B-Mode Polarization Power Spectrum at Sub-Degree Scales with POLARBEAR. The POLARBEAR Collaboration: P. A. R. Ade, Y. Akiba, A. E. Anthony, K. Arnold, M. Atlas, D. Barron, D. Boettger, J. Borrill, S. Chapman, Y. Chi- none, M. Dobbs, T. Elleflot, J. Errard, G. Fabbian, C. Feng, D. Flanigan, A. Gilbert, W. Grainger, N. W. Halverson, M. Hasegawa, K. Hattori, M. Hazumi, W. L. Holzapfel, Y. Hori, J. Howard, P. Hyland, Y. Inoue, G. C. Jaehnig, A. H. Jaffe, B. Keating, Z. Kermish, R. Keskitalo, T. Kisner, M. Le Jeune, A. T. Lee, E. M. Leitch, E. Linder, M. Lungu, F. Matsuda, T. Matsumura, X. Meng, N. J. Miller, H. Morii, S. Moyerman, M. J. Myers, M. Navaroli, H. Nishino, H. Paar, J. Peloton, D. Poletti, E. Quealy, G. Rebeiz, C. L. Reichardt, P. L. Richards, C. Ross, I. Schanning, D. E. Schenck, B. D. Sherwin, A. Shimizu, C. Shimmin, M. Shimon, P. Siritanasak, G. Smecher, H. Spieler, N. Stebor, B. Steinbach, R. Stompor, A. Suzuki, S. Takakura, T. Tomaru, B. Wilson, A. Yadav, and O. Zahn, ArXiv e-prints, Mar. 2014. The dissertation author made essential contributions to many aspects of this work.

Chapter 6

Results and Outlook

Power spectra results from the analysis of the first season of POLARBEAR data are presented here. These results represent the first measurement of C_L^{dd} using data from CMB polarization alone [42], and the first measurement of non-zero C_ℓ^{BB} [43].

Subsequent to the release of the POLARBEAR C_ℓ^{BB} spectra, the BICEP2 experiment, covering a different multipole (ℓ) range, presented C_ℓ^{BB} measurements with greater than 5σ evidence for primordial B-modes. We will compare the results from POLARBEAR and BICEP2 to the state of the field prior to March 2014, and briefly discuss the outlook for the future, paying particular attention to the role that POLARBEAR and its successors POLARBEAR-2 and the Simons Array will play.

The measurement of C_L^{dd} is presented in figure 6.1. The values from the three different patches are combined using their covariance matrices to form estimates of C_L^{dd} from $\langle d_{EB} d^*_{EB} \rangle_{\varphi_{\vec{L}}}$ and $\langle d_{EE} d^*_{EB} \rangle_{\varphi_{\vec{L}}}$ individually, which are also combined to form one single estimate. As described in section 4.9, the covariances are formed with and without the assumption of lensing, which affects the uncertainty of the final results as well as the final value via the different weighting of the estimators. Fitting a single value for the amplitude of observed lensing $\mathcal{A}_{dd}$, with a value of $\mathcal{A}_{dd} = 1$ being the WMAP-9 ΛCDM value, the measurement implies $\mathcal{A}_{dd} = 1.37 \pm .30 \pm 0.13$, where the ± 0.13 represents an estimate of the bounds on systematic errors, which are dominated by uncertainties in the abso-

lute gain calibration. Including the effects of lensing, the measurement implies $\mathcal{A}_{dd} = 1.06 \pm 0.47^{+0.32}_{-0.27}$ again with $^{+0.32}_{-0.27}$ representing bounds on the systematic uncertainties.

The significance for the rejection of $\mathcal{A}_{dd} = 0$ in the case of the un-lensed simulations indicates the significance with which the hypothesis of no gravitational lensing is rejected. We find that this data gives evidence for the presence of gravitational lensing (and gravitational lensing induced B-modes) at 4.2σ significance, including both statistical and systematic errors.

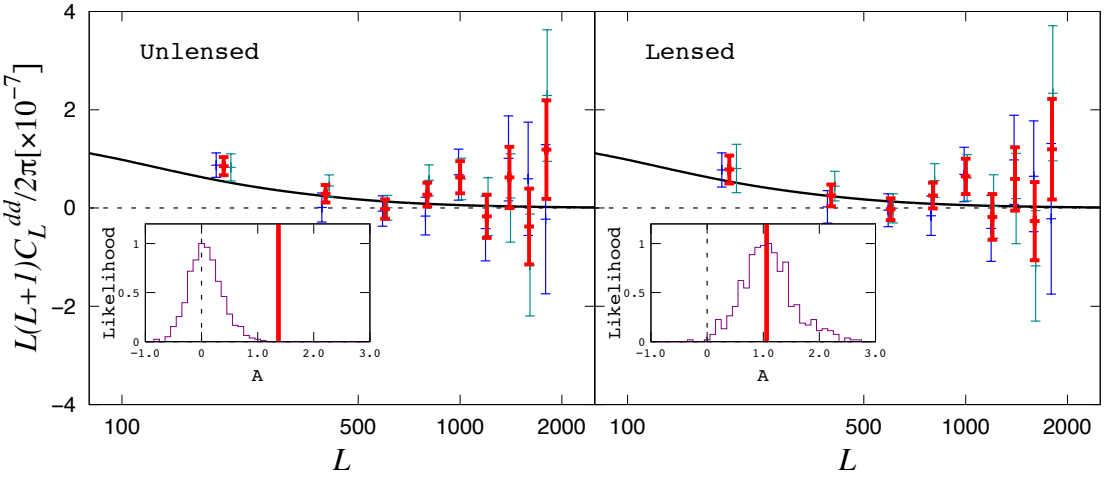

Figure 6.1: The C_L^{dd} power spectrum as measured by the first season of POLARBEAR observations. The left figure shows the results from simulations without lensing, and the right figure shows the results from simulations with lensing. $\langle d_{EE} d^*_{EB} \rangle_{\varphi_{\tilde{L}}}$ is shown in blue, $\langle d_{EB} d^*_{EB} \rangle_{\varphi_{\tilde{L}}}$ is shown in green, and the combination is shown in red. In each panel the prediction from ΛCDM is shown as a solid black line. Each inset shows the measured value of $\mathcal{A}_{dd}$ along with a histogram of values from 500 un-lensed (left) or lensed (right) simulations. Figure credit: Chang Feng

The POLARBEAR measurement of C_ℓ^{BB} is presented in figure 6.2 with data from all three patches combined. The data agree with the WMAP-9 ΛCDM value of C_ℓ^{BB} with a PTE of 42%. Fitting a single amplitude parameter $\mathcal{A}_{BB}$ between the ΛCDM model and the data, we find $\mathcal{A}_{BB}$=$1.12 \pm 0.61^{+0.04}_{-0.10} \pm 0.07$, where ± 0.61 is statistical, $^{+0.04}_{-0.10}$ is the additive portion of systematic errors, and ± 0.07 is the multiplicative portion of the systematic error.

The additive systematic error is computed as the per-bin linear sum of the

systematic errors presented in section 5.2, and the multiplicative uncertainties are computed as a quadrature sum. This constitutes a rejection of the no lensing-induced B-modes hypothesis at 97.5% significance, and was the first measurement of C_ℓ^{BB} with greater than 2σ significance. It remains the only $> 2\sigma$ significance measurement of C_ℓ^{BB} in the multipole range it covers.

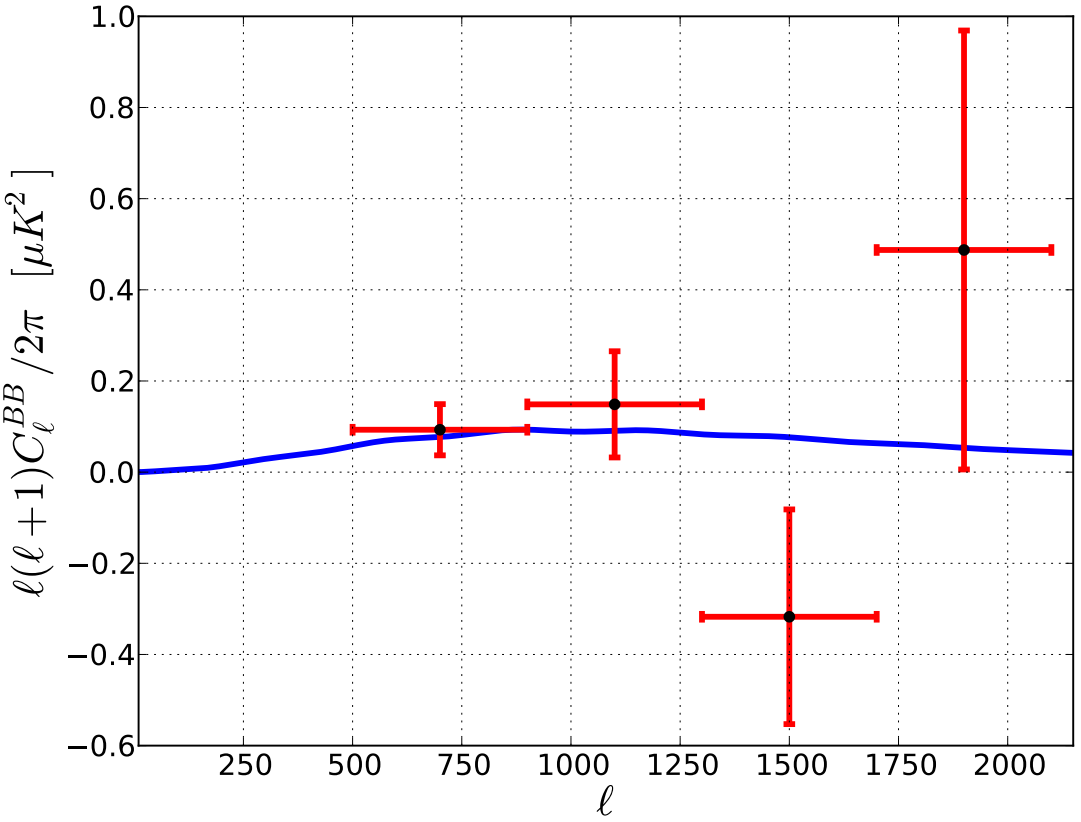

Figure 6.2: The C_ℓ^{BB} power spectrum as measured by the first season of POLARBEAR observations.

The negative band-power value in the $1300 < \ell < 1700$ bin is clearly non-physical. With the cross-spectrum estimator used for C_ℓ^{BB} the negative measurement indicates that power is anti-correlated in that ℓ bin between different days. With an overall PTE of 42% to the ΛCDM theory curve, we conclude that this fluctuation is entirely consistent with noise.

Further, under the hypothesis of no lensing, the estimates of C_L^{dd} and C_ℓ^{BB} would be uncorrelated, and combining the statistical significance of the two measurements can be combined as a quadrature sum. The combined significance for

the existence of gravitational-lensing induced B-modes is 4.7σ.

The BICEP2 measurement, POLARBEAR measurement, and constraints from previous experiments are shown in figure 6.3.

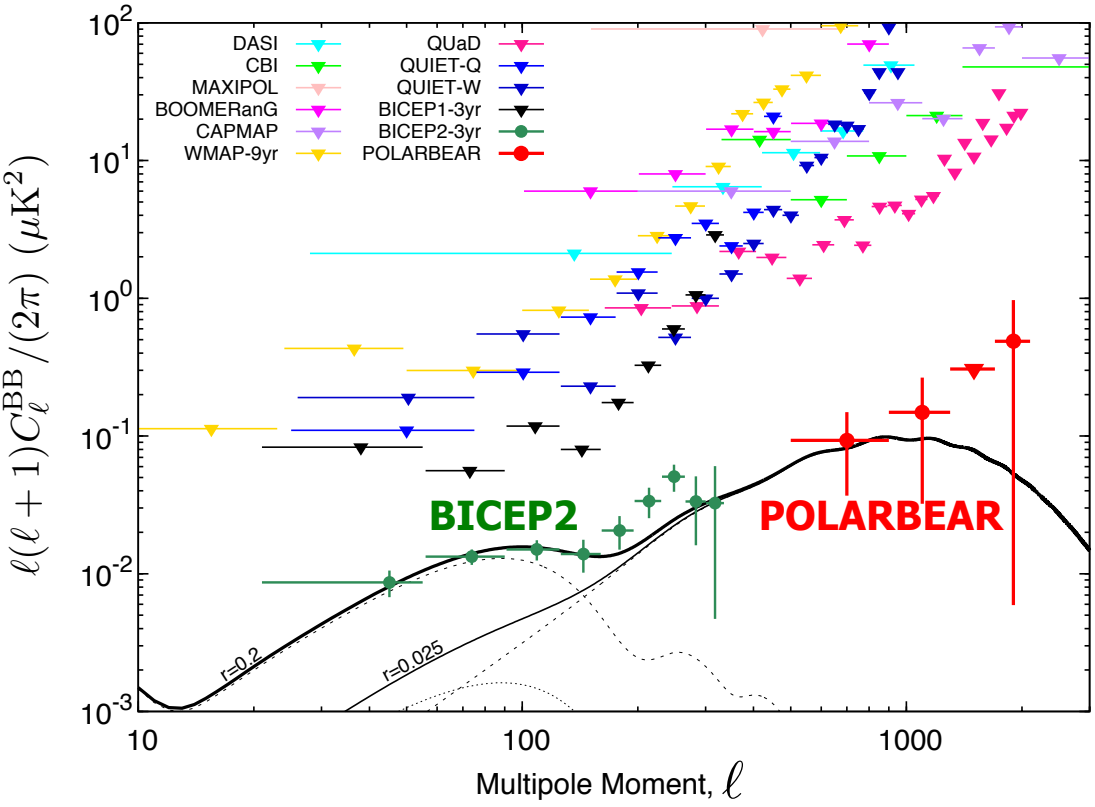

Figure 6.3: A comparison of C_ℓ^{BB} measurements. The value of the BICEP2 measurements are shown with their 1σ errors. The POLARBEAR points are shown with 1σ errors except for the third band power, which is shown with a 95% upper confidence limit given a positive prior. All other points are 95% upper limits.

The BICEP2 result marks the beginning of a new phase for CMB measurements. The result must be confirmed by other experiments using different regions of the sky and at different frequency bands to eliminate concerns about foreground contamination. A second peak in C_ℓ^{BB} should also be detectable at lower ℓ from the gravitational-wave background induced quadrupoles generating polarization during reionization.

With confirmation of the signal, the clear path forward is to both produce better constraints on the value of r and to attempt a measurement of the scale

dependence of the gravitational wave background, quantified by the tensor spectral index n_t. Simple models of inflation predict a specific relationship between r and n_t [75], making measurements of these quantities vital for testing the models.

In future observation seasons, scanning larger regions of the sky will give POLARBEAR the lower-ℓ sensitivity required to confirm the BICEP2 measurement. Because of its higher spacial resolution, it will also be able to extend measurements of the inflationary B-mode spectrum to higher multipoles as required for a measurement of n_t. To do this, the gravitational lensing B-mode signal must be separated from the primordial B-mode signal using a process called delensing. This technique relies on having high-resolution B-mode measurements, such as those POLARBEAR will make, and separates the two signals by reconstructing the lensing B-modes based on the induced non-Gaussian correlations [76, 77].

B-mode measurements on larger sky patches are also critical for improved measurements of C_L^{dd}. These measurements will be able to constrain the sum of neutrino masses [45] and the dark energy equation of state [78]. The combination of all of these possibilities make the CMB an incredible tool for future measurements of cosmology and fundamental physics.

The results from the first season of POLARBEAR observations demonstrate powerful control over systematic errors. Future expansions to the experiment, POLARBEAR-2 and the Simons Array, will increase the number of detectors by more than an order of magnitude and observe over three different spectral bands to better control errors introduced by foreground contamination. The lessons learned from POLARBEAR-1 will help to ensure the success of these instruments as we begin the era of B-mode cosmology.

Figure 6.1 was provided by Chang Feng and figure 6.3 by Yuji Chinone. The dissertation author made essential contributions to many aspects of both works.

Bibliography

[1] A. Einstein, "Die Feldgleichungen der Gravitation," *Sitzungsberichte der Königlich Preußischen Akademie der Wissenschaften (Berlin), Seite 844-847.*, pp. 844–847, 1915.

[2] BICEP2 Collaboration, P. A. R. Ade, R. W. Aikin, D. Barkats, S. J. Benton, C. A. Bischoff, J. J. Bock, J. A. Brevik, I. Buder, E. Bullock, C. D. Dowell, L. Duband, J. P. Filippini, S. Fliescher, S. R. Golwala, M. Halpern, M. Hasselfield, S. R. Hildebrandt, G. C. Hilton, V. V. Hristov, K. D. Irwin, K. S. Karkare, J. P. Kaufman, B. G. Keating, S. A. Kernasovskiy, J. M. Kovac, C. L. Kuo, E. M. Leitch, M. Lueker, P. Mason, C. B. Netterfield, H. T. Nguyen, R. O'Brient, R. W. Ogburn, IV, A. Orlando, C. Pryke, C. D. Reintsema, S. Richter, R. Schwarz, C. D. Sheehy, Z. K. Staniszewski, R. V. Sudiwala, G. P. Teply, J. E. Tolan, A. D. Turner, A. G. Vieregg, C. L. Wong, and K. W. Yoon, "BICEP2 I: Detection Of B-mode Polarization at Degree Angular Scales," *ArXiv e-prints*, Mar. 2014.

[3] G. Fuller. Lectures and personal communication.

[4] C. W. Misner, K. S. Thorne, and J. A. Wheeler, *Gravitation.* 1973.

[5] S. Dodelson, *Modern cosmology.* 2003.

[6] E. Hubble, "A Relation between Distance and Radial Velocity among Extra-Galactic Nebulae," *Proceedings of the National Academy of Science*, vol. 15, pp. 168–173, Mar. 1929.

[7] A. Friedmann, "On the Curvature of Space," *General Relativity and Gravitation*, vol. 31, p. 1991, Dec. 1999.

[8] A. Coc, E. Vangioni-Flam, P. Descouvemont, A. Adahchour, and C. Angulo, "Updated Big Bang Nucleosynthesis Compared with Wilkinson Microwave Anisotropy Probe Observations and the Abundance of Light Elements," *ApJ*, vol. 600, pp. 544–552, Jan. 2004.

[9] G. Gamow, "The Evolution of the Universe," *Nature*, vol. 162, pp. 680–682, Oct. 1948.

[10] R. A. Alpher and R. Herman, "Evolution of the Universe," *Nature*, vol. 162, pp. 774–775, Nov. 1948.

[11] A. A. Penzias, "The origin of the elements," *Reviews of Modern Physics*, vol. 51, pp. 425–431, July 1979.

[12] A. G. Doroshkevich and I. D. Novikov, "Mean Density of Radiation in the Metagalaxy and Certain Problems in Relativistic Cosmology," *Soviet Physics Doklady*, vol. 9, p. 111, Aug. 1964.

[13] A. A. Penzias and R. W. Wilson, "A Measurement of Excess Antenna Temperature at 4080 Mc/s.," *ApJ*, vol. 142, pp. 419–421, July 1965.

[14] R. H. Dicke, P. J. E. Peebles, P. G. Roll, and D. T. Wilkinson, "Cosmic Black-Body Radiation.," *ApJ*, vol. 142, pp. 414–419, July 1965.

[15] J. A. Peacock, *Cosmological Physics*. Jan. 1999.

[16] R. K. Sachs and A. M. Wolfe, "Perturbations of a Cosmological Model and Angular Variations of the Microwave Background," *ApJ*, vol. 147, p. 73, Jan. 1967.

[17] G. F. Smoot, C. L. Bennett, A. Kogut, E. L. Wright, J. Aymon, N. W. Boggess, E. S. Cheng, G. de Amici, S. Gulkis, M. G. Hauser, G. Hinshaw, P. D. Jackson, M. Janssen, E. Kaita, T. Kelsall, P. Keegstra, C. Lineweaver, K. Loewenstein, P. Lubin, J. Mather, S. S. Meyer, S. H. Moseley, T. Murdock, L. Rokke, R. F. Silverberg, L. Tenorio, R. Weiss, and D. T. Wilkinson, "Structure in the COBE differential microwave radiometer first-year maps," *ApJ Letters*, vol. 396, pp. L1–L5, Sept. 1992.

[18] J. C. Mather, E. S. Cheng, D. A. Cottingham, R. E. Eplee, Jr., D. J. Fixsen, T. Hewagama, R. B. Isaacman, K. A. Jensen, S. S. Meyer, P. D. Noerdlinger, S. M. Read, L. P. Rosen, R. A. Shafer, E. L. Wright, C. L. Bennett, N. W. Boggess, M. G. Hauser, T. Kelsall, S. H. Moseley, Jr., R. F. Silverberg, G. F. Smoot, R. Weiss, and D. T. Wilkinson, "Measurement of the cosmic microwave background spectrum by the COBE FIRAS instrument," *ApJ*, vol. 420, pp. 439–444, Jan. 1994.

[19] D. J. Fixsen, E. S. Cheng, J. M. Gales, J. C. Mather, R. A. Shafer, and E. L. Wright, "The Cosmic Microwave Background Spectrum from the Full COBE FIRAS Data Set," *ApJ*, vol. 473, p. 576, Dec. 1996.

[20] S. Bashinsky and E. Bertschinger, "Dynamics of cosmological perturbations in position space," *Phys. Rev. D*, vol. 65, p. 123008, Jun 2002.

[21] S. Bashinsky and E. Bertschinger, "Position-space description of the cosmic microwave background and its temperature correlation function," *Phys. Rev. Lett.*, vol. 87, p. 081301, Aug 2001.

[22] C.-P. Ma and E. Bertschinger, "Cosmological Perturbation Theory in the Synchronous and Conformal Newtonian Gauges," *ApJ*, vol. 455, p. 7, Dec. 1995.

[23] U. Seljak and M. Zaldarriaga, "A Line-of-Sight Integration Approach to Cosmic Microwave Background Anisotropies," *ApJ*, vol. 469, p. 437, Oct. 1996.

[24] A. Lewis and A. Challinor, "Evolution of cosmological dark matter perturbations," *Phys. Rev. D*, vol. 66, p. 023531, July 2002.

[25] A. Lewis, A. Challinor, and A. Lasenby, "Efficient Computation of Cosmic Microwave Background Anisotropies in Closed Friedmann-Robertson-Walker Models," *ApJ*, vol. 538, pp. 473–476, Aug. 2000.

[26] P. A. R. Ade, N. Aghanim, C. Armitage-Caplan, M. Arnaud, M. Ashdown, F. Atrio-Barandela, J. Aumont, C. Baccigalupi, A. J. Banday, R. B. Barreiro, J. G. Bartlett, E. Battaner, K. Benabed, A. BenoÃőt, A. Benoit-Levy, J. Bernard, M. Bersanelli, P. Bielewicz, J. Bobin, J. J. Bock, A. Bonaldi, J. R. Bond, J. Borrill, F. R. Bouchet, M. Bridges, M. Bucher, C. Burigana, R. C. Butler, E. Calabrese, B. Cappellini, J. Cardoso, A. Catalano, A. Challinor, A. Chamballu, R. Chary, X. Chen, L. Chiang, H. C. Chiang, P. R. Christensen, S. Church, D. L. Clements, S. Colombi, L. P. L. Colombo, F. Couchot, A. Coulais, B. P. Crill, A. Curto, F. Cuttaia, L. Danese, R. D. Davies, R. J. Davis, P. de Bernardis, A. de Rosa, G. de Zotti, J. Delabrouille, J. Delouis, F. Desert, C. Dickinson, J. M. Diego, K. Dolag, H. Dole, S. Donzelli, O. Dore, M. Douspis, J. Dunkley, X. Dupac, G. Efstathiou, F. Elsner, T. A. EnÃ§lin, H. K. Eriksen, F. Finelli, O. Forni, M. Frailis, A. A. Fraisse, E. Franceschi, T. C. Gaier, S. Galeotta, S. Galli, K. Ganga, M. Giard, G. Giardino, Y. Giraud-Heraud, E. Gjerlow, J. Gonzalez-Nuevo, K. M. Gorski, S. Gratton, A. Gregorio, A. Gruppuso, J. E. Gudmundsson, J. Haissinski, J. Hamann, F. K. Hansen, D. Hanson, D. Harrison, S. Henrot-Versille, C. Hernandez-Monteagudo, D. Herranz, S. R. Hildebrandt, E. Hivon, M. Hobson, W. A. Holmes, A. Hornstrup, Z. Hou, W. Hovest, K. M. Huffenberger, T. R. Jaffe, A. H. Jaffe, J. Jewell, W. C. Jones, M. Juvela, E. Keihanen, R. Keskitalo, T. S. Kisner, R. Kneissl, J. Knoche, L. Knox, M. Kunz, H. Kurki-Suonio, G. Lagache, A. Lahteenmaki, J. Lamarre, A. Lasenby, M. Lattanzi, R. J. Laureijs, C. R. Lawrence, S. Leach, J. P. Leahy, R. Leonardi, J. Leon-Tavares, J. Lesgourgues, A. Lewis, M. Liguori, P. B. Lilje, M. Linden-Vornle, M. Lopez-Caniego, P. M. Lubin, J. F. Macias-Perez, B. Maffei, D. Maino, N. Mandolesi, M. Maris, D. J. Marshall, P. G. Martin, E. Martinez-Gonzalez, S. Masi, S. Matarrese, F. Matthai, P. Mazzotta, P. R. Meinhold, A. Melchiorri,

J. Melin, L. Mendes, E. Menegoni, A. Mennella, M. Migliaccio, M. Millea, S. Mitra, M. Miville-Deschenes, A. Moneti, L. Montier, G. Morgante, D. Mortlock, A. Moss, D. Munshi, P. Naselsky, F. Nati, P. Natoli, C. B. Netterfield, H. U. Norgaard-Nielsen, F. Noviello, D. Novikov, I. Novikov, I. J. O'Dwyer, S. Osborne, C. A. Oxborrow, F. Paci, L. Pagano, F. Pajot, D. Paoletti, B. Partridge, F. Pasian, G. Patanchon, D. Pearson, T. J. Pearson, H. V. Peiris, O. Perdereau, L. Perotto, F. Perrotta, V. Pettorino, F. Piacentini, M. Piat, E. Pierpaoli, D. Pietrobon, S. Plaszczynski, P. Platania, E. Pointecouteau, G. Polenta, N. Ponthieu, L. Popa, T. Poutanen, G. W. Pratt, G. Prezeau, S. Prunet, J. Puget, J. P. Rachen, W. T. Reach, R. Rebolo, M. Reinecke, M. Remazeilles, C. Renault, S. Ricciardi, T. Riller, I. Ristorcelli, G. Rocha, C. Rosset, G. Roudier, M. Rowan-Robinson, J. A. Rubino-Martin, B. Rusholme, M. Sandri, D. Santos, M. Savelainen, G. Savini, D. Scott, M. D. Seiffert, E. P. S. Shellard, L. D. Spencer, J. Starck, V. Stolyarov, R. Stompor, R. Sudiwala, R. Sunyaev, F. Sureau, D. Sutton, A. Suur-Uski, J. Sygnet, J. A. Tauber, D. Tavagnacco, L. Terenzi, L. Toffolatti, M. Tomasi, M. Tristram, M. Tucci, J. Tuovinen, M. Turler, G. Umana, L. Valenziano, J. Valiviita, B. V. Tent, P. Vielva, F. Villa, N. Vittorio, L. A. Wade, B. D. Wandelt, I. K. Wehus, M. White, S. D. M. White, A. Wilkinson, D. Yvon, A. Zacchei, and A. Zonca, "Planck 2013 results. XXII. Constraints on inflation," *ArXiv e-prints*, Mar. 2013.

[27] B. Bassett and R. Hlozek, *Baryon acoustic oscillations*, p. 246. 2010.

[28] P. A. R. Ade, N. Aghanim, C. Armitage-Caplan, M. Arnaud, M. Ashdown, F. Atrio-Barandela, J. Aumont, C. Baccigalupi, A. J. Banday, R. B. Barreiro, J. G. Bartlett, E. Battaner, K. Benabed, A. BenoÃőt, A. Benoit-Levy, J. Bernard, M. Bersanelli, P. Bielewicz, J. Bobin, J. J. Bock, A. Bonaldi, J. R. Bond, J. Borrill, F. R. Bouchet, M. Bridges, M. Bucher, C. Burigana, R. C. Butler, E. Calabrese, B. Cappellini, J. Cardoso, A. Catalano, A. Challinor, A. Chamballu, R. Chary, X. Chen, L. Chiang, H. C. Chiang, P. R. Christensen, S. Church, D. L. Clements, S. Colombi, L. P. L. Colombo, F. Couchot, A. Coulais, B. P. Crill, A. Curto, F. Cuttaia, L. Danese, R. D. Davies, R. J. Davis, P. de Bernardis, A. de Rosa, G. de Zotti, J. Delabrouille, J. Delouis, F. Desert, C. Dickinson, J. M. Diego, K. Dolag, H. Dole, S. Donzelli, O. Dore, M. Douspis, J. Dunkley, X. Dupac, G. Efstathiou, F. Elsner, T. A. EnÃ§lin, H. K. Eriksen, F. Finelli, O. Forni, M. Frailis, A. A. Fraisse, E. Franceschi, T. C. Gaier, S. Galeotta, S. Galli, K. Ganga, M. Giard, G. Giardino, Y. Giraud-Heraud, E. Gjerlow, J. Gonzalez-Nuevo, K. M. Gorski, S. Gratton, A. Gregorio, A. Gruppuso, J. E. Gudmundsson, J. Haissinski, J. Hamann, F. K. Hansen, D. Hanson, D. Harrison, S. Henrot-Versille, C. Hernandez-Monteagudo, D. Herranz, S. R. Hildebrandt, E. Hivon, M. Hobson, W. A. Holmes, A. Hornstrup, Z. Hou, W. Hovest, K. M. Huffenberger, T. R. Jaffe, A. H. Jaffe, J. Jewell, W. C. Jones, M. Juvela, E. Keihanen,

R. Keskitalo, T. S. Kisner, R. Kneissl, J. Knoche, L. Knox, M. Kunz, H. Kurki-Suonio, G. Lagache, A. Lahteenmaki, J. Lamarre, A. Lasenby, M. Lattanzi, R. J. Laureijs, C. R. Lawrence, S. Leach, J. P. Leahy, R. Leonardi, J. Leon-Tavares, J. Lesgourgues, A. Lewis, M. Liguori, P. B. Lilje, M. Linden-Vornle, M. Lopez-Caniego, P. M. Lubin, J. F. Macias-Perez, B. Maffei, D. Maino, N. Mandolesi, M. Maris, D. J. Marshall, P. G. Martin, E. Martinez-Gonzalez, S. Masi, S. Matarrese, F. Matthai, P. Mazzotta, P. R. Meinhold, A. Melchiorri, J. Melin, L. Mendes, E. Menegoni, A. Mennella, M. Migliaccio, M. Millea, S. Mitra, M. Miville-Deschenes, A. Moneti, L. Montier, G. Morgante, D. Mortlock, A. Moss, D. Munshi, P. Naselsky, F. Nati, P. Natoli, C. B. Netterfield, H. U. Norgaard-Nielsen, F. Noviello, D. Novikov, I. Novikov, I. J. O'Dwyer, S. Osborne, C. A. Oxborrow, F. Paci, L. Pagano, F. Pajot, D. Paoletti, B. Partridge, F. Pasian, G. Patanchon, D. Pearson, T. J. Pearson, H. V. Peiris, O. Perdereau, L. Perotto, F. Perrotta, V. Pettorino, F. Piacentini, M. Piat, E. Pierpaoli, D. Pietrobon, S. Plaszczynski, P. Platania, E. Pointecouteau, G. Polenta, N. Ponthieu, L. Popa, T. Poutanen, G. W. Pratt, G. Prezeau, S. Prunet, J. Puget, J. P. Rachen, W. T. Reach, R. Rebolo, M. Reinecke, M. Remazeilles, C. Renault, S. Ricciardi, T. Riller, I. Ristorcelli, G. Rocha, C. Rosset, G. Roudier, M. Rowan-Robinson, J. A. Rubino-Martin, B. Rusholme, M. Sandri, D. Santos, M. Savelainen, G. Savini, D. Scott, M. D. Seiffert, E. P. S. Shellard, L. D. Spencer, J. Starck, V. Stolyarov, R. Stompor, R. Sudiwala, R. Sunyaev, F. Sureau, D. Sutton, A. Suur-Uski, J. Sygnet, J. A. Tauber, D. Tavagnacco, L. Terenzi, L. Toffolatti, M. Tomasi, M. Tristram, M. Tucci, J. Tuovinen, M. Turler, G. Umana, L. Valenziano, J. Valiviita, B. V. Tent, P. Vielva, F. Villa, N. Vittorio, L. A. Wade, B. D. Wandelt, I. K. Wehus, M. White, S. D. M. White, A. Wilkinson, D. Yvon, A. Zacchei, and A. Zonca, "Planck 2013 Results. XXIV. Constraints on primordial non-Gaussianity," *ArXiv e-prints*, Mar. 2013.

[29] G. Hinshaw, D. Larson, E. Komatsu, D. N. Spergel, C. L. Bennett, J. Dunkley, M. R. Nolta, M. Halpern, R. S. Hill, N. Odegard, L. Page, K. M. Smith, J. L. Weiland, B. Gold, N. Jarosik, A. Kogut, M. Limon, S. S. Meyer, G. S. Tucker, E. Wollack, and E. L. Wright, "Nine-year Wilkinson Microwave Anisotropy Probe (WMAP) Observations: Cosmological Parameter Results," , vol. 208, p. 19, Oct. 2013.

[30] R. Keisler, C. L. Reichardt, K. A. Aird, B. A. Benson, L. E. Bleem, J. E. Carlstrom, C. L. Chang, H. M. Cho, T. M. Crawford, A. T. Crites, T. de Haan, M. A. Dobbs, J. Dudley, E. M. George, N. W. Halverson, G. P. Holder, W. L. Holzapfel, S. Hoover, Z. Hou, J. D. Hrubes, M. Joy, L. Knox, A. T. Lee, E. M. Leitch, M. Lueker, D. Luong-Van, J. J. McMahon, J. Mehl, S. S. Meyer, M. Millea, J. J. Mohr, T. E. Montroy, T. Natoli, S. Padin, T. Plagge, C. Pryke, J. E. Ruhl, K. K. Schaffer, L. Shaw, E. Shirokoff, H. G. Spieler, Z. Staniszewski, A. A. Stark, K. Story, A. van Engelen, K. Vanderlinde, J. D.

Vieira, R. Williamson, and O. Zahn, "A Measurement of the Damping Tail of the Cosmic Microwave Background Power Spectrum with the South Pole Telescope," *Astrophysical Journal*, vol. 743, p. 28, Dec. 2011.

[31] D. J. Eisenstein, I. Zehavi, D. W. Hogg, R. Scoccimarro, M. R. Blanton, R. C. Nichol, R. Scranton, H.-J. Seo, M. Tegmark, Z. Zheng, S. F. Anderson, J. Annis, N. Bahcall, J. Brinkmann, S. Burles, F. J. Castander, A. Connolly, I. Csabai, M. Doi, M. Fukugita, J. A. Frieman, K. Glazebrook, J. E. Gunn, J. S. Hendry, G. Hennessy, Z. Ivezić, S. Kent, G. R. Knapp, H. Lin, Y.-S. Loh, R. H. Lupton, B. Margon, T. A. McKay, A. Meiksin, J. A. Munn, A. Pope, M. W. Richmond, D. Schlegel, D. P. Schneider, K. Shimasaku, C. Stoughton, M. A. Strauss, M. SubbaRao, A. S. Szalay, I. Szapudi, D. L. Tucker, B. Yanny, and D. G. York, "Detection of the Baryon Acoustic Peak in the Large-Scale Correlation Function of SDSS Luminous Red Galaxies," *Astrophysical Journal*, vol. 633, pp. 560–574, Nov. 2005.

[32] J. D. Jackson, *Classical Electrodynamics*. New York, NY: Wiley, 3rd ed. ed.

[33] M. Zaldarriaga, "Nature of the E-B decomposition of CMB polarization," *Physical Review D*, vol. 64, p. 103001, Nov. 2001.

[34] J. M. Kovac, E. M. Leitch, C. Pryke, J. E. Carlstrom, N. W. Halverson, and W. L. Holzapfel, "Detection of polarization in the cosmic microwave background using DASI," *Nature*, vol. 420, pp. 772–787, Dec. 2002.

[35] M. Kamionkowski, A. Kosowsky, and A. Stebbins, "A Probe of Primordial Gravity Waves and Vorticity," *Physical Review Letters*, vol. 78, pp. 2058–2061, Mar. 1997.

[36] U. Seljak and M. Zaldarriaga, "Signature of Gravity Waves in the Polarization of the Microwave Background," *Physical Review Letters*, vol. 78, pp. 2054–2057, Mar. 1997.

[37] M. Zaldarriaga and U. Seljak, "Gravitational lensing effect on cosmic microwave background polarization," *Physical Review D*, vol. 58, p. 023003, July 1998.

[38] W. Hu and T. Okamoto, "Mass Reconstruction with Cosmic Microwave Background Polarization," *Astrophysical Journal*, vol. 574, pp. 566–574, Aug. 2002.

[39] S. Dodelson, "How much can we learn about the physics of inflation?," *ArXiv e-prints*, Mar. 2014.

[40] D. Hanson, S. Hoover, A. Crites, P. A. R. Ade, K. A. Aird, J. E. Austermann, J. A. Beall, A. N. Bender, B. A. Benson, L. E. Bleem, J. J. Bock, J. E. Carlstrom, C. L. Chang, H. C. Chiang, H.-M. Cho, A. Conley, T. M. Crawford,

T. de Haan, M. A. Dobbs, W. Everett, J. Gallicchio, J. Gao, E. M. George, N. W. Halverson, N. Harrington, J. W. Henning, G. C. Hilton, G. P. Holder, W. L. Holzapfel, J. D. Hrubes, N. Huang, J. Hubmayr, K. D. Irwin, R. Keisler, L. Knox, A. T. Lee, E. Leitch, D. Li, C. Liang, D. Luong-Van, G. Marsden, J. J. McMahon, J. Mehl, S. S. Meyer, L. Mocanu, T. E. Montroy, T. Natoli, J. P. Nibarger, V. Novosad, S. Padin, C. Pryke, C. L. Reichardt, J. E. Ruhl, B. R. Saliwanchik, J. T. Sayre, K. K. Schaffer, B. Schulz, G. Smecher, A. A. Stark, K. T. Story, C. Tucker, K. Vanderlinde, J. D. Vieira, M. P. Viero, G. Wang, V. Yefremenko, O. Zahn, and M. Zemcov, "Detection of B-Mode Polarization in the Cosmic Microwave Background with Data from the South Pole Telescope," *Physical Review Letters*, vol. 111, p. 141301, Oct. 2013.

[41] P. Ade, Y. Akiba, E. Anthony, A. K. Arnold, M. Atlas, D. Barron, D. Boettger, J. Borrill, C. Borys, S. Chapman, Y. Chinone, M. Dobbs, T. Elleflot, J. Errard, G. Fabbian, C. Feng, D. Flanigan, A. Gilbert, W. Grainger, W. Halverson, N. M. Hasegawa, K. Hattori, M. Hazumi, L. Holzapfel, W. Y. Hori, J. Howard, P. Hyland, Y. Inoue, C. Jaehnig, G. A. Jaffe, B. Keating, Z. Kermish, R. Keskitalo, T. Kisner, M. Le Jeune, T. Lee, A. M. Leitch, E. E. Linder, M. Lungu, F. Matsuda, T. Matsumura, X. Meng, J. Miller, N. H. Morii, S. Moyerman, J. Myers, M. M. Navaroli, H. Nishino, H. Paar, J. Peloton, D. Poletti, E. Quealy, G. Rebeiz, L. Reichardt, C. L. Richards, P. C. Ross, K. Rotermund, I. Schanning, E. Schenck, D. D. Sherwin, B. A. Shimizu, C. Shimmin, M. Shimon, P. Siritanasak, G. Smecher, H. Spieler, N. Stebor, B. Steinbach, R. Stompor, A. Suzuki, S. Takakura, A. Tikhomirov, T. Tomaru, B. Wilson, A. Yadav, and O. Zahn, "Evidence for gravitational lensing of the cosmic microwave background polarization from cross-correlation with the cosmic infrared background," *Phys. Rev. Lett.*, vol. 112, p. 131302, Apr 2014.

[42] Polarbear Collaboration, P. A. R. Ade, Y. Akiba, A. E. Anthony, K. Arnold, D. Barron, D. Boettger, J. Borrill, S. Chapman, Y. Chinone, M. Dobbs, T. Elleflot, J. Errard, G. Fabbian, C. Feng, D. Flanigan, A. Gilbert, W. Grainger, N. W. Halverson, M. Hasegawa, K. Hattori, M. Hazumi, W. L. Holzapfel, Y. Hori, J. Howard, P. Hyland, Y. Inoue, G. C. Jaehnig, A. Jaffe, B. Keating, Z. Kermish, R. Keskitalo, T. Kisner, M. Le Jeune, A. T. Lee, E. Linder, M. Lungu, F. Matsuda, T. Matsumura, X. Meng, N. J. Miller, H. Morii, S. Moyerman, M. J. Myers, M. Navaroli, H. Nishino, H. Paar, J. Peloton, E. Quealy, G. Rebeiz, C. L. Reichardt, P. L. Richards, C. Ross, I. Schanning, D. E. Schenck, B. Sherwin, A. Shimizu, C. Shimmin, M. Shimon, P. Siritanasak, G. Smecher, H. Spieler, N. Stebor, B. Steinbach, R. Stompor, A. Suzuki, S. Takakura, T. Tomaru, B. Wilson, A. Yadav, and O. Zahn, "Gravitational Lensing of Cosmic Microwave Background Polarization," *ArXiv e-prints*, Dec. 2013.

[43] The POLARBEAR Collaboration, P. A. R. Ade, Y. Akiba, A. E. Anthony, K. Arnold, M. Atlas, D. Barron, D. Boettger, J. Borrill, S. Chapman, Y. Chinone, M. Dobbs, T. Elleflot, J. Errard, G. Fabbian, C. Feng, D. Flanigan, A. Gilbert, W. Grainger, N. W. Halverson, M. Hasegawa, K. Hattori, M. Hazumi, W. L. Holzapfel, Y. Hori, J. Howard, P. Hyland, Y. Inoue, G. C. Jaehnig, A. H. Jaffe, B. Keating, Z. Kermish, R. Keskitalo, T. Kisner, M. Le Jeune, A. T. Lee, E. M. Leitch, E. Linder, M. Lungu, F. Matsuda, T. Matsumura, X. Meng, N. J. Miller, H. Morii, S. Moyerman, M. J. Myers, M. Navaroli, H. Nishino, H. Paar, J. Peloton, D. Poletti, E. Quealy, G. Rebeiz, C. L. Reichardt, P. L. Richards, C. Ross, I. Schanning, D. E. Schenck, B. D. Sherwin, A. Shimizu, C. Shimmin, M. Shimon, P. Siritanasak, G. Smecher, H. Spieler, N. Stebor, B. Steinbach, R. Stompor, A. Suzuki, S. Takakura, T. Tomaru, B. Wilson, A. Yadav, and O. Zahn, "A Measurement of the Cosmic Microwave Background B-Mode Polarization Power Spectrum at Sub-Degree Scales with POLARBEAR," *ArXiv e-prints*, Mar. 2014.

[44] A. Challinor and A. Lewis, "Lensed CMB power spectra from all-sky correlation functions," *Physical Review D*, vol. 71, p. 103010, May 2005.

[45] K. N. Abazajian, K. Arnold, J. Austermann, B. A. Benson, C. Bischoff, J. Bock, J. R. Bond, J. Borrill, E. Calabrese, J. E. Carlstrom, C. S. Carvalho, C. L. Chang, H. C. Chiang, S. Church, A. Cooray, T. M. Crawford, K. S. Dawson, S. Das, M. J. Devlin, M. Dobbs, S. Dodelson, O. Dore, J. Dunkley, J. Errard, A. Fraisse, J. Gallicchio, N. W. Halverson, S. Hanany, S. R. Hildebrandt, A. Hincks, R. Hlozek, G. Holder, W. L. Holzapfel, K. Honscheid, W. Hu, J. Hubmayr, K. Irwin, W. C. Jones, M. Kamionkowski, B. Keating, R. Keisler, L. Knox, E. Komatsu, J. Kovac, C.-L. Kuo, C. Lawrence, A. T. Lee, E. Leitch, E. Linder, P. Lubin, J. McMahon, A. Miller, L. Newburgh, M. D. Niemack, H. Nguyen, H. T. Nguyen, L. Page, C. Pryke, C. L. Reichardt, J. E. Ruhl, N. Sehgal, U. Seljak, J. Sievers, E. Silverstein, A. Slosar, K. M. Smith, D. Spergel, S. T. Staggs, A. Stark, R. Stompor, A. G. Vieregg, G. Wang, S. Watson, E. J. Wollack, W. L. K. Wu, K. W. Yoon, and O. Zahn, "Neutrino Physics from the Cosmic Microwave Background and Large Scale Structure," *ArXiv e-prints*, Sept. 2013.

[46] M. Shimon, B. Keating, N. Ponthieu, and E. Hivon, "CMB polarization systematics due to beam asymmetry: Impact on inflationary science," *Physical Review D*, vol. 77, p. 083003, Apr. 2008.

[47] Y. Mizugutch, M. Akagawa, and H. Yokoi, "Offset dual reflector antenna," in *Antennas and Propagation Society International Symposium, 1976*, vol. 14, pp. 2–5, 1976.

[48] C. Dragone, "Offset multireflector antennas with perfect pattern symmetry

and polarization discrimination," *Bell System Technical Journal*, vol. 57, no. 7, pp. 2663–2684, 1978.

[49] H. Tran, A. Lee, S. Hanany, M. Milligan, and T. Renbarger, "Comparison of the crossed and the gregorian mizuguchi-dragone for wide-field millimeter-wave astronomy," *Appl. Opt.*, vol. 47, pp. 103–109, Jan 2008.

[50] Z. D. Kermish, P. Ade, A. Anthony, K. Arnold, D. Barron, D. Boettger, J. Borrill, S. Chapman, Y. Chinone, M. A. Dobbs, J. Errard, G. Fabbian, D. Flanigan, G. Fuller, A. Ghribi, W. Grainger, N. Halverson, M. Hasegawa, K. Hattori, M. Hazumi, W. L. Holzapfel, J. Howard, P. Hyland, A. Jaffe, B. Keating, T. Kisner, A. T. Lee, M. Le Jeune, E. Linder, M. Lungu, F. Matsuda, T. Matsumura, X. Meng, N. J. Miller, H. Morii, S. Moyerman, M. J. Myers, H. Nishino, H. Paar, E. Quealy, C. L. Reichardt, P. L. Richards, C. Ross, A. Shimizu, M. Shimon, C. Shimmin, M. Sholl, P. Siritanasak, H. Spieler, N. Stebor, B. Steinbach, R. Stompor, A. Suzuki, T. Tomaru, C. Tucker, and O. Zahn, "The POLARBEAR experiment," in *Society of Photo-Optical Instrumentation Engineers (SPIE) Conference Series*, vol. 8452 of *Society of Photo-Optical Instrumentation Engineers (SPIE) Conference Series*, Sept. 2012.

[51] P. A. R. Ade, N. Aghanim, C. Armitage-Caplan, M. Arnaud, M. Ashdown, F. Atrio-Barandela, J. Aumont, C. Baccigalupi, A. J. Banday, R. B. Barreiro, J. G. Bartlett, E. Battaner, K. Benabed, A. BenoÃőt, A. Benoit-Levy, J. Bernard, M. Bersanelli, P. Bielewicz, J. Bobin, J. J. Bock, A. Bonaldi, J. R. Bond, J. Borrill, F. R. Bouchet, M. Bridges, M. Bucher, C. Burigana, R. C. Butler, E. Calabrese, B. Cappellini, J. Cardoso, A. Catalano, A. Challinor, A. Chamballu, R. Chary, X. Chen, L. Chiang, H. C. Chiang, P. R. Christensen, S. Church, D. L. Clements, S. Colombi, L. P. L. Colombo, F. Couchot, A. Coulais, B. P. Crill, A. Curto, F. Cuttaia, L. Danese, R. D. Davies, R. J. Davis, P. de Bernardis, A. de Rosa, G. de Zotti, J. Delabrouille, J. Delouis, F. Desert, C. Dickinson, J. M. Diego, K. Dolag, H. Dole, S. Donzelli, O. Dore, M. Douspis, J. Dunkley, X. Dupac, G. Efstathiou, F. Elsner, T. A. EnÃ§lin, H. K. Eriksen, F. Finelli, O. Forni, M. Frailis, A. A. Fraisse, E. Franceschi, T. C. Gaier, S. Galeotta, S. Galli, K. Ganga, M. Giard, G. Giardino, Y. Giraud-Heraud, E. Gjerlow, J. Gonzalez-Nuevo, K. M. Gorski, S. Gratton, A. Gregorio, A. Gruppuso, J. E. Gudmundsson, J. Haissinski, J. Hamann, F. K. Hansen, D. Hanson, D. Harrison, S. Henrot-Versille, C. Hernandez-Monteagudo, D. Herranz, S. R. Hildebrandt, E. Hivon, M. Hobson, W. A. Holmes, A. Hornstrup, Z. Hou, W. Hovest, K. M. Huffenberger, T. R. Jaffe, A. H. Jaffe, J. Jewell, W. C. Jones, M. Juvela, E. Keihanen, R. Keskitalo, T. S. Kisner, R. Kneissl, J. Knoche, L. Knox, M. Kunz, H. Kurki-Suonio, G. Lagache, A. Lahteenmaki, J. Lamarre, A. Lasenby, M. Lattanzi, R. J. Laureijs, C. R. Lawrence, S. Leach, J. P. Leahy, R. Leonardi, J. Leon-Tavares, J. Lesgourgues, A. Lewis, M. Liguori, P. B. Lilje, M. Linden-Vornle,

M. Lopez-Caniego, P. M. Lubin, J. F. Macias-Perez, B. Maffei, D. Maino, N. Mandolesi, M. Maris, D. J. Marshall, P. G. Martin, E. Martinez-Gonzalez, S. Masi, S. Matarrese, F. Matthai, P. Mazzotta, P. R. Meinhold, A. Melchiorri, J. Melin, L. Mendes, E. Menegoni, A. Mennella, M. Migliaccio, M. Millea, S. Mitra, M. Miville-Deschenes, A. Moneti, L. Montier, G. Morgante, D. Mortlock, A. Moss, D. Munshi, P. Naselsky, F. Nati, P. Natoli, C. B. Netterfield, H. U. Norgaard-Nielsen, F. Noviello, D. Novikov, I. Novikov, I. J. O'Dwyer, S. Osborne, C. A. Oxborrow, F. Paci, L. Pagano, F. Pajot, D. Paoletti, B. Partridge, F. Pasian, G. Patanchon, D. Pearson, T. J. Pearson, H. V. Peiris, O. Perdereau, L. Perotto, F. Perrotta, V. Pettorino, F. Piacentini, M. Piat, E. Pierpaoli, D. Pietrobon, S. Plaszczynski, P. Platania, E. Pointecouteau, G. Polenta, N. Ponthieu, L. Popa, T. Poutanen, G. W. Pratt, G. Prezeau, S. Prunet, J. Puget, J. P. Rachen, W. T. Reach, R. Rebolo, M. Reinecke, M. Remazeilles, C. Renault, S. Ricciardi, T. Riller, I. Ristorcelli, G. Rocha, C. Rosset, G. Roudier, M. Rowan-Robinson, J. A. Rubino-Martin, B. Rusholme, M. Sandri, D. Santos, M. Savelainen, G. Savini, D. Scott, M. D. Seiffert, E. P. S. Shellard, L. D. Spencer, J. Starck, V. Stolyarov, R. Stompor, R. Sudiwala, R. Sunyaev, F. Sureau, D. Sutton, A. Suur-Uski, J. Sygnet, J. A. Tauber, D. Tavagnacco, L. Terenzi, L. Toffolatti, M. Tomasi, M. Tristram, M. Tucci, J. Tuovinen, M. Turler, G. Umana, L. Valenziano, J. Valiviita, B. V. Tent, P. Vielva, F. Villa, N. Vittorio, L. A. Wade, B. D. Wandelt, I. K. Wehus, M. White, S. D. M. White, A. Wilkinson, D. Yvon, A. Zacchei, and A. Zonca, "Planck 2013 results. I. Overview of products and scientific results," *ArXiv e-prints*, Mar. 2013.

[52] M. J. Griffin, J. J. Bock, and W. K. Gear, "Relative performance of filled and feedhorn-coupled focal-plane architectures," *Applied Optics*, vol. 41, pp. 6543–6554, Nov. 2002.

[53] J. Zmuidzinas, "Thermal noise and correlations in photon detection," *Applied Optics*, vol. 42, pp. 4989–5008, Sept. 2003.

[54] K. Arnold, P. A. R. Ade, A. E. Anthony, D. Barron, D. Boettger, J. Borrill, S. Chapman, Y. Chinone, M. A. Dobbs, J. Errard, G. Fabbian, D. Flanigan, G. Fuller, A. Ghribi, W. Grainger, N. Halverson, M. Hasegawa, K. Hattori, M. Hazumi, W. L. Holzapfel, J. Howard, P. Hyland, A. Jaffe, B. Keating, Z. Kermish, T. Kisner, M. Le Jeune, A. T. Lee, E. Linder, M. Lungu, F. Matsuda, T. Matsumura, N. J. Miller, X. Meng, H. Morii, S. Moyerman, M. J. Myers, H. Nishino, H. Paar, E. Quealy, C. Reichardt, P. L. Richards, C. Ross, A. Shimizu, C. Shimmin, M. Shimon, M. Sholl, P. Siritanasak, H. Spieler, N. Stebor, B. Steinbach, R. Stompor, A. Suzuki, T. Tomaru, C. Tucker, and O. Zahn, "The bolometric focal plane array of the POLARBEAR CMB experiment," in *Society of Photo-Optical Instrumentation Engineers (SPIE) Confer-*

ence Series, vol. 8452 of *Society of Photo-Optical Instrumentation Engineers (SPIE) Conference Series*, Sept. 2012.

[55] G. Smecher, F. Aubin, E. Bissonnette, M. Dobbs, P. Hyland, and K. MacDermid, "Biasing and Demodulation Firmware for Kilopixel TES Bolometer Arrays," *ArXiv e-prints*, Aug. 2010.

[56] A. B. Goldin, M. S. Kowitt, E. S. Cheng, D. A. Cottingham, D. J. Fixsen, C. A. Inman, S. S. Meyer, J. L. Puchalla, J. E. Ruhl, and R. F. Silverberg, "Whole-Disk Observations of Jupiter, Saturn, and Mars in Millimeter/Submillimeter Bands," *Astrophysical Journal, Letters*, vol. 488, p. L161, Oct. 1997.

[57] J. Aumont, L. Conversi, C. Thum, H. Wiesemeyer, E. Falgarone, J. F. Macías-Pérez, F. Piacentini, E. Pointecouteau, N. Ponthieu, J. L. Puget, C. Rosset, J. A. Tauber, and M. Tristram, "Measurement of the Crab nebula polarization at 90 GHz as a calibrator for CMB experiments," *Astronomy and Astrophysics*, vol. 514, p. A70, May 2010.

[58] C. W. O'dell, B. G. Keating, A. de Oliveira-Costa, M. Tegmark, and P. T. Timbie, "CMB polarization at large angular scales: Data analysis of the POLAR experiment," *Physical Review D*, vol. 68, p. 042002, Aug. 2003.

[59] H. C. Chiang, P. A. R. Ade, D. Barkats, J. O. Battle, E. M. Bierman, J. J. Bock, C. D. Dowell, L. Duband, E. F. Hivon, W. L. Holzapfel, V. V. Hristov, W. C. Jones, B. G. Keating, J. M. Kovac, C. L. Kuo, A. E. Lange, E. M. Leitch, P. V. Mason, T. Matsumura, H. T. Nguyen, N. Ponthieu, C. Pryke, S. Richter, G. Rocha, C. Sheehy, Y. D. Takahashi, J. E. Tolan, and K. W. Yoon, "Measurement of Cosmic Microwave Background Polarization Power Spectra from Two Years of BICEP Data," *Astrophysical Journal*, vol. 711, pp. 1123–1140, Mar. 2010.

[60] D. Barkats, R. Aikin, C. Bischoff, I. Buder, J. P. Kaufman, B. G. Keating, J. M. Kovac, M. Su, P. A. R. Ade, J. O. Battle, E. M. Bierman, J. J. Bock, H. C. Chiang, C. D. Dowell, L. Duband, J. Filippini, E. F. Hivon, W. L. Holzapfel, V. V. Hristov, W. C. Jones, C. L. Kuo, E. M. Leitch, P. V. Mason, T. Matsumura, H. T. Nguyen, N. Ponthieu, C. Pryke, S. Richter, G. Rocha, C. Sheehy, S. S. Kernasovskiy, Y. D. Takahashi, J. E. Tolan, and K. W. Yoon, "Degree-scale Cosmic Microwave Background Polarization Measurements from Three Years of BICEP1 Data," *Astrophysical Journal*, vol. 783, p. 67, Mar. 2014.

[61] J. P. Kaufman, N. J. Miller, M. Shimon, D. Barkats, C. Bischoff, I. Buder, B. G. Keating, J. M. Kovac, P. A. R. Ade, R. Aikin, J. O. Battle, E. M. Bierman, J. J. Bock, H. C. Chiang, C. D. Dowell, L. Duband, J. Filippini, E. F. Hivon, W. L. Holzapfel, V. V. Hristov, W. C. Jones, S. S. Kernasovskiy, C. L.

Kuo, E. M. Leitch, P. V. Mason, T. Matsumura, H. T. Nguyen, N. Ponthieu, C. Pryke, S. Richter, G. Rocha, C. Sheehy, M. Su, Y. D. Takahashi, J. E. Tolan, and K. W. Yoon, "Self-Calibration of BICEP1 Three-Year Data and Constraints on Astrophysical Polarization Rotation," *ArXiv e-prints*, Dec. 2013.

[62] BICEP2 Collaboration, P. A. R. Ade, R. W. Aikin, M. Amiri, D. Barkats, S. J. Benton, C. A. Bischoff, J. J. Bock, J. A. Brevik, I. Buder, E. Bullock, G. Davis, C. D. Dowell, L. Duband, J. P. Filippini, S. Fliescher, S. R. Golwala, M. Halpern, M. Hasselfield, S. R. Hildebrandt, G. C. Hilton, V. V. Hristov, K. D. Irwin, K. S. Karkare, J. P. Kaufman, B. G. Keating, S. A. Kernasovskiy, J. M. Kovac, C. L. Kuo, E. M. Leitch, N. Llombart, M. Lueker, C. B. Netterfield, H. T. Nguyen, R. O'Brient, R. W. Ogburn, IV, A. Orlando, C. Pryke, C. D. Reintsema, S. Richter, R. Schwarz, C. D. Sheehy, Z. K. Staniszewski, K. T. Story, R. V. Sudiwala, G. P. Teply, J. E. Tolan, A. D. Turner, A. G. Vieregg, P. Wilson, C. L. Wong, and K. W. Yoon, "BICEP2 II: Experiment and Three-Year Data Set," *ArXiv e-prints*, Mar. 2014.

[63] C. O'Dell, D. Swetz, and P. Timbie, "Calibration of millimeter-wave polarimeters using a thin dielectric sheet," *Microwave Theory and Techniques, IEEE Transactions on*, vol. 50, pp. 2135–2141, Sep 2002.

[64] J. G. Magnum, "ALMA Memo 366: A Telescope Pointing Algorithm for ALMA," Apr. 2001.

[65] W. C. Jones, T. E. Montroy, B. P. Crill, C. R. Contaldi, T. S. Kisner, A. E. Lange, C. J. MacTavish, C. B. Netterfield, and J. E. Ruhl, "Instrumental and analytic methods for bolometric polarimetry," *Astronomy and Astrophysics*, vol. 470, pp. 771–785, Aug. 2007.

[66] J. P. Snyder, "Map projections—a working manual," *U.S. Geological Survey professional paper*, no. 1395, 1926.

[67] S. Das, T. A. Marriage, P. A. R. Ade, P. Aguirre, M. Amiri, J. W. Appel, L. F. Barrientos, E. S. Battistelli, J. R. Bond, B. Brown, B. Burger, J. Chervenak, M. J. Devlin, S. R. Dicker, W. Bertrand Doriese, J. Dunkley, R. Dünner, T. Essinger-Hileman, R. P. Fisher, J. W. Fowler, A. Hajian, M. Halpern, M. Hasselfield, C. Hernández-Monteagudo, G. C. Hilton, M. Hilton, A. D. Hincks, R. Hlozek, K. M. Huffenberger, D. H. Hughes, J. P. Hughes, L. Infante, K. D. Irwin, J. Baptiste Juin, M. Kaul, J. Klein, A. Kosowsky, J. M. Lau, M. Limon, Y.-T. Lin, R. H. Lupton, D. Marsden, K. Martocci, P. Mauskopf, F. Menanteau, K. Moodley, H. Moseley, C. B. Netterfield, M. D. Niemack, M. R. Nolta, L. A. Page, L. Parker, B. Partridge, B. Reid, N. Sehgal, B. D. Sherwin, J. Sievers, D. N. Spergel, S. T. Staggs, D. S. Swetz, E. R. Switzer, R. Thornton, H. Trac, C. Tucker, R. Warne, E. Wollack, and Y. Zhao, "The

Atacama Cosmology Telescope: A Measurement of the Cosmic Microwave Background Power Spectrum at 148 and 218 GHz from the 2008 Southern Survey," *Astrophysical Journal*, vol. 729, p. 62, Mar. 2011.

[68] E. Hivon, K. M. Górski, C. B. Netterfield, B. P. Crill, S. Prunet, and F. Hansen, "MASTER of the Cosmic Microwave Background Anisotropy Power Spectrum: A Fast Method for Statistical Analysis of Large and Complex Cosmic Microwave Background Data Sets," *Astrophysical Journal*, vol. 567, pp. 2–17, Mar. 2002.

[69] G. Hinshaw, D. N. Spergel, L. Verde, R. S. Hill, S. S. Meyer, C. Barnes, C. L. Bennett, M. Halpern, N. Jarosik, A. Kogut, E. Komatsu, M. Limon, L. Page, G. S. Tucker, J. L. Weiland, E. Wollack, and E. L. Wright, "First-Year Wilkinson Microwave Anisotropy Probe (WMAP) Observations: The Angular Power Spectrum," , vol. 148, pp. 135–159, Sept. 2003.

[70] QUIET Collaboration, C. Bischoff, A. Brizius, I. Buder, Y. Chinone, K. Cleary, R. N. Dumoulin, A. Kusaka, R. Monsalve, S. K. Næss, L. B. Newburgh, R. Reeves, K. M. Smith, I. K. Wehus, J. A. Zuntz, J. T. L. Zwart, L. Bronfman, R. Bustos, S. E. Church, C. Dickinson, H. K. Eriksen, P. G. Ferreira, T. Gaier, J. O. Gundersen, M. Hasegawa, M. Hazumi, K. M. Huffenberger, M. E. Jones, P. Kangaslahti, D. J. Kapner, C. R. Lawrence, M. Limon, J. May, J. J. McMahon, A. D. Miller, H. Nguyen, G. W. Nixon, T. J. Pearson, L. Piccirillo, S. J. E. Radford, A. C. S. Readhead, J. L. Richards, D. Samtleben, M. Seiffert, M. C. Shepherd, S. T. Staggs, O. Tajima, K. L. Thompson, K. Vanderlinde, R. Williamson, and B. Winstein, "First Season QUIET Observations: Measurements of Cosmic Microwave Background Polarization Power Spectra at 43 GHz in the Multipole Range $25 \leq \ell \leq 475$," *Astrophysical Journal*, vol. 741, p. 111, Nov. 2011.

[71] J. Grain, M. Tristram, and R. Stompor, "Polarized CMB power spectrum estimation using the pure pseudo-cross-spectrum approach," *Physical Review D*, vol. 79, p. 123515, June 2009.

[72] K. M. Smith, "Pseudo-C estimators which do not mix E and B modes," *Physical Review D*, vol. 74, p. 083002, Oct. 2006.

[73] T. Louis, S. Næss, S. Das, J. Dunkley, and B. Sherwin, "Lensing simulation and power spectrum estimation for high-resolution CMB polarization maps," *Monthly Notices of the RAS*, vol. 435, pp. 2040–2047, Nov. 2013.

[74] B. G. Keating, M. Shimon, and A. P. S. Yadav, "Self-calibration of Cosmic Microwave Background Polarization Experiments," *Astrophysical Journal, Letters*, vol. 762, p. L23, Jan. 2013.

[75] J. E. Lidsey, A. R. Liddle, E. W. Kolb, E. J. Copeland, T. Barreiro, and M. Abney, "Reconstructing the inflaton potential-an overview," *Reviews of Modern Physics*, vol. 69, pp. 373–410, Apr. 1997.

[76] L. Knox and Y.-S. Song, "Limit on the Detectability of the Energy Scale of Inflation," *Physical Review Letters*, vol. 89, p. 011303, July 2002.

[77] C. M. Hirata and U. Seljak, "Reconstruction of lensing from the cosmic microwave background polarization," *Physical Review D*, vol. 68, p. 083002, Oct. 2003.

[78] D. M. Goldberg and D. N. Spergel, "Microwave background bispectrum. II. A probe of the low redshift universe," *Physical Review D*, vol. 59, p. 103002, May 1999.